Electron Clouds in High Energy Hadron Accelerators

Elektronenwolken in Hochenergie-Hadronenbeschleunigern
Zur Erlangung des Grades eines Doktors der Naturwissenschaften (Dr. rer. nat.)
genehmigte Dissertation von M.Sc. Fedor Petrov aus Leningrad
August 2013 — Darmstadt — D 17

TECHNISCHE
UNIVERSITÄT
DARMSTADT

Fachbereich Elektrotechnik und
Informationstechnik

Institut für Theorie
Elektromagnetischer Felder

Electron Clouds in High Energy Hadron Accelerators
Elektronenwolken in Hochenergie-Hadronenbeschleunigern

Genehmigte Dissertation von M.Sc. Fedor Petrov aus Leningrad

1. Gutachten: Prof. Dr. rer. nat. Oliver Boine-Frankenheim
2. Gutachten: Prof. Dr. -Ing. Thomas Weiland
3. Gutachten: Prof. Dr. Dr. h.c./RUS Dieter H. H. Hoffmann

Tag der Einreichung: 05.02.2013
Tag der Prüfung: 13.05.2013

Darmstadt — D 17

Bitte zitieren Sie dieses Dokument als:
URN: urn:nbn:de:tuda-tuprints-
URL: http://tuprints.ulb.tu-darmstadt.de/

Erklärung zur Dissertation

Hiermit versichere ich, die vorliegende Dissertation ohne Hilfe Dritter nur mit den angegebenen Quellen und Hilfsmitteln angefertigt zu haben. Alle Stellen, die aus Quellen entnommen wurden, sind als solche kenntlich gemacht. Diese Arbeit hat in gleicher oder ähnlicher Form noch keiner Prüfungsbehörde vorgelegen.

Darmstadt, den August 29, 2013

(F. Petrov)

Kurzfassung

Die Bildung von Elektronenwolken ist in Positron- und Ionenbeschleunigern ein bekanntes Problem. Abhängig von den Strahlparametern können sich Elektronenwolken verschiedenartig äußern. Ziel der vorliegenden Arbeit ist die Untersuchung der Elektronenwolken im Large Hadron Collider (LHC) und im Super Proton Synchrotron (SPS) bei Genf (Schweiz) sowie im Schwerionensynchrotron SIS-100 als Teil des FAIR-Projekts (Facility for Antiproton and Ion Research) bei Darmstadt (Deutschland).

Am SIS-100 soll langsame Extraktion durchgeführt werden: Nachdem der Strahl die Extraktionsenergie erreicht hat, wird er in einen Gleichstromstrahl umgeformt und innerhalb etwa einer Sekunde zu den Experimenten extrahiert. Werden genügend Elektronen akkumuliert, wird der Strahl instabil. Im Vergleich zum SIS-100 sind die Teilchen im Strahl unter SPS- und LHC-Bedingungen immer in Teilchenpaketen gebündelt. In einem solchen Strahl werden die Elektronen durch Sekundäremission erzeugt. Während der Anfertigung dieser Arbeit stellte sich heraus, dass die Strahlintensität im LHC und im SPS durch Elektronenwolken begrenzt wird. Unter anderem wird die Strahlqualität beim Betrieb mit 25ns Abstand zwischen den Paketen durch Elektronenwolken hoher Dichte stark beeinträchtigt. Darüber hinaus äußern sich beim Betrieb mit größerem Abstand schon Elektronenwolken geringer Dichte in einem messbaren Verlust der Strahlenergie.

Im Rahmen dieser Doktorarbeit wurde festgestellt, dass die Stabilitätsgrenze von gleichförmigen Ionenstrahlen mit gleichen Emittanzen, Energien und raumladungserzeugten Betatronfrequenzverschiebungen identisch ist. Dabei wurden erstmals Simulationen durchgeführt, in denen die Auswirkung von Coulombstößen auf die Elektronendichte berücksichtigt wurde. Es konnte gezeigt werden, dass für jeden Gleichstromstrahl eine Restgasdichte gefunden werden kann, ab der die Elektronenwolken kein Intensitätslimit mehr darstellen. Wir nennen solche Bedingungen ein "gutes" Vakuum. Im SIS-100 ermöglicht der geplante Restgasdruck von 10^{-12} mbar diesen Betrieb.

Für SPS- und LHC-Bedingungen wurden Simulationen der Elektronenwolkenwakefelder durchgeführt, unter anderem erstmals 3D-Simulationen. Die Resultate der mit Hilfe der Software VORPAL durchgeführten 3D-Simulationen wurden mit den Ergebnissen von elektrostatischen 2D-Codes verglichen. In Letzteren wird nur die Wechselwirkung zwischen Elektronenwolke und Strahl transversal zur Strahlrichtung berücksichtigt. Bei diesem Vergleich wurde festgestellt, dass die 2D-Approximation die Ergebnisse der 3D-Simulationen in guter Näherung reproduziert. Darüber hinaus wurde ein analytischer Ausdruck für das longitudinale Elektronenwolkenwakefeld abgeleitet. Für niedrige Strahlintensitäten wurden mit dem

analytischen Ausdruck Ergebnisse erzielt, die sehr gut mit denen der Simulationen übereinstimmen.

Abstract

The formation of electron clouds in accelerators operating with positrons and positively charge ions is a well-known problem. Depending on the parameters of the beam the electron cloud manifests itself differently. In this thesis the electron cloud phenomenon is studied for the CERN Super Proton Synchrotron (SPS) and Large Hadron Collider (LHC) conditions, and for the heavy-ion synchrotron SIS-100 as a part of the FAIR complex in Darmstadt, Germany.

Under the FAIR conditions the extensive use of slow extraction will be made. After the acceleration the beam will be debunched and continuously extracted to the experimental area. During this process, residual gas electrons can accumulate in the electric field of the beam. If this accumulation is not prevented, then at some point the beam can become unstable. Under the SPS and LHC conditions the beam is always bunched. The accumulation of electron cloud happens due to secondary electron emission. At the time when this thesis was being written the electron cloud was known to limit the maximum intensity of the two machines. During the operation with 25 ns bunch spacing, the electron cloud was causing significant beam quality deterioration. At moderate intensities below the instability threshold the electron cloud was responsible for the bunch energy loss.

In the framework of this thesis it was found that the instability thresholds of the coasting beams with similar space charge tune shifts, emittances and energies are identical. First of their kind simulations of the effect of Coulomb collisions on electron cloud density in coasting beams were performed. It was found that for any hadron coasting beam one can choose vacuum conditions that will limit the accumulation of the electron cloud below the instability threshold. We call such conditions the "good" vacuum regime. In application to SIS-100 the design pressure 10^{-12} mbar corresponds to the good vacuum regime. The transition to the bad vacuum regime can happen for pressures larger than 10^{-11} mbar.

For the SPS and LHC conditions the simulations of the electron cloud wake fields were performed. The wake fields calculated using VORPAL were compared with the results of the 2D electrostatic code for the first time. In the latter the beam-cloud interaction is purely transverse. It was found that the results of the simplified code agree very well with the results of 3D electromagnetic simulations in VORPAL. Moreover, based on the kick approximation an analytical expression for the longitudinal electron cloud wake field was derived. The analytical expression gives a good agreement with the simulation result for very low bunch intensities.

Contents

1 Introduction

Since the time of the first accelerators a huge technological step forward in the accelerator technology has been made. Nowadays particle accelerators are applied in many fields of human activity. More and more accelerators are being built for the medical applications [1, 2]. Accelerator driven systems also promise to solve the problems of the nuclear waste handling [3]. Besides, there are numerous applications of the synchrotron light sources [4]. But the most advanced and high energy accelerators are used in the field of scientific research. In particular they are applied to study the interaction of elementary particles, and heavy ion accelerators are used to synthesize new rare isotopes and quark-gluon plasma. The construction and operation of such new accelerators is facing numerous technological challenges.

The stability of particle beams is of great importance in all the particle accelerators of the world. Beam particles interact with each other, with accelerator structures, and with other surrounding species. Residual gas particles, ions, and electrons are among them. For the operation with positively charge beams predominantly the latter two kinds of species pose a threat. Interaction of ion beams with residual gas species can cause the change of the beam species charge state [5]. As a consequence such particles significantly deviate from the design orbit and get lost. Another important effect is the residual gas ionization by the beam particles. In this case the electrons and positively charged ions are produced. Electrons can also originate from secondary emission, beam losses and photo effect [6, 7]. Depending on the beam parameters electrons can accumulate and cause beam instabilities, emittance growth, and heat load on the wall. The so-called *electron cloud effects* were known since 1960-s, when the first observations and studies were performed in the Soviet Union [8], the United States [9] and a little later in Europe [10]. Much effort is made to take into account and prevent the electron cloud effects in future facilities, such as the International Linear Collider [11]. In this thesis the interaction between the positively charged beams and electrons is studied under the conditions of two accelerator facilities. The electron cloud effects in coasting beams are studied in application to the Facility for Antiproton and Ion Research (FAIR). Meanwhile, the electron cloud wake fields are studied in application to the Large Hadron Collider (LHC) and the Super Proton Synchrotron (SPS) in CERN.

FAIR is a new international accelerator facility that will provide antiproton and heavy-ion beams with unprecedented intensity and quality [12]. These beams will be used in many experimental programs. To achieve the goal intensity ions with intermediate charge states will be used. For such ions (e.g. U^{28+}) the process of charge exchange in collisions with residual gas molecules is very effective [5, 13]. The loss of the beam ions due to this process can be avoided by the proper high vacuum conditions. To mitigate the charge exchange problem the

SIS-100 is specially designed to control the dynamic vacuum [13, 14]. In [15] it was shown that secondary electron emission under FAIR conditions is not important. However, before this thesis it was not completely clear, whether the design vacuum will be good enough to avoid the dangerous build-up of the electron cloud during the slow extraction. In coasting beams and low intensity long bunches the residual gas electrons can accumulate being trapped in the beam potential [10]. This can lead to the two-stream instability. The first observations of this phenomenon were made in 1960-s in the Novosibirsk Proton Storage Ring [16]. The instabilities of the two-stream type were also observed later in the ISR (Intersecting Storage Rings) [17, 10], etc.

In the CERN LHC and SPS the conditions are significantly different from FAIR. The charge exchange does not play any role in the high energy proton beams. Compared to the 50 ns bunch length in the FAIR SIS-100, bunches in the LHC are only around 1.0 ns long. In short bunches the electron clouds are accumulating mainly due to the secondary electron emission. Most of the time electrons do not see the beam field. As soon as the bunch arrives, electrons get attracted towards the bunch center. This causes the formation of the electron cloud pinch with a very high density near the beam axis. The coupled motion of the cloud and the bunch in this case leads to the head-tail instability and/or emittance growth [18]. The electron cloud affects not only the bunch but also the beam surroundings. As soon as the bunch flies away, the electrons are released. They deposit their kinetic energy to the wall. The consequences are the dynamic pressure rise and the heat load. The latter poses a potential threat to the cryogenic systems of superconducting accelerators. All these effects were observed in the LHC and the SPS. In this thesis the longitudinal and transverse electron cloud wake fields are studied for short proton bunches.

This document has the following structure. In Chapter 2 the FAIR and CERN complexes are introduced in greater details. The experimental programs of the both facilities are highlighted as well as the parameters of the main synchrotrons. Chapter 3 gives an overview of the beam and accelerator characteristics in the zero intensity (noninteracting beam particles) approximation. Chapter 4 is devoted to the collective effects in particle accelerators when the beam current is not negligible. In Chapter 5 the origin of the electron cloud in accelerator and its effect on the beam are described. Chapter 6 describes the features of the numerical codes used in the simulations. In Chapter 7 the results of the simulations are presented and discussed. Finally, Chapter 8 summarizes and concludes the studies performed in this thesis.

2 FAIR and CERN

2.1 Facility for Antiproton and Ion Research

The Facility for Antiproton and Ion Research (FAIR) is going to provide the beams with the unprecedented intensity and luminosity [12]. Operation with protons and antiprotons is a new feature of the project compared to the existing GSI Helmholtz Center for Heavy Ion Research. To achieve the goal intensities the ions with the intermediate charge states will be used. This allows to increase the total number of beam particles, however, at the expense of beam energy.

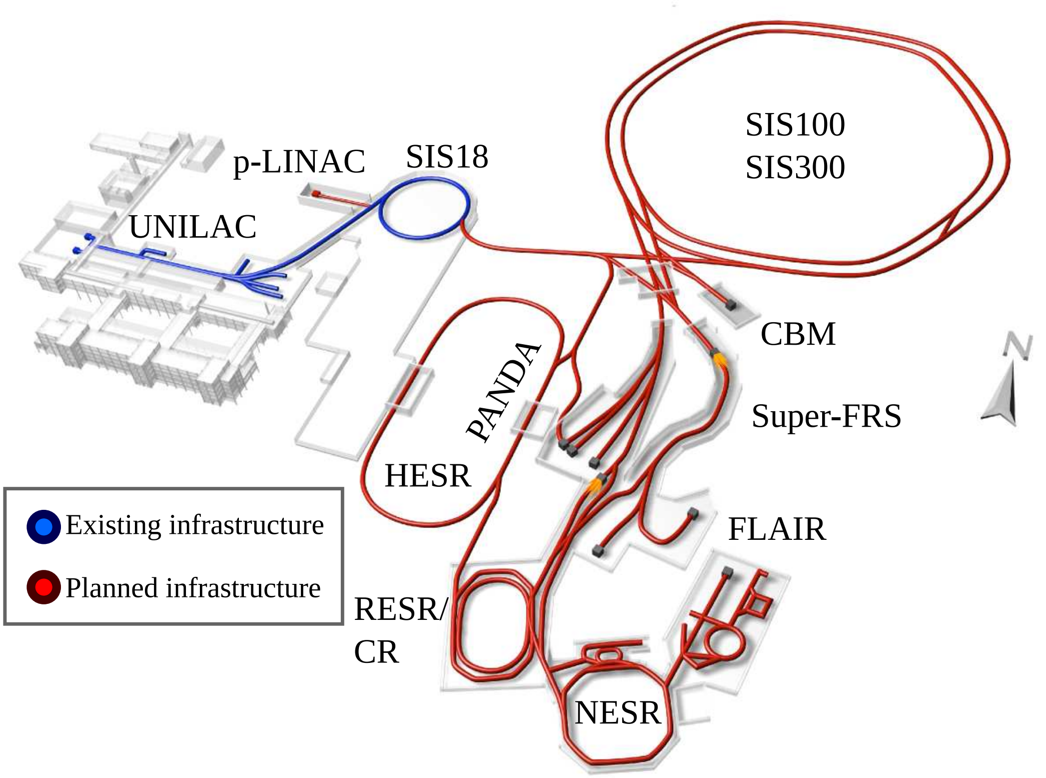

Figure 2.1.: (Courtesy www.fair-center.eu) Future infrastructure of FAIR. Existing structures are shown in blue. Future structures are shown in red. The existing accelerators UNILAC and SIS-18 will serve as injector for the new SIS-100.

The planned and existing infrastructure of FAIR is shown in Fig. 2.1. The existing UNILAC (Universal Linear Accelerator) and SIS-18 (Schwerionensynchrotron-18) are going to deliver the particle beams to the new SIS-100 synchrotron. It will in turn provide the beam to other rings and experimental areas. To enable the operation with the proton beams a new p-linac will

Table 2.1.: SIS-100 parameters [12, 28]

Parameter	Value
Circumference / m	1083
Magnetic rigidity / Tm	100
Bending radius / m	52.63
Number of dipole magnets	108
Number of quadrupole magnets	168
Repetition rate / Hz	1

be built. Antiprotons will be generated in the collisions of the proton beams with the antiproton target at 29 GeV/u [19]. These antiprotons will be finally collected and stochastically cooled in the HESR (**H**igh **E**nergy **S**torage **R**ing) [20]. Afterwards, they will collide with the fixed target inside PANDA (Anti-**P**roton **An**nihilation at **Da**rmstadt) detector [21]. In these collisions the physics of strong interactions will be investigated. This experiment is one of the key experiments at FAIR. FLAIR (**F**acility for **L**ow-energy **A**ntiproton and **I**on **R**esearch) will be used for the experiments with low energy antiprotons [22]. Under the FLAIR conditions, several interesting topics such as gravitation of antimatter, spectral properties of antiprotonic atoms, antiproton medical applications can be studied [23]. The nuclei-nuclei collisions will be investigated using the CBM (**C**ompressed **B**aryonic **M**atter) detector [24]. The aim of these experiments is the investigation of highly compressed nuclear matter. Super-FRS (Super **Fr**agment **S**eparator) will be utilized to study the short-lived nuclei [25].

The key synchrotron in FAIR enabling the experimental program will be the superconducting SIS-100 (Schwerionensynchrotron-100). Some of the SIS-100 parameters are listed in Table 2.1. Because the intermediately charged ions are chosen for the operation, the design vacuum is 10^{-12} mbar and a special collimation system is developed [13, 14]. The final intensity of the SIS-100 is formed by the four consecutive injections from the SIS-18. A significant progress in intensity parameters has been made in the past years. Since 2006 until now the intensity of U^{28+} has been increased approximately by factor 7 [26, 27]. The upper limit for the number of extracted ions under the present SIS-18 conditions is $5 \cdot 10^{10}$, which is still lower than the FAIR design parameters given in Table 2.2.

The beams can be extracted from the SIS-100 differently [29]. One way is the fast extraction in one revolution period. In this case the extraction kicker is implemented. The beam extracted this way is bunched. Another method is the slow extraction that can take up to several seconds.

Table 2.2.: Parameters of the SIS-100 beams [12, 28]

Specie	Min. energy / MeV/u	Max. energy / GeV/u	Intensity
U^{28+}	200	2.7	$5 \cdot 10^{11}$
proton	4000	29	$4 \cdot 10^{13}$

In this case the coasting beam is slowly driven to the third order resonance by sextupoles. In this document the electron cloud effects are studied in application to the coasting beam during the slow extraction.

2.2 CERN

The European Organization for Nuclear Research (CERN) is the world's largest accelerator complex. The organization was launched in 1954. Since then it has been gradually growing up to the present day. During the past decades several physics discoveries have been made in experiments performed on the CERN site. Two Nobel Prizes in Physics were awarded to the CERN scientists. One was received for the discovery of the W and Z bosons [30]. Another one was awarded for the invention and development of particle detectors [31]. Big contribution was made to the field of accelerator physics. Presently the CERN activity is mainly concentrated on the LHC operation.

The existing complex consists of the cascade of synchrotrons, each accelerating the proton beams to higher energies. The two largest rings are the LHC and the Super Proton Synchrotron (SPS), which works as injector into the LHC. Presently the SPS extraction energy is 450 GeV/u. The top design beam energy of the LHC is 7 TeV/u [32]. Both of the rings are used to accelerate protons and lead ions. At the time when this thesis was being written, the design parameters were not reached because of the electron cloud instabilities.

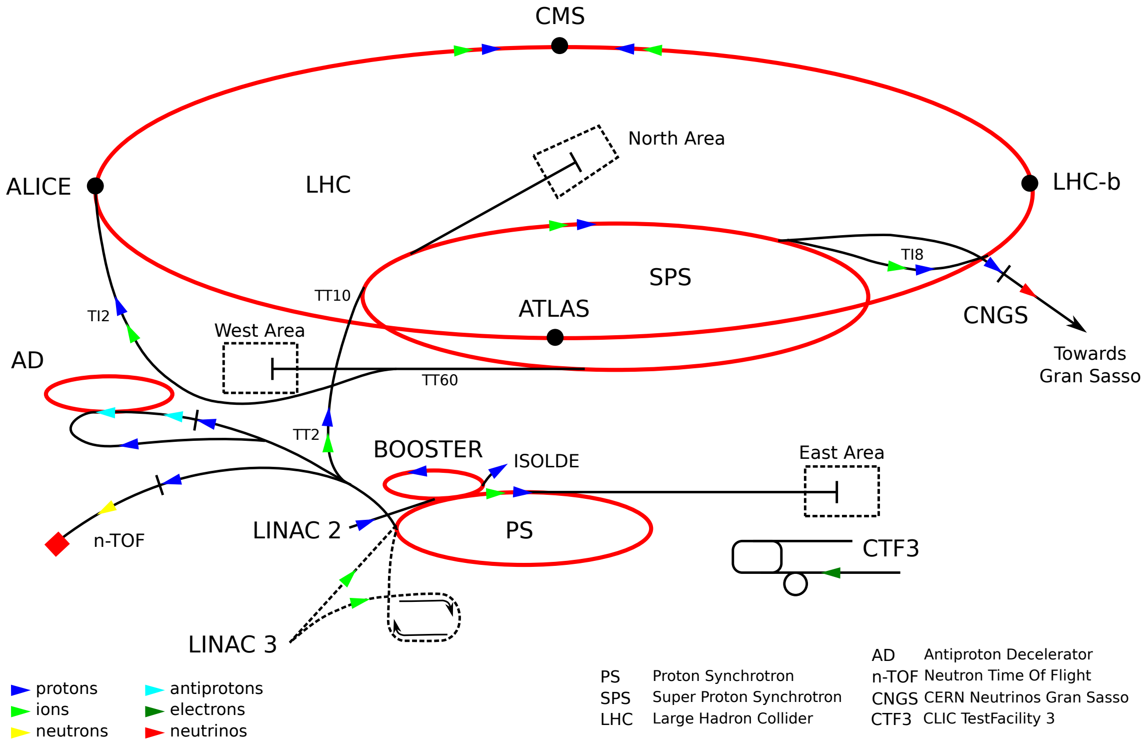

Figure 2.2.: (Courtesy Forthommel) The CERN accelerator complex. The LHC and the SPS are the largest rings. The main detectors such as ALICE, the CMS, the LHCb and ATLAS are positioned along the LHC.

There are seven detector experiments planned for the LHC. ATLAS (A Toroidal LHC Apparatus) and the CMS (Compact Muon Solenoid) are general physics detectors [33, 34]. They serve for similar goals. However, the technical principles of these detectors are different. Having two independent detectors allows to crosscheck the experimental results. The ALICE (A Large Ion Collider Experiment) detector is used to study the quark-gluon plasma in experiments with colliding lead ions [35]. The LHCb (Large Hadron Collider beauty) experiment is studying the reasons for the matter prevailing over the antimatter [36]. TOTEM (TOTal Elastic and diffractive cross section Measurement) and the LHCf (Large Hadron Collider forward) experiments are focused on the forward particles [37, 38]. The deployment of the MoEDAL (Monopole and Exotics Detector At the LHC) experiment started in 2011 [39]. One of its goals is to search for the magnetic monopoles.

Table 2.3.: Parameters of the LHC and the SPS operating with protons.

Parameter	in LHC	in SPS
Circumference / km	26.659	6.9
Maximum energy / TeV	7	0.450
Bunch spacing / ns	25	25
Bunch length, $4\sigma_z$ / cm	7.55	11.24
Bunch intensity	$1.15 \cdot 10^{11}$	$1.15 \cdot 10^{11}$
Luminosity / $\mathrm{cm}^{-2}\mathrm{s}^{-1}$	10^{-34}	—

Bunch properties in the LHC are significantly different from what is planned for FAIR. The design LHC and SPS parameters are listed in Table 2.3. In the early phase the LHC has been working with lower bunch energies up to 3.5 TeV/u. Even under these conditions in both machines the electron cloud builds up leading to the losses of the beam. That is why until now all the experiments have been performed with 50 ns bunch spacings. Even in stable bunches the electron cloud manifests itself via synchronous phase shift [40]. The synchronous phase shift is connected with the electron cloud wake field. The studies of these fields are presented in this thesis.

3 The Dynamics of Low Intensity Beams

The dynamics of low intensity beams is an important starting point in understanding of the complex phenomena observed in accelerators. Low intensity implies that the electromagnetic forces acting between the particles are negligible compared to the bending and focusing forces of the accelerator structures. A detailed description of beam dynamics and accelerator physics can be found in a variety of books [41, 42, 43, 44, 45]. The basics of the charged particles transverse and longitudinal dynamics in circular accelerators is presented in this chapter. The accelerator model in this chapter is kept as simple as possible. Section 3.1 starts with the description of a single particle transverse dynamics. Basic parameters of the beam as an ensemble of noninteracting particles are explicated. In Section 3.2 the longitudinal dynamics of noninteracting particles in presence of accelerating Radio-Frequency (RF) fields is examined. Section 3.3 is dedicated to the parameters of the beam as an ensemble of noninteracting particles.

3.1 Transverse Beam Dynamics

3.1.1 Single Particle Dynamics

In this subsection the motion of a single particle in a circular accelerator is studied. Charged particles of the beam move under the influence of the Lorentz force:

$$\vec{F} = eZ(\vec{E} + \vec{v} \times \vec{B}). \tag{3.1}$$

where $\vec{B}$ is the magnetic field, $\vec{E}$ is the electric field, e is the elementary charge, Z is the particle charge state and $\vec{v}$ is the particle velocity. Momentum of the relativistic particle is

$$\vec{p} = \gamma A m_0 \vec{v}, \tag{3.2}$$

where A is the mass number, m_0 is the atomic mass unit, $\gamma = 1/\sqrt{1-(\frac{v}{c})^2}$, c is the speed of light.

In absence of accelerating fields and collective effects the particle is guided through accelerator structures by magnetic fields. These fields come from dipoles, quadruples and higher order magnetic multipoles. Bending dipole magnets serve to hold the particle on a circular orbit. Quadrupoles work as focusing lenses in one plane and defocusing ones in another. The section composed of alternating focusing and defocusing magnets is called the FODO cell. If the magnets are arranged in a certain way, the FODO cell gives a net focusing in both planes. The whole magnetic structure of the accelerator is called *lattice*.

Appropriately constructed accelerator optics sets the *reference orbit*. It is defined as the trajectory of an *ideal particle* with nominal momentum $\vec{p_0}$. The revolution frequency of the particle is $f_0 = L/\beta c$. Non-ideal particles oscillate in the vicinity of the reference orbit. Their motion is described by a six-dimensional vector in Cartesian coordinates. The coordinate system moves along the reference orbit with the nominal momentum $\vec{p_0}$. The vector of coordinates is given as follows:

$$\vec{r} = \begin{pmatrix} x \\ x' \\ y \\ y' \\ s \\ \delta_p \end{pmatrix}, \tag{3.3}$$

where x, y, s are the coordinates of the real particle, x' and y' stand for the horizontal and vertical momenta (the derivative of x and y along z), $\delta_p = \Delta p/p_0 = (p - p_0)/p_0$ is the deviation of the longitudinal particle momentum from the ideal one. Vector $\vec{r}$ is schematically shown in Fig. 3.1. $\vec{z}$ axis directs parallel to the reference orbit and the coordinate along this axis can be connected with the time advance via $s = \beta ct$. The vector (Eq. 3.3) gives the deviation of the real particle trajectory from the ideal one. Coordinates x and y form a transverse plane. Particles with $\delta_p \neq 0$ are called *off-momentum particles*.

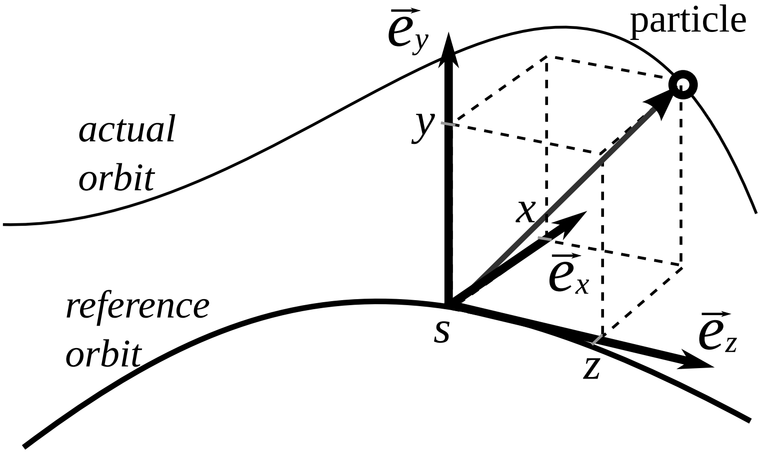

Figure 3.1.: Rectangular coordinate system with the center in the reference particle. The real particle trajectory deviates from the reference orbit.

Assuming only linear focusing and absence of coupling between planes one can write the equation of particle transverse motion

$$x'' + k(s)_x x = 0. \tag{3.4}$$

Here $k(s)$ is the linear focusing force due to the quadrupole field depending on the longitudinal position. The derivatives are taken along the longitudinal coordinate $s = \beta ct$. In circular accelerator the focusing force seen by a particle is periodic, i.e., $k(s) = k(s + L)$. Equation 3.4 with periodic focusing is called Hill's equation [46]. It can be solved yielding

$$x(s) = \sqrt{\epsilon_x \beta_x(s)} \cos(\psi_x(s) + \theta_0), \tag{3.5}$$

where β_x is the *betatron function* describing the envelope of particle trajectories, ϵ_x is the integration constant obtained from initial conditions, θ_0 is the initial phase. Phase advance is connected with betatron function by virtue of

$$\psi_x(s) = \int_0^s \frac{ds}{\beta_x(s)}. \tag{3.6}$$

An important characteristic of circular accelerators is the *betatron tune* Q_x:

$$Q_x = \frac{1}{2\pi} \oint \frac{ds}{\beta_x(s)}. \tag{3.7}$$

It stands for the number of oscillations preformed by the particle along the reference orbit in one turn. The frequency associated with the tune

$$f_\beta = Q_x f_0 \tag{3.8}$$

is called the *betatron frequency*. In the *smooth focusing approximation* the single particle motion in the unperturbed case is described as a simple harmonic oscillator:

$$u'' + (\frac{Q_x}{R})^2 u = 0. \tag{3.9}$$

As it was mentioned above dipole magnets confine the trajectory of particles to a circular orbit. The orbit of a particle in a synchrotron is characterized by the mean bending radius $R = L/2\pi$, where L represents the length of the synchrotron circumference. The product of the maximum dipole magnetic field B and R is called the *magnetic rigidity*. It is connected with charge Ze and p_0 of an ideal particle by virtue of

$$B\rho = \frac{p_0}{Ze}. \tag{3.10}$$

We have replaced R with ρ to conform the tradition. Using this quantity one can calculate the maximum energy of the particle with the given charge and mass.

Several features arise when the momentum deviation of the particle is not zero [47]. The focusing strength of the quadrupole is given as

$$k(s) = \frac{1}{B\rho} \frac{dB_z}{dx} \approx \frac{1}{B\rho_0} \frac{dB_z}{dx} (1 - \delta_p), \tag{3.11}$$

where B_z is the longitudinal component of the magnetic field, zero index indicates the rigidity of the ideal particle. Since the value of Q_x depends on $k(z)$, one can arrive at the following expression:

$$\frac{\Delta Q_x}{Q_x} = \xi \delta_p, \tag{3.12}$$

where ξ is called the *normalized chromaticity*. When lattice consists only of focusing quadrupoles, it is called the *natural chromaticity*. In large rings natural chromaticity and corresponding tune spread are very large and need to be compensated. For this purpose higher order multipoles are used. However, the chromaticity is usually chosen to be at least a little bit higher than zero to maintain the beam stability. The reason for this will be explained in Section 4.2. Off-momentum particles also have a slightly different trajectory with a modified radius. This modification is described by the dispersion function $D(s)$. It connects the horizontal shift $\Delta x(s)$ of the off-momentum particle with δ_p:

$$D(s) = \frac{\Delta x(s)}{\delta_p}. \tag{3.13}$$

A particle having $\delta_p \neq 0$ has also a slightly modified revolution frequency. As far as $\beta \ll 1$ an increase of δ_p leads to an increase of ω_0, i.e., $\delta\omega_0/\delta_p > 0$. The mass of particles starts to grow when β approaches 1. For high γ this leads to the negative $\delta\omega_0/\delta_p < 0$. The energy at which $\delta\omega_0/\delta_p = 0$ is called the *transition energy*. The corresponding Lorentz factor is γ_t. When δ_p is small, the change of revolution frequency is the linear function of momentum deviation:

$$\frac{\Delta\omega_0}{\omega_0} = -\eta\delta_p, \tag{3.14}$$

where the slip factor is given by

$$\eta = \frac{1}{\gamma_t^2} - \frac{1}{\gamma^2}. \tag{3.15}$$

The dispersion is neglected throughout this work.

The particle easily becomes unstable if the horizontal and vertical tunes are chosen according to

$$k \cdot Q_x + l \cdot Q_y = n. \tag{3.16}$$

Here k, l and n are integer numbers. Eq. 3.16 represents a set of resonant conditions [42]. If the equation is satisfied, then the effect of focusing errors present in real accelerators is resonantly multiplied.

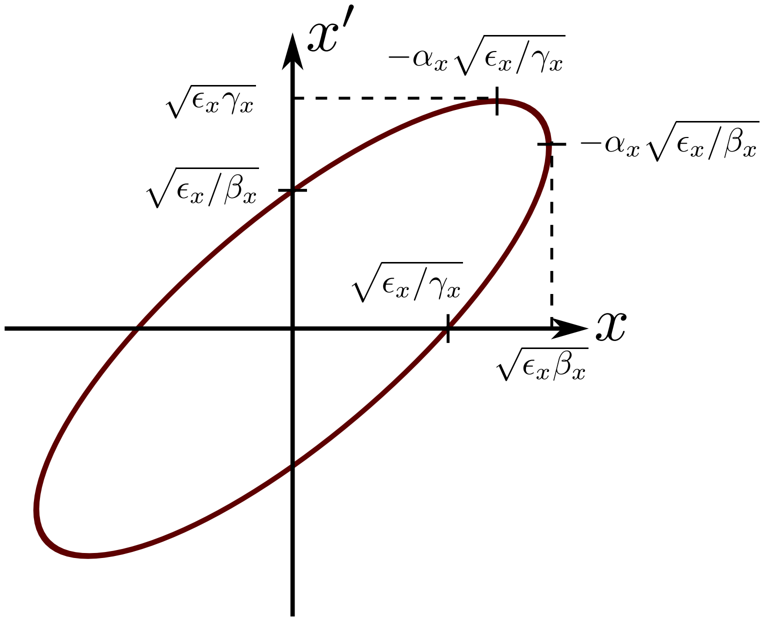

Figure 3.2.: Particle horizontal phase space ellipse. Particle coordinates observed at a fixed point in an accelerator cover this ellipse uniformly. The maximum amplitude and momentum are expressed through the accelerator Twiss parameters.

3.1.2 Transfer Matrix Approach

One important feature of the particle motion in circular accelerator is that it can be described in terms of transfer matrices. This fact is widely used in simulation codes where interaction with surroundings is reduced to several points. In between these points the beam is transfered using the matrices. To proceed we need to introduce additional parameters:

$$\alpha(s) \equiv -\frac{\beta'(s)}{2} \tag{3.17}$$

and

$$\gamma(s) \equiv \frac{1+\alpha^2(s)}{\beta(s)}. \tag{3.18}$$

The functions $\beta(s)$, $\alpha(s)$ and $\gamma(s)$ are the so-called *Twiss parameters*. Let us rewrite the particle transverse coordinate and momentum in terms of these functions:

$$\begin{cases} x(s) = \sqrt{\epsilon_x\beta(s)}\cos(\psi_x(s)+\theta_0) \\ x'(s) = \sqrt{\dfrac{\epsilon_x}{\beta_s}}\left[-\sin(\psi_x(s)+\theta_0)+\alpha(s)\cos(\psi_x(s)+\theta_0)\right] \end{cases}. \tag{3.19}$$

The evolution of the particle transverse phase space while traveling between s to s_0 can be expressed by the following matrix:

$$M_{tr}(s,s_0) = \begin{bmatrix} \sqrt{\frac{\beta_x}{\beta_{x,0}}}(\cos\Delta\psi + \alpha_{x,0}\sin\Delta\psi) & \sqrt{\beta_x\beta_{x,0}}\sin\Delta\psi \\ \sqrt{\frac{1}{\beta_x\beta_{x,0}}}\left[(\alpha_{x,0}-\alpha_x)\cos\Delta\psi-(1+\alpha_{x,0}\alpha_x)\sin\Delta\psi\right] & \sqrt{\frac{\beta_{x,0}}{\beta_x}}(\cos\Delta\psi-\alpha_x\sin\Delta\psi) \end{bmatrix}, \tag{3.20}$$

where $\Delta\psi = \psi(s) - \psi(s_0)$ is the phase advance. In the constant focusing approximation this matrix is simplified:

$$M_{tr}(s,s_0) = \begin{bmatrix} \cos(\frac{2\pi Q_x}{L}(s-s_0)) & \overline{\beta}_x\sin(\frac{2\pi Q_x}{L}(s-s_0)) \\ -\overline{\beta}_x^{-1}\sin(\frac{2\pi Q_x}{L}(s-s_0)) & \cos(\frac{2\pi Q_x}{L}(s-s_0)) \end{bmatrix}, \tag{3.21}$$

where $\overline{\beta}_x$ is the average beta function. Particles which motion is described by the transfer matrices mentioned above form an ellipse in the transverse phase space (Fig. 3.2). The area of this ellipse is connected with the integration constant ϵ_x.

3.2 Longitudinal Dynamics

RF cavities are used in accelerators to form bunches and accelerate the beams. The most simple case is when cavity is driven by a sinusoidal wave. In this case its accelerating voltage is given as follows:

$$V_{rf}(t) = V_0 \cdot sin(\omega_{rf}t) = V_0 \cdot sin(\phi_s(t)). \tag{3.22}$$

The RF frequency satisfies $\omega_{rf} = h\omega_0$, where h is the integer harmonic number. A particle having the nominal energy and trajectory always experiences one and the same ϕ_s, which is called the *synchronous phase*. The exactly synchronized particle is called the *synchronous particle*. Particles deviating from the nominal parameters experience different accelerating voltage relative to the synchronous particle 3.3. Below the transition energy a particle that is slower arrives at the cavity later than the synchronous one. Thus, the particle receives a higher voltage kick relative to the ideal case. A particle having bigger energy than the synchronous one gets smaller kick. Above the transition energy slower particles have bigger revolution frequency and vice versa. In this case ϕ_s should be chosen to give bigger kicks to more energetic particles and smaller kicks to less energetic ones. This leads to the oscillations of nonideal particles around the synchronous phase. These oscillations are called thr *synchrotron oscillations* and described by the following system of equations:

$$\begin{cases} \dfrac{d\phi}{dt} = -\dfrac{\eta\omega_{rf}}{Lp_0}W \\ \dfrac{dW}{dt} = ZeV_0(sin(\phi) - sin(\phi_s)) \end{cases}, \tag{3.23}$$

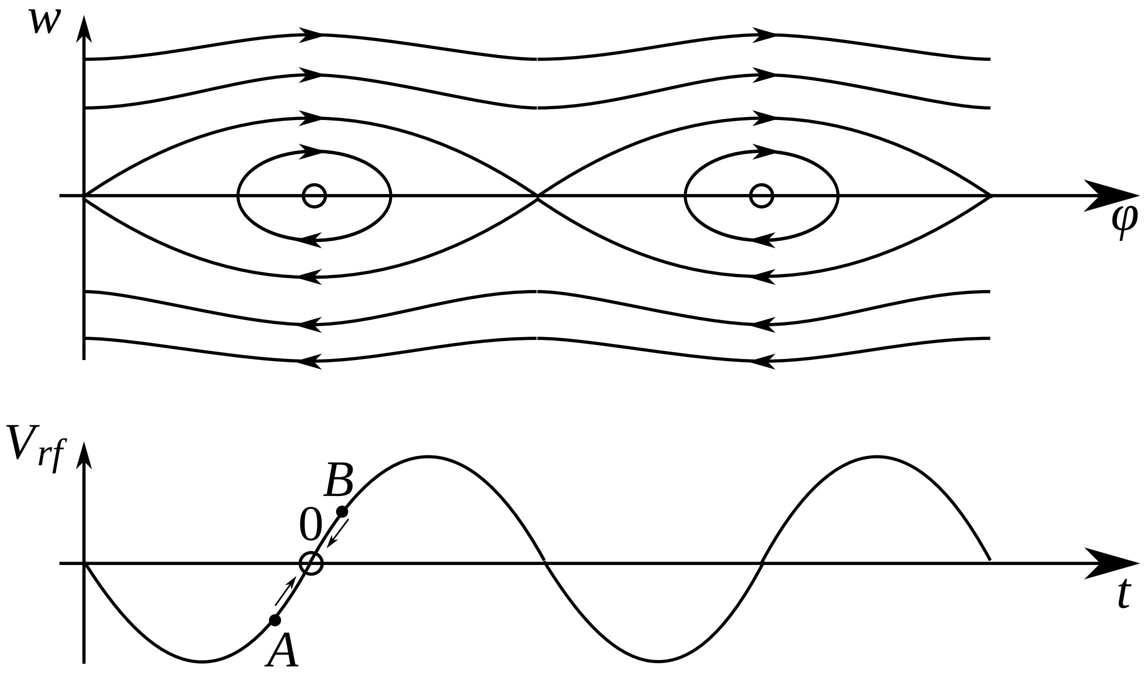

Figure 3.3.: Longitudinal phase space in which the particle moves (top) and RF voltage (bottom). Below the transition particle that arrives later (B) than synchronous particle gets positive kick, faster particle (A) that arrives earlier gets decelerating kick.

where $W = L\Delta p$. This system of equations can be transformed to a second order differential equation

$$\ddot{\phi} + \frac{\Omega_s^2}{cos(\phi_s)}(sin(\phi) - sin(\phi_s)) = 0, \tag{3.24}$$

where

$$\Omega_s = \sqrt{\frac{ZeV_0\omega_{rf}|\eta|cos(\phi_s)}{Cp_0}} \tag{3.25}$$

is the synchrotron angular frequency in $\phi - \phi_s \ll 1$ approximation. Similar to the transverse dynamics one defines the *synchrotron tune*

$$Q_s = \frac{\Omega_s}{\omega_0} = \sqrt{\frac{ZeV_0h|\eta|cos(\phi_s)}{2\pi\gamma Am_0c^2}} \tag{3.26}$$

Typically this value is very small. One full synchrotron oscillation happens in several hundreds or thousands revolution periods.

3.3 Particle Ensemble Dynamics

An ensemble of particles (beam) manifests the parameters not present in case of a single particle. The most important parameters are the beam size, beam offset and beam emittance. The latter one is the invariant of the beam. These parameters are introduced in subsection 3.3.1. Subsection 3.3.2 explicates the features of the beam arising from the finite number of beam particles. The discrete nature of the beam manifests itself in the Schottky noise [48, 49]. Spectral characteristics of this noise reveal the beam and accelerator parameters. Studying this noise in the real machine one can find the beam momentum spread, chromaticity and betatron tune. The finite width of the betatron side bands plays an important role in beam stabilization.

3.3.1 Transverse Beam Parameters

Any particle beam is an ensemble of many particles randomly distributed in phase space. This distribution can be very sophisticated depending on the accelerator conditions [50, 51]. However, the most widely used beam parameters are the first momenta of its distribution function. Let $F(x,x',z)$ be the distribution function of the beam transverse coordinates and momenta. It is normalized so that

$$\int_{-\infty}^{\infty}\int_{-\infty}^{\infty} F(x,x',z)dxdx' = 1. \tag{3.27}$$

The transverse offset of the beam at longitudinal position z is then given by

$$\overline{x}(z) = \int_{-\infty}^{\infty}\int_{-\infty}^{\infty} xF(x,x',z)dxdx'. \tag{3.28}$$

The rms size of the beam is

$$\sigma_x^2(z) = \int_{-\infty}^{\infty}\int_{-\infty}^{\infty} (x-\overline{x})^2 F(x,x',z)dxdx'. \tag{3.29}$$

The quantity which is used in the accelerator physics to describe the beam size instead of σ_x is *emittance* ϵ_x. It is given as follows:

$$\epsilon_x = \frac{\sigma_x^2(z)}{\beta_x(z)}. \tag{3.30}$$

A beam with the uniform (Kapchinsky-Vladimirsky) transverse distribution has $\sigma_x = a/2$. Its rms emittance is expressed through the beam radius as follows:

$$\epsilon_x = \frac{a^2(z)}{4\beta_x(z)}. \tag{3.31}$$

If the energy of the beam is constant, then the emittance is preserved according to the Liouville's theorem. In case of the beam acceleration the quantity called the *normalized emittance* is preserved:

$$\epsilon_{x,n} = \epsilon_x \gamma\beta. \tag{3.32}$$

Taking into account Eq. 3.5 one sees that the dependence on z cancels and emittance does not depend on the longitudinal position. It is the invariant of the beam.

3.3.2 Coasting Beam Spectral Characteristics

Beams consist of the finite number of particles. Therefore, the parameters of the beam exhibit fluctuations. Such fluctuations are called the Schottky noise. In circular accelerators this noise has a certain structure. The spectral characteristics of this noise are very important. They make the beam more stable against the external disturbance [45, 52] and they can be used for the beam diagnostics [53, 49]. Suppose, there is an ideal current pick-up placed somewhere in accelerator. One particle with index j periodically passing this pick-up generates a Dirac comb signal

$$I_j(t) = Ze\omega_{0,j} \sum_{n=-\infty}^{\infty} \delta(\omega_{0,j}t + \theta_j - 2\pi n), \tag{3.33}$$

where $\omega_{0,j} = 2\pi f_{0,j}$ is the circular revolution frequency of the particle, θ_j is the initial phase shift depending on the particle's position in the beam. The total current signal of the beam is the sum of the currents of individual particles and is given by

$$I(t) = \sum_{j=1}^{N_i} I_j(t). \tag{3.34}$$

Each particle produces a Dirac comb with a slightly different period. The pick-up detects a linearly changing delay between individual particles (Fig. 3.4). In coasting beams θ_j is uniformly distributed in the interval $(0, 2\pi]$. In order to proceed with the analysis of the beam spectral characteristics, we make use of the Dirac comb Fourier series:

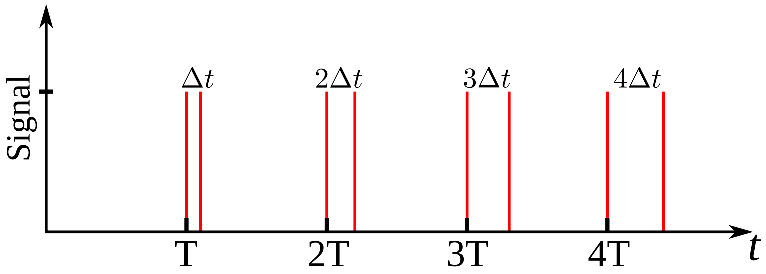

Figure 3.4.: Current seen by the pick-up in case of two particles with different momenta. Signal of an individual particle is Dirac's δ-function. The delay between the particle signals is growing with time.

$$2\pi \sum_{n=-\infty}^{\infty} \delta(\omega_{0,j} + \theta_j - 2\pi n) = \sum_{n=-\infty}^{\infty} e^{-in(\omega_{0,j}t+\theta_j)}. \tag{3.35}$$

We substitute this equation to Eq. 3.33 and extract the term with $n = 0$ from the sum yielding

$$I(t) = Ze\sum_{j=1}^{N_i} f_j + 2Ze\sum_{j=1}^{N_i}\sum_{n=1}^{\infty} f_j \cos\left[m(\omega_{0,j}t + \theta_j)\right]. \tag{3.36}$$

Here the imaginary parts have canceled. The periodic part of Eq. 3.36 also cancels giving the average current:

$$\overline{I}(t) \equiv Ze \sum_{j=1}^{N_i} f_j = ZeN_i f_0, \tag{3.37}$$

where overline means the averaging over the particles' ensemble. The current fluctuation signal is then given by

$$\delta I(t) \equiv 2Ze \sum_{j=1}^{N_i} \sum_{n=1}^{\infty} f_j \cos\left[m(\omega_{0,j} t + \theta_j)\right]. \tag{3.38}$$

One can see that this noise has a time structure. To find patterns in the signal, the autocorrelation function is used

$$C_I(t, t+\delta t) = \overline{\delta I(t) \delta I^*(t+\delta t)}, \tag{3.39}$$

where I^* is the complex conjugate of I. Applying Eq. 3.39 to Eq. 3.38 one gets

$$C_I(\delta t) \approx 2Z^2 e^2 f_0^2 \sum_{j=1}^{N_i} \sum_{n=1}^{\infty} \cos(n\omega_{0,j} \delta t) = 2Z^2 e^2 f_0^2 \sum_{j=1}^{N_i} \sum_{n=1}^{\infty} \cos\left[(1 - \eta \delta p_j) n \omega_0 \delta t\right], \tag{3.40}$$

where we have used Eq. 3.14 to tie together the momentum spread and the revolution frequency. The frequencies of the individual particles are approximated by the average revolution frequency. The current noise in frequency domain consists of equally spaced bands with the rms width given as follows:

$$\sigma_n = \omega_0 \frac{\Delta p}{p_0} \eta n, \tag{3.41}$$

where n is the number of a band.

In the transverse plane particles oscillate with the betatron frequency. Their dipole moment is represented by the δ-functions multiplied by the harmonic function:

$$d_j(t) = ZeX_j \omega_{0,j} \sum_{n=-\infty}^{\infty} \delta(\omega_{0,j} t + \theta_j - 2\pi n) \cos(Q_j \omega_{0,j} t + \phi_j), \tag{3.42}$$

where X_j is the electron amplitude, Q_j is the single particle betatron tune and ϕ_j is another uniformly distributed random phase. The average dipole moment then reads

$$\overline{d}(t) = \sum_{j=1}^{N_i} d_j(t). \tag{3.43}$$

Eq. 3.43 can be rewritten as

$$\overline{d}(t) = \frac{Ze}{2} \sum_{j=1}^{N_i} f_j X_j \sum_{n=-\infty}^{\infty} \left[\cos[(n - Q_j)\omega_{0,j} t - \phi_j + n\theta_j] + \cos[(n + Q_j)\omega_{0,j} t + \phi_j + n\theta_j] \right], \tag{3.44}$$

where Eq. 3.36 was used. Such behavior leads to the formation of the *betatron side bands*. Their position is given as follows:

$$\omega_{n,\pm} = \omega_0 (n \pm Q), \tag{3.45}$$

where "+" in the subscript marks a frequency of the *fast wave*, "−" is that of the *slow wave*. As it was shown in Section 3.1, chromaticity changes the betatron tune of the off-momentum particle. In case of the beam, it modifies the width of the side-bands:

$$\sigma_{n,\pm} = (\xi Q - \eta(n \pm Q))\omega_0 \frac{\Delta p}{p_0}. \tag{3.46}$$

One can see that the chromaticity depending on its sign can cancel or increase the damping. Usually it is chosen to increase the width of the lowest betatron side bands where the resistive wall impedance is high [54].

The features described above are used in the beam diagnostics [53]. Measuring the distance between the side-bands one can identify the tune working point. Using the measured width of the side-bands it is possible to extract the momentum spread and the chromaticity. It is important to say that external forces, e.g., impedance or electron cloud, can excite only the slow waves.

4 Collective Effects in Particle Beams

In the previous chapter the motion of noninteracting particles in an accelerator was discussed. In real situation the charged particles interact with the accelerator structures through the electromagnetic waves. These waves being modified by the beam surroundings act back on the beam. This interaction in accelerator physics is described in terms of *wake fields* and *impedances* [55, 56, 45]. Over many turns the effect of the impedance can resonantly sum up leading to an instability. The impedance concept is well-developed and very convenient to use in the beam equations of motion. That is why there were efforts to find similarities of the electron cloud effects with conventional impedances [18, 57, 58].

Not every impedance causes an instability. Longitudinal momentum spread leads to the Landau damping, which stabilizes the beam. However, particles interact with each other within the beam via direct space charge forces. The higher beam intensity gets, the stronger these forces are. Finally, the damping can be lost or the tune of the particles in the beam can be shifted towards the resonant line and the losses or the formation of halo can start.

In Section 4.1 the concept of wake fields and impedances is introduced. Section 4.2 is dedicated to Landau damping due to a betatron frequency spread. The effect of space charge tune shift is discussed in Section 4.3.

4.1 Impedances and Wake Fields

Consider a beam circulating in an accelerator with the average current $I(z)$. If a chamber around the beam is not perfectly conducting or has discontinuities, then there is always an electromagnetic wave left behind. This electromagnetic wave is called the *wake field*. It acts back on the beam. Over many turns the effect of wake fields can resonantly multiply leading to an instability. Furthermore, the energy emitted by the beam leads to the *energy loss*.

Let us proceed with the description of the interaction of two particles traveling through the accelerator structures. Let q_1 and $\vec{r_1}$ be the charge and the transverse position of the leading particle correspondingly. Whereas, q_2 and $\vec{r_2}$ are the corresponding parameters of the trailing charge. The longitudinal distance s between the two charges is measured from the leading charge in the direction opposite to the velocity. The first charge produces the fields $\vec{E}$ and $\vec{B}$, which act back on the charge itself and on the trailing particle. The work done by the fields of the leading particle on the trailing charge is proportional to the *wake potential*:

$$W(\vec{r_1}, s) = \frac{1}{q_1} \int_{-\infty}^{\infty} \left[\vec{E}(r_1, z, t) + \vec{v_z} \times \vec{B}(r_1, z, t) \right] dz, \tag{4.1}$$

where $t = (s + z)/v$.

The longitudinal component of the wake potential is

$$W_{||}(\vec{r}_1, s) = -\frac{1}{q_1}\int_{-\infty}^{\infty} E_{||}(\vec{r}_1, z, (s+z)/v)dz. \tag{4.2}$$

The wake potential can be expanded into series in terms of $\vec{r}_1$. Usually the monopole component $W_{||,0}(s)$ is dominant and we omit higher orders components in the latter discussion.

Similar to the longitudinal case one can define the *transverse wake potential*:

$$\vec{W}_{\perp}(\vec{r}_1, s) = \frac{1}{q_1}\int_{-\infty}^{\infty} \left[\vec{E}(r_1, z, t) + \vec{v}_z \times \vec{B}(r_1, z, t)\right]_{\perp} dz, \tag{4.3}$$

where only the transverse components of the electromagnetic force are taken into account. The dipole components of the transverse wake potential $W_{x,1}(s)$ and $W_{y,1}(s)$ are dominant in most cases.

The wake potentials defined above can be treated as Green functions, i.e., the response of the accelerator structures to the Dirac δ-function. They can be used to find the potentials of the macroscopic beam distributions. For this purpose the wake potentials should be convoluted with the beam line density. Longitudinal potential is then given as

$$V_{||}(s) = Ze\int_{-\infty}^{\infty} \lambda_i(s-s')W_{||,0}(s')ds' \tag{4.4}$$

and transverse is

$$V_x(s) = Ze\int_{-\infty}^{\infty} \lambda_i(s-s')W_{x,1}(s')x(s')ds', \tag{4.5}$$

where $x(s')$ is the local beam displacement. In the vertical plane everything is similar. As soon as these potentials are calculated, one can obtain the total energy loss of the beam per turn:

$$\Delta U = Ze\int_{-\infty}^{\infty} \lambda_i(s)V_{||}(s)ds = \int_{-\infty}^{\infty} I(\tau)V_{||}(\tau)d\tau, \tag{4.6}$$

where $I(\tau) = Ze\beta c\lambda_i(\tau)$ and $\tau = s/(\beta c)$. Energy loss per unit length can be then defined as

$$\frac{dU}{ds} = -Ze\int_{-\infty}^{\infty} \lambda_i(s)E_{||}(s)ds = -\int_{-\infty}^{\infty} I(\tau)E_{||}(\tau)d\tau. \tag{4.7}$$

These losses are due to the finite resistivity of the wall or different pipe discontinuities seen by the beam along its path.

So far we have talked about the wake fields. In accelerator physics the *impedances* defined in frequency domain are more convenient. They are obtained applying the Fourier transform to the wake functions. The *longitudinal coupling impedance* is given as follows:

$$Z_{||,0}(\omega) \equiv \int_{\infty}^{\infty} W_{||,0}(\tau)e^{-i\omega\tau}d\tau. \tag{4.8}$$

In transverse direction the *transverse dipole coupling impedance* is defined as

$$Z_x(x_1,\omega) \equiv -i\int_{\infty}^{\infty} W_{x,1}(\vec{r_1},\tau)e^{-i\omega\tau}d\tau. \tag{4.9}$$

Longitudinal impedances are measured in $[\Omega]$, transverse dipole impedances are measured in $[\Omega/m]$. A Fourier transform of Eq. 4.4 is

$$\tilde{V}_{||}(\omega) = \tilde{I}(\omega)Z_{||}(\omega), \tag{4.10}$$

where tilde defines a Fourier transform of the corresponding function. We can now rewrite the energy loss using the impedance definition:

$$\Delta U = \frac{1}{2\pi}\int_{-\infty}^{\infty} ReZ_{||}(\omega)|I(\omega)|^2 d\omega. \tag{4.11}$$

These losses can be observed in accelerators. Moreover, they should be compensated by the rf system. Let us analyze the case when the synchronous phase is zero. Particles are divided into bunches, but no acceleration happens. However, energy loss (Eq. 4.6) gradually decelerates the beam. To avoid this, ϕ_s should be shifted by $\Delta\phi_s$ given by

$$ZeV_0 sin(\Delta\phi_s) = \Delta U. \tag{4.12}$$

An approximate expression for the phase shift is

$$\Delta\phi_s \approx \frac{\Delta U}{ZeV_0}. \tag{4.13}$$

Similar effects happen in presence of an electron cloud. The effect of the electron cloud on the synchronous phase will be discussed in Section 5.3.

4.2 Instabilities and Landau Damping

In Section 4.1 it was shown that the beam fields modified by the accelerator structures act back on the beam. This situation was described by means of wake fields and impedances. One can substitute a given transverse dipole impedance $Z_{\perp,1}$ to the beam equation of motion and study its stability. Assuming a constant focusing, the motion of the particle in the coasting beam is described as follows [45]:

$$\left(\frac{\partial}{\partial t} + \omega_0\frac{\partial}{\partial\theta}\right)^2 x + \omega_\beta^2 x = iA\overline{x} = \frac{iZf_0^2eI_0Z_1^{\perp}L}{\beta E}\overline{x}. \tag{4.14}$$

One can immediately find the corresponding betatron frequency shift

$$\Delta\omega_\beta = -\frac{iZ\beta c^2}{2\omega_\beta E}\frac{eI_0}{L}Z_1^\perp. \tag{4.15}$$

The imaginary part of the transverse dipole impedance produces a real coherent frequency shift. If the resistive part of the impedance is positive, the instability occurs. The instability growth rate is given by

$$\frac{1}{\tau_{ins}} = \frac{Z\beta c^2}{2\omega_\beta E}\frac{eI_0}{L}ReZ_1^\perp. \tag{4.16}$$

The tune shift induced by the dipole impedance is *coherent*. It means that all particles at a certain longitudinal position see one and the same electromagnetic force.

In Section 3.3 the spectral characteristics of the beam transverse fluctuations were discussed. It was shown that the beam momentum spread induces a transverse tune spread. The oscillations of the kicked beam in this case are damped and the instability threshold appears. Below the threshold impedance value the beam stays stable. A similar effect was firstly discovered in plasma physics by Landau [59]. The underlying physics of this effect in accelerators is described in many textbooks and publications [45, 60, 52]. We will follow the analysis performed there. To investigate the stability of the beam let us assume that all the beam particles are initially at rest. At time $t = 0$ they get a horizontal displacement $x(\theta,0) = \sum_n x_{n,0}e^{in\theta}$. For simplicity, horizontal velocity is set to zero. Applying the double Fourier transform to Eq. 4.14 one gets

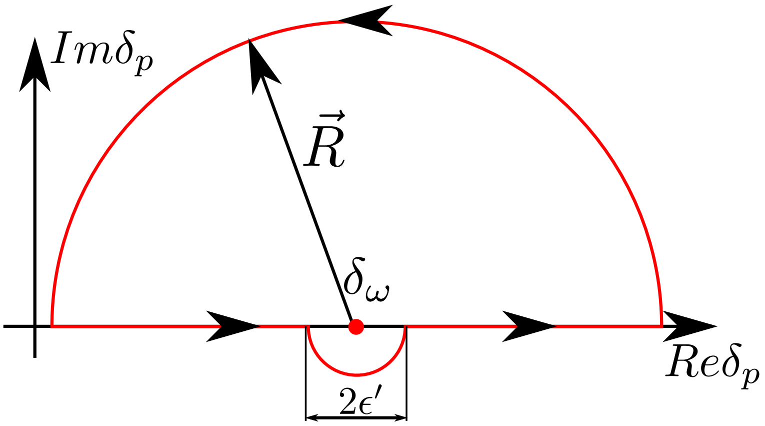

Figure 4.1.: Integration contour for the dispersion integral. The radius R of the big semicircle goes to infinity. The radius of the small semicircle ϵ' goes to zero.

$$\frac{i(\omega-2n\omega_0)x_{n,0}}{2\pi} + (\omega_\beta^2-(\omega-n\omega_0)^2)\tilde{x}_n(\omega) = iG\overline{\tilde{x}_n(\omega)}. \tag{4.17}$$

This algebraic equation can be solved yielding

$$\tilde{x}_n(\omega) = \frac{iG\overline{\tilde{x}_n(\omega)}}{\omega_\beta^2-(\omega-n\omega_0)^2} - \frac{ix_{n,0}}{2\pi}\frac{\omega-2n\omega_0}{\omega_\beta^2-(\omega-n\omega_0)^2}. \tag{4.18}$$

The revolution and betatron frequencies are connected with the particle momentum by virtue of Eq. 3.14 and Eq. 3.12. To proceed further we need to integrate this equation with the distribution function of the beam longitudinal momenta $F(\delta_p)$:

$$\overline{x}_n(\omega) = \frac{-ix_{n,0}(\omega - 2n\omega_0)\int_{-\infty}^{\infty}\frac{F(\delta_p)}{\omega_\beta^2-(\omega-n\omega_0)^2}d\delta_p}{2\pi\mathscr{H}(\omega)}, \tag{4.19}$$

where

$$\mathscr{H}(\omega) = 1 - iG\int_{-\infty}^{\infty}\frac{F(\delta_p)}{\omega_\beta^2-(\omega-n\omega_0)^2}d\delta_p \tag{4.20}$$

and $\mathscr{H}(\omega) = 0$ is the *dispersion relation* governing the stability of the beam. The expression under the integral sign in Eq. 4.20 can be rewritten as

$$\mathscr{H}(\omega) = 1 - \frac{iG}{2Q_\beta\overline{\omega}_0}\left[\int_{-\infty}^{\infty}\frac{F(\delta_p)}{Q_\beta\omega_0 - \omega + n\omega_0}d\delta_p + \int_{-\infty}^{\infty}\frac{F(\delta_p)}{Q_\beta\omega_0 + \omega - n\omega_0}d\delta_p\right]. \tag{4.21}$$

The integrals above have singularities at $\omega = \omega_0(n \pm Q_\beta)$. If the frequency ω is close to one of these poles, then the contribution of the corresponding term is large. Another term can be neglected in this case. Let us investigate the first integral from Eq. 4.21 assuming that $F(\delta_p)$ is narrow and contains only one of the two poles. In the vicinity of the slow wave frequency, Eq. 4.21 can be rewritten as

$$\mathscr{H}(\omega) = 1 - \frac{iG}{2Q_\beta\overline{\omega}_0}\left[\int_{-\infty}^{\infty}\frac{F(\delta_p)}{\omega - \overline{\omega}_0(n-\overline{Q}_\beta) - \delta_p\overline{\omega}_0[(n-\overline{Q}_\beta)\eta + \overline{Q}_\beta\xi]}d\delta_p\right], \tag{4.22}$$

where overline denotes the average value. We now make use of Eq. 3.46 and rewrite Eq. 4.22 as

$$\mathscr{H}(\omega) = 1 - \frac{iG\overline{\delta}_p}{2Q_\beta\overline{\omega}_0\sigma_{\beta,-}}\left[\oint_C\frac{F(\delta_p)}{\delta_\omega - \delta_p}d\delta_p\right], \tag{4.23}$$

where

$$\delta_\omega = \frac{\omega - \overline{\omega}_0(n-\overline{Q}_\beta)}{\overline{\omega}_0[(n-\overline{Q}_\beta)\eta + \overline{Q}_\beta\xi]} \tag{4.24}$$

is the linear function of excitation frequency ω. To proceed further we replace the integration path with a contour shown in Fig. 4.1. In the limit of infinite R and zero ϵ' one gets:

$$\oint_C\frac{F(\delta_p)}{\delta_\omega - \delta_p}d\delta_p = -i\pi F(\delta_\omega) + P.V.\int_{-\infty}^{\infty}\frac{F(\delta_p)}{\delta_\omega - \delta_p}d\delta_p, \tag{4.25}$$

where P.V. denotes the principal value of the integral. For the Gaussian momentum distribution, the principal value is connected with the complex error function:

$$P.V. \int_{-\infty}^{\infty} \frac{F(\delta_p)}{\delta_\omega - \delta_p} d\delta_p = -i\sqrt{\frac{\pi}{2}} \frac{1}{\overline{\delta}_p} e^{-\frac{\delta_\omega^2}{2\overline{\delta}_p^2}} erf\left(i\frac{\delta_\omega}{\sqrt{2}\overline{\delta}_p}\right). \tag{4.26}$$

If the excitation frequency is exactly in the middle of the side band frequency distribution, then Eq. 4.26 gives zero. Using Eq. 4.22 one can find the threshold G and corresponding instability increment (Eq. 4.16). The beam is stable if the growth rate predicted for the cold beam is lower than the Landau damping rate:

$$\frac{1}{\tau_{inst}} < \sqrt{\frac{2}{\pi}} \sigma_{\beta,-}. \tag{4.27}$$

Taking into account Eq. 3.46 one can obtain a threshold for each betatron side band

$$\frac{1}{\tau_{inst}} < \sqrt{\frac{2}{\pi}} (\xi Q_\beta - \eta(n - Q_\beta))\omega_0 \frac{\Delta p}{p_0}. \tag{4.28}$$

The instability threshold is the linear function of the side band number. One can see that the thresholds for each side band exist even for $\xi = 0$. Usually $\xi \neq 0$, because resistive wall impedance affects the lowest side bands.

The same derivations can be done for the fast wave. One can see from Eq. 4.21 that the excitation frequency in the fast wave term has the opposite sign. This means that the fast wave can be excited only by the negative real part of impedance.

4.3 Space Charge Tune Shift

The interaction of the beam particles happens not only via impedances and wake fields but also through the direct space charge. In the following description of this phenomenon is based on the CERN school lectures [61]. For simplicity let us assume a uniform beam with radius a. It has a line charge density $\lambda = \pi a^2 Ze\rho_i$ and velocity $v = \beta c$. The equation for its radial electric field is given as follows:

$$\frac{1}{r}\frac{d}{dr} rE(r) = \frac{Ze\rho_i}{\epsilon_0}. \tag{4.29}$$

The field expressed through the current $I = \beta c\lambda$ is

$$E(r) = \frac{I}{2\pi\epsilon_0 \beta c} \frac{r}{a^2}. \tag{4.30}$$

The azimuthal magnetic field is determined by another Maxwell equation:

$$\frac{1}{r}\frac{d}{dr} rB_\phi(r) = \mu_0 J, \tag{4.31}$$

where $J = \beta c Z e \rho_i$ is the current density. The solution of Eq. 4.31 is

$$B_\phi = \frac{I}{2\pi\epsilon_0 c^2}\frac{r}{a^2}. \tag{4.32}$$

Now we can calculate the total radial force acting on the beam particle using Eq. 3.1

$$F_r(r) = \frac{ZeI}{2\pi\epsilon_0\beta c}(1-\beta^2)\frac{r}{a^2} = \frac{ZeI}{2\pi\epsilon_0\beta c\gamma^2}\frac{r}{a^2}. \tag{4.33}$$

We now can include this force into Eq. 3.4:

$$x'' + \left(k_x(s) - \frac{ZeI}{2\pi\epsilon_0 a^2 A m_0 v^3\gamma^3}\right)x = 0, \tag{4.34}$$

where the time derivative was replaced by the derivative along the path s. The negative sign of the space charge term means that the overall focusing is reduced.

In real accelerator the size of the beam is defined by the local lattice parameters. To find the tune shift in this case, one should integrate the focusing error along the circumference

$$\Delta Q_x = \frac{1}{4\pi}\int_0^{2\pi R} K_{sc}(s)\beta_x(s)ds = \frac{ZeI}{8\pi^2\epsilon_0 A m_0 v^3\gamma^3}\int_0^{2\pi R}\frac{\beta_x(s)}{a^2(s)}ds. \tag{4.35}$$

The term under the integral gives the circumference length divided by four rms transverse emittances (Eq. 3.31). The tune shift is then simply

$$\Delta Q_x = -\frac{ZeIR}{16\pi\epsilon_0 A m_0 v^3\gamma^3\epsilon_x}. \tag{4.36}$$

In case of elliptical beam this expression is modified [61]:

$$\Delta Q_x = -\frac{ZeIR}{8\pi\epsilon_0 A m_0 v^3\gamma^3\epsilon_x(1+\sqrt{\overline{\beta}_y\epsilon_y/\overline{\beta}_x\epsilon_x})}. \tag{4.37}$$

The tune shifts presented above are *incoherent*. It means that each beam particle sees its own force.

The real beams usually have a transverse distribution close to Gaussian. In this case the space charge force is nonlinear and amplitude dependent. The tune shift of an individual particle starts to depend on its amplitude. That is why the so-called *space charge tune spread* appears. As intensity grows, the spread becomes larger. Some of the beam particles start to cross the resonant lines (Eq. 3.16) and get lost. At some point it becomes impossible to choose a stable working point.

5 Electron Cloud Effects

The electron cloud effect is a special case of the beam interaction with the surroundings. It can cause beam instabilities, emittance growth, dynamic pressure rise and additional heat load on the walls of the beam chamber [7, 62, 63, 64]. Electrons in the electron cloud are unwanted secondary particles accumulating in the beam pipe over many turns. There are several mechanisms leading to the electron cloud formation. They will be discussed in the upcoming sections.

The first observations of the electron cloud effects were made in 1960s [7]. The electron cloud phenomenon remains a field of active research, because it still affects the performance of several accelerator facilities in the world. In the LHC and the SPS electron clouds are the main limiting factor for the operation with the 25 ns bunch spacing [62]. For larger bunch spacings a synchronous phase shift due to the electron cloud was observed [40]. Other facilities encountering the electron cloud problem are the KEK [65] and the Cornel Electron Storage Ring [66].

In the past decades several accelerator facilities in the world were suffering from electron cloud induced instabilities, beam loss and emittance blow-up. Among them are the accelerators operating with short bunches [7, 18, 65] and the machines with long ones relative to the electron trapping wavelength [67, 68, 69]. In vast majority of the machines the multipactor condition is fulfilled and the electron cloud appears because of the significant secondary emission yield (SEY) from the wall.

During the operation with short bunches the electron cloud build-up happens after many bunch passages until the density is saturated. Secondaries are produced when the bunch field is not significant. This is seen in simulations and experiments [70]. In long intense bunches such as used in the SNS (Spallation Neutron Source) or the PSR (Proton Storage Ring) the maximum of the electron density can already be reached after one bunch passage [68, 67]. In this case the multipacting happens in the presence of the attracting field of the bunch tail. Under these conditions electrons are able to interact with the opposite sides of the pipe several times during one bunch passage thus, increasing the total yield per bunch.

Based on these observations the electron cloud was expected to threaten the operation of the FAIR project in Darmstadt. The main accelerator in this complex is the SIS-100 [12]. One of the main differences of the FAIR facility from the modern CERN facilities is the extensive use of coasting-beam-like long bunches during extraction. In many experiments the beam delivered from the SIS-100 should be continuous. Stored beam charge has the same order of magnitude as in the PSR or the SNS [67, 68, 12]. However, bigger circumference and smaller pipe size result into smaller transverse potentials and much smaller danger of multipacting. For realistic beam and pipe parameters simulations reveal the multipacting only for relatively high secondary emission yield [15]. These conditions can be avoided by a proper surface conditioning. The production of electrons from synchrotron radiation is also not relevant because of the particle mass. That is why the ionization of residual gas by beam ions becomes important.

A theory addressing accumulation of residual gas ions can be found in [17]. There were several recent works considering the problem of accumulation of the residual gas electrons and accompanying two-stream instability in coasting beams. In [71] the simulations with rigid slice beam were performed for coasting proton beams. It was found out that the linear two-stream instability threshold is quite inconsistent for the case of the residual gas electrons as compared to the simulations. In case of J-PARC the pressure in the vacuum chamber should be around 10^{-6} mbar to cause problems, which is too high for the actual machine.

In [72, 73] the problem of electron accumulation in coasting heavy ion beams was addressed. The author proposed an additional mechanism that can decrease the density of electron cloud. Continuous Coulomb collisions of the beam particles with electrons warm up the cloud leading to the diffusion of electrons towards the wall. Neutralization factor appears proportional to the pressure in the beam pipe. Thus, at sufficiently low pressures the electron density can be much below the instability threshold. However, the derivations in [72] are performed in absence of electron space charge for the simplified case assuming constant transverse beam density in the pipe.

In [74] electron-proton two-stream instability in coasting beam was studied using advanced δf 3D electromagnetic particle tracking simulations. It was found out that the linear small amplitude beam instability can be accompanied by the nonlinear instability at a later time. This happens because electrons gain big nonlinear amplitudes during initial linear instability and fluctuations of this bigger cloud later drive the beam unstable. The spectral characteristics of this nonlinear phase are not discussed. It was also found out that the instability threshold decreases with growing neutralization degree and increases with growing axial momentum spread. However, the question of simulations including electron production is left for the future. The phenomenological theory of nonlinear two-stream instability was proposed in [75].

As it was mentioned in the introduction, in the LHC the beams are always bunched. The main production mechanism there is the secondary electron emission, and the cloud builds-up in several microseconds. The bunches are short in a sense that the number of electron oscillations performed during the bunch passage is small. Most of the electrons during the interaction do not change their position significantly. They get a transverse kick from the passing bunch. The energy transfered to the electron cloud is then deposited to the wall.

In this chapter some specific features of the electron cloud interaction with positively charged beams are elaborated. In Section 5.1 the most important mechanisms of the electron cloud production such as secondary emission and residual gas ionization are discussed. In Section 5.2 a linear theory of electron trapping, coupled beam-electron motion, and Coulomb heating is explicated. The theory of this section is applied to the FAIR conditions. Section 5.3 is devoted to the wake fields and energy loss of relativistic proton bunches in electron clouds. This section is motivated by the LHC and the SPS observations.

5.1 Electron Cloud Production Mechanisms

In this Section only two of several possible mechanisms of electron production are discussed. Subsection 5.1.1 is devoted to the residual gas ionization. Electrons produced this way can accumulate in coasting beams or serve as seed electrons for the secondary emission. Subsection 5.1.2 explicates the interaction of electrons with the accelerator vacuum chamber and production of secondary electrons.

Such mechanisms as photon induced secondary emission and beam loss induced emission are not treated in this thesis. The first mechanism plays no role for heavy ions under FAIR conditions. The second mechanism plays role, for example, in the LHC. However, in the framework of this thesis the electron cloud build-up is not studied for the LHC conditions. In [76] for the SNS conditions it was pointed out that continuous beam losses in the collimator region can cause dangerous electron cloud build-up only if the multipacting is effective. In [15] it was shown that multipacting will hardly occur in the SIS-100.

5.1.1 Residual Gas Ionization

Early accelerators operating with coasting beams were suffering from the accumulation of the residual gas electrons in the field of the beam. A lot of studies were made at the time of the Intersecting Storage Rings (ISR) [17]. The project became fully functional only after the vacuum was improved by two orders from its initial value.

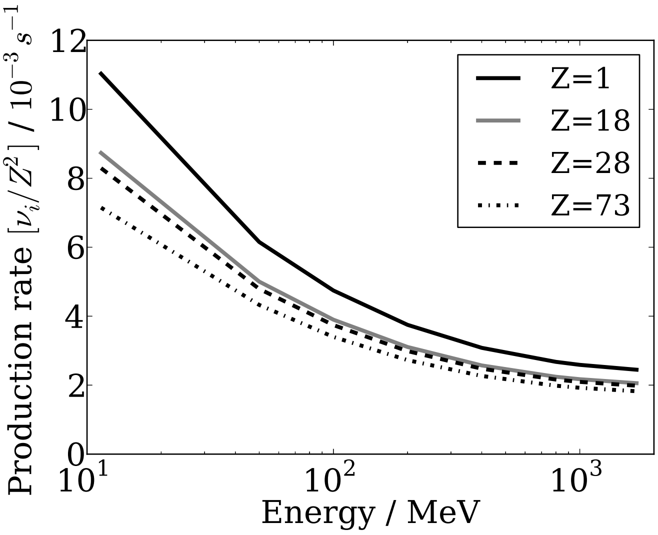

Figure 5.1.: Ionization rate of residual gas by beam ions for different charge states versus beam energy. The pressure is 10^{-11} mbar.

The average pressure in the LHC is 10^{-10} mbar [77, 78]. The design pressure in the SIS-100 is 10^{-12} mbar [13]. Other modern accelerator facilities have design vacuum pressure not lower than 10^{-9} mbar [79, 80]. At room temperature 1 mbar corresponds to the particle density $2.4 \cdot 10^{22}$ m^{-3}. Beams circulating in accelerators ionize residual gas species. The electrons produced this way can accumulate in the potential of coasting beam. In case of a bunched beam they can be accelerated by the varying beam potential towards the pipe wall. This can cause secondary emission, which is discussed in Section 5.1.2.

There are no exact formulae for the ionization cross sections. That is why to connect the production rate and residual gas pressure we have used the fit for cross sections proposed in [81]:

$$\sigma_{ion}(v, I_{nl}, Z_p) = \pi a_0^2 \frac{Z_p^2}{Z_p/Z_T + 1} N_{nl} \frac{E_{Ry}^2}{I_{nl}^2} G^{new} \left(\frac{v}{v_{nl}\sqrt{Z_p/Z_T + 1}} \right), \tag{5.1}$$

where $a_0 = 4\pi\epsilon_0\hbar^2/(m_e e^2) = 0.529 \times 10^{-11}$ m is the Bohr radius, Z_p is the projectile charge state, Z_T is the target nucleus charge, N_{nl} is the number of electrons in the orbital nl, $E_{Ry} = 27.2$ eV is the double Rydberg energy, I_{nl} is the ionization potential, v_{nl} is the electron orbital velocity. The fitting function is

$$G^{new}(x) = \frac{exp(-1/x^2)}{x^2}[1.26 + 0.283 \ln(2x^2 + 25)]. \tag{5.2}$$

These cross sections still scale with a very good precision $\propto Z^2$. This means that the ionization rate per one heavy ion is

$$\nu_i = \sigma_{cross}\rho_g\beta_0 c \propto Z^2, \tag{5.3}$$

where ρ_g is the residual gas density, σ_{cross} is the cross section, β_0 is the relativistic factor, c is the speed of light.

The ionization rate normalized to the beam intensity and Z^2 are shown in Fig. 5.1. It was calculated using Eq. 5.1 and Eq. 5.3 assuming that the pressure is 10^{-11} mbar. A snapshot of the real gas decomposition in the SIS-18 was used. Molecules are treated as the sum of separate atoms. The species used for our calculations are presented in Table 5.1. In the figure one can see that neutralization time $\tau_{neut} = Z/\nu_i \propto Z^{-1}$. It means that without any electron losses a U^{73+} beam will be completely neutralized 73 times faster than a proton beam with the same energy. Depending on the pressure conditions, there can be two ways of electron loss. At high production rates and small beam momentum spreads electron losses are predominantly due to the two-stream instability [71]. One can set a significant momentum spread obtaining a very stable beam. In this case the electron density is limited due to electron space charge around neutralization of 100% [17]. At low pressures collisions of electrons with beam particles will dominate [72]. These effects are discussed in the next subsections.

Table 5.1.: Main SIS-18 residual gas atoms

Species	Share / %	I_{nl} / eV	N_{nl}
C	13	11.26	4
H	84	13.59	1
O	3	13.61	4
He, Ar etc.	<1	—	—

5.1.2 Electron Induced Secondary Emission

Secondary emission is an important mechanism of electron production especially for bunched beams [65, 66, 62, 69, 67, 68, 82]. In this case the transverse electric field of the beam oscillates with radio frequency. This field periodically pulls the electrons existing in the chamber towards the bunch. After each bunch passage these electrons are released and fly towards the wall. If the wall has a high *secondary emission yield* (SEY), one impact electron may produce more than one secondary electrons. For some bunch spacings and intensities a resonant multipactor condition may occur. Secondary electrons produced after the initial impact get sufficient energy to produce new secondaries after the next bunch passage. This process leads to the exponential build-up of the electron cloud and is called the *beam induced multipacting*. Electron density saturates when the space charge potential of the electron cloud gets equal to the initial energy of secondary electrons E_s.

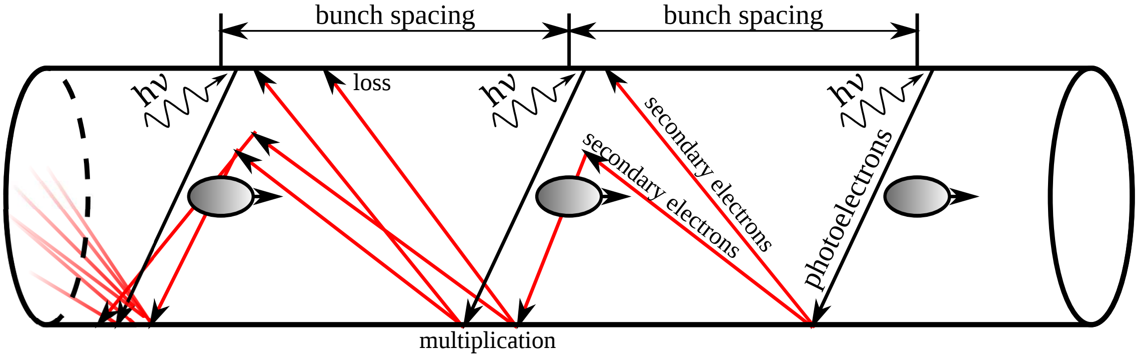

Figure 5.2.: Schematics of the multipacting process for short high-energy bunches. Initial electrons occur due to the synchrotron radiation or residual gas ionization and exponentially multiply because of the secondary emission. At very high energies the production of photoelectrons can become as strong as secondary emission.

Secondary electrons can be divided into three groups (Fig. 5.3) [83]. The first group is the reflected electrons. There exists a nonzero probability of the electron elastic reflection at low impact energies - δ_{refl}. Theoretical quantum mechanics calculations for the perfect boundary predict that $\delta_{refl,0} = 1$. In reality, however, this value is reduced because of the surface roughness and impurities. There is still no consensus on this question. The probability of the reflection [6] as a function of impact energy is

$$\delta_{refl}(E) = \delta_{0,refl} \frac{(\sqrt{E+E_0} - \sqrt{E})^2}{(\sqrt{E+E_0} + \sqrt{E})^2}, \tag{5.4}$$

where E is the energy of incident electron, $\delta_{0,refl}$ is the actual reflection coefficient at zero energy, E_0 is the energy parameter depending on the surface. Another group consists of the *rediffused electrons* - δ_{diff}. These are the impact electrons which random way in the surface brings them back to the vacuum chamber. Their energy distribution is almost uniform and ranges from the energy of reflected electrons down to zero. The third group of secondary electrons is the so-called *true secondaries* - δ_{true}. These electrons are released from the surface because of the impact electron energy deposition. Their average energy is typically several eV. An important feature of the electron secondary emission is its angular dependence. Incident electrons hitting the wall at grazing angles produce more electrons. It happens, because the stopping range of the electron lies close to the surface and newly born electrons can easier escape the wall. A full probabilistic model of the electron secondary emission was proposed in [83]. Usually, the term secondary emission yield refers to the $\delta_{SEY} = \delta_{diff} + \delta_{true}$. The

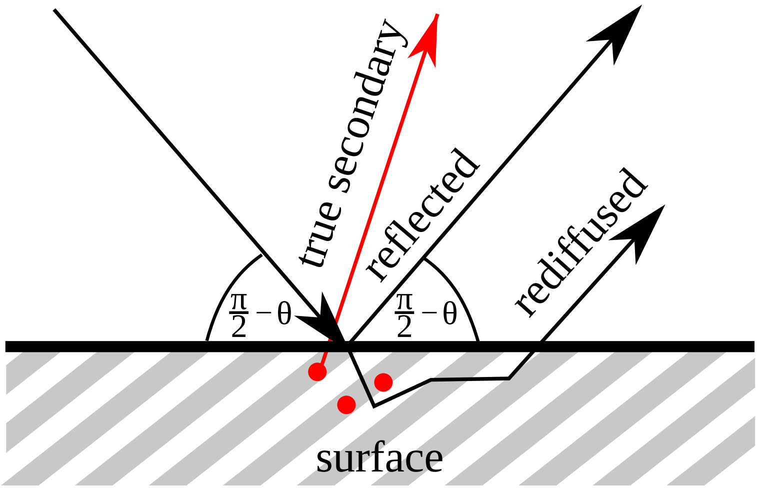

Figure 5.3.: Schematics of the electron interaction with the vacuum chamber wall. Incident electron can be absorbed, rediffused or reflected. Energy of the incident electron deposited in the wall can cause the release of secondary electrons.

typical behavior of the SEY and the reflection probability as a function of energy is shown in Fig. 5.4. A purely analytical expression for the SEY does not exist. In most cases fits to the experimental data are used. One of the possible fits is [83]

$$\delta_{SEY}(E) = \delta_{max} \frac{sx}{s-1+x^s}, \tag{5.5}$$

where $x = E/E_{max}$, E_{max} is the energy for which maximum SEY is reached, δ_{max} is the value of SEY at maximum, s is the fitting constant.

However, if the wall has a significant SEY, it does not always lead to the formation of the electron cloud. It is a matter of beam intensity and bunch spacing. In [15] it was shown that under the FAIR conditions the build-up in the SIS-100 happens for $\delta_{max} \approx 2.0$. This is a relatively high value for secondary emission yield and can be obtained by the proper conditioning of the wall. In the SIS-18 working as the injector to the SIS-100 the threshold is $\delta_{max} \approx 1.8$. In 2009 the SIS-18 upgrade to improve the beam life time was accomplished. During this period a special NEG coating to increase the pumping speed and decrease δ_{max} was introduced into approximately 65% of the circumference [84]. NEG coatings have SEY [85] lower than the threshold δ_{max} for the SIS-18, so the electron cloud problem will very likely not occur in the coated sections.

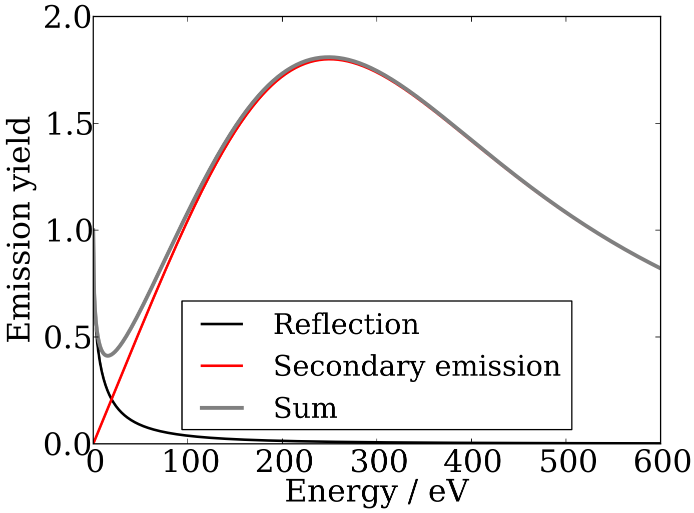

Figure 5.4.: Secondary emission yield and reflection coefficient as functions of electron energy.

5.2 Electron Cloud Effects in Long Bunches and Coasting Beams

In this section we analyze the electron cloud effects in the long bunches and coasting beams. This means that the number of electron oscillations performed in one turn is much bigger than 1. The main production mechanism assumed in this section is the residual gas ionization. Subsection 5.2.1 is devoted to the motion of an electron in the stable beam. The conditions for electron trapping are explicated. The reduction of the electron accumulation efficiency in the beam with perturbed linear density is analyzed. Subsection 5.2.2 describes some features of the coupled electron-beam motion in linear approximation. Features arising in case of heavy ion beams are explicated. Finally, in Subsection 5.2.3 the stochastic effects of electron collisions with the beam particles and their effect on the electron density are analyzed.

5.2.1 Single Electron Dynamics

In this subsection we explicate the motion of an electron in the field of long, coasting beam-like bunches. This is of interest, because the slow extraction of coasting beams is foreseen in the SIS-100 [12]. First, let us assume a beam with a line density slowly varying along the accelerator so that it does not vanish anywhere. An electron trapped in the field of such a beam will exhibit oscillations. The motion of electron in both planes is identical. Hereafter, all the effects are discussed for horizontal plane. Image currents and longitudinal fields, which can modify the electron behavior, are neglected as well as the beam field nonlinearities. The motion of electrons trapped in the vicinity of beam center is described by the following equation:

$$\ddot{x_e} + \omega_{e,x}^2(t, z_0)x_e = 0, \tag{5.6}$$

where $\ddot{x_e}$ is the second time derivative of the electron displacement and electron bounce frequency is

$$\omega_{e,x}(t, z_0) = Q_{e,x}(t, z_0)\omega_0 = \sqrt{\frac{Z\lambda_i(t)e^2}{2\pi\epsilon_0 m_e \sigma_{x,z_0}(\sigma_{y,z_0} + \sigma_{x,z_0})}}. \tag{5.7}$$

Here $Q_{e,x}$ is the electron bounce tune, ω_0 is the revolution frequency, Z is the charge state of beam particles, N_i is the number of beam particles, $\lambda_i(t)$ is the local electron line density, σ_{x,z_0} and σ_{y,z_0} - horizontal and vertical rms beam size, z_0 reflects the fact that the electron motion is studied at a fixed location in accelerator.

In case of harmonic oscillations and slow ($\dot{\omega}_e \lesssim \omega_e^2$) variation of focusing force the Hamiltonian is [86]

$$H = \frac{m_e\omega_e^2 x_e^2}{2} + \frac{m_e V_e^2}{2} = \frac{m_e\omega_e^2 X_e^2}{2} = \omega_e J, \tag{5.8}$$

where X_e is the electron oscillation amplitude, J is the adiabatic invariant. From Eq. 5.8 follows

$$X_{e,max} = X_{e,0}\sqrt{\frac{\omega_{e,0}}{\omega_{e,min}}} = X_{e,0}\sqrt[4]{\frac{\lambda_{i,0}}{\lambda_{i,min}}}, \tag{5.9}$$

where $X_{e,max}$ is the maximal amplitude of the electron, $X_{e,0}$ is its initial amplitude, $\omega_{e,0}$ and $\lambda_{e,0}$ are the initial trapping frequency and the line density correspondingly, $\omega_{e,min}$ and $\lambda_{e,min}$ are minimal values. One sees that if at some point $\lambda_i = 0$, then the amplitude goes to infinity i. e., electron hits the wall. In reality the field outside the beam goes down nonlinearly and the amplitude increases even stronger.

If the beam parameters do not change in time, then $\omega_e(t) = \omega_e(t + L/(\beta_0 c))$ is the periodic function. Eq. 5.6 becomes a Hill's equation. It can give finite solutions [45] when the adiabatic theory predicts a singularity. Eq. 5.6 is solved similar to the case of the beam motion in a periodic focusing lattice of accelerator:

$$x_e(t) = \sqrt{\beta_0^e \epsilon_{e,x}}\sin(\psi_e(t) + \phi_0). \tag{5.10}$$

Here $\beta_0^e = \beta^e(t_0, t)$ is the amplitude function of the electron produced at time t_0, $\epsilon_{e,x}$ is the size of electron in phase space similar to the particle emittance, $\psi_e(t)$ is the periodic phase and ϕ_0 is the constant phase shift obtained from initial conditions. One can introduce other electron Twiss parameters $\alpha_{e,0} = \alpha_e(t_0, t)$ and $\gamma_{e,0} = \gamma_e(t_0, t)$ as it is done in the beam optics [46].

Based on these electron Twiss parameters one can construct a transfer matrix

$$M_e = \begin{bmatrix} \cos(\psi) + \alpha_{e,0}\sin(\psi) & \beta_0^e \sin(\psi) \\ -\frac{1+\alpha_{e,0}^2}{\beta_0^e}\sin(\psi) & \cos(\psi) - \alpha_{e,0}\sin(\psi) \end{bmatrix}. \tag{5.11}$$

The motion is stable if

$$Tr(M_e) < 2. \tag{5.12}$$

This matrix relates electron coordinates $(x_{e,0}, V_{e,0})$ to $(x_{e,1}, V_{e,1})$ after one revolution period via

$$\begin{pmatrix} x_{e,1} \\ V_{e,1} \end{pmatrix} = M_e \begin{pmatrix} x_{e,0} \\ V_{e,0} \end{pmatrix}. \tag{5.13}$$

In case of stable motion, electron coordinates in phase space satisfy

$$\gamma_{e,0} x_e^2 + 2\alpha_{e,0} x_e V_x + \beta_0^e V_x^2 = \epsilon_{e,0}. \tag{5.14}$$

If the electron is produced with zero initial velocity, then its emittance is simply

$$\epsilon_{e,0} = \gamma_{e,0} X_{e,0}^2. \tag{5.15}$$

The electrons produced at equal distances from the beam center but at different moments of time have different initial emittances. The motion of electron along the time axis is similar to the motion of beam particle along longitudinal direction. At some point electron gets to the place with maximal electron beta function β_{max}^e. Here it will exhibit a peak deviation from the pipe axis given by

$$X_{e,max} = \sqrt{\epsilon_{e,0}\beta_{max}^e} = X_{e,0}\sqrt{\gamma_{e,0}\beta_{max}^e}. \tag{5.16}$$

If $\lambda_i(t) \neq 0$ and we increase the beam intensity N_i, then

$$\lim_{N_i \to \infty} \gamma_{e,0}\beta_{max}^e = \sqrt{\frac{\lambda_{e,0}}{\lambda_{e,min}}}. \tag{5.17}$$

Fig. 5.5 shows how the solution of Hill's equation gets closer to the adiabatic one with growing beam intensity.

Let us include the information about the electron production and the beam size into our approximation. First, the beam is assumed to be round and uniform transversely, i.e., having

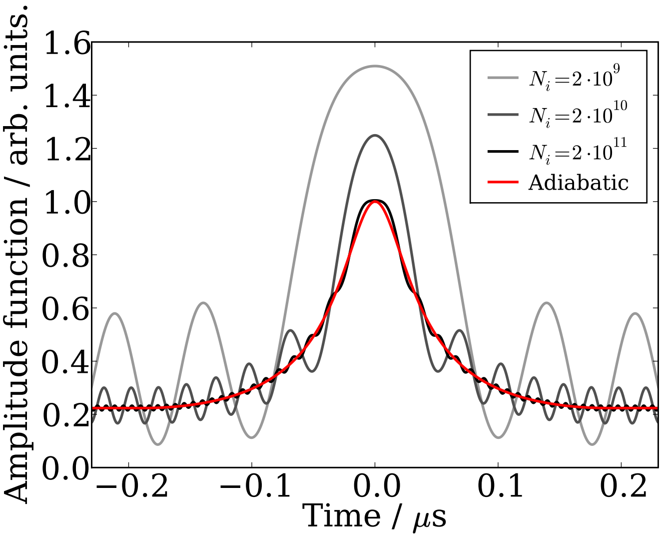

Figure 5.5.: The amplitude functions obtained for sausage-like U^{73+} beam using the adiabatic theory and the strict solution of Hill's equation. Gap in the beam has a cosine profile with 5% density in the middle. Total gap length is 10% of SIS-100 circumference.

Kapchinsky-Vladimirsky (KV) distribution with radius a. Second, let the electrons be produced proportionally to the local density, i.e., uniformly inside the beam. We assume that the electron with $X_{e,max} > a$ becomes unstable and hits the wall within several revolution periods. Electrons produced at the distances $x_{e,0} < a/\sqrt{\gamma_{e,0}\beta^e_{max}}$ will accumulate. The ratio of electrons that accumulate in point z_0 to the total amount produced in one revolution is then given by

$$\delta_{e,z_0} = \frac{1}{T\overline{\lambda_i}} \int_0^T \frac{\lambda_i(t)}{\gamma_e(t)\beta^e_{max}} dt, \tag{5.18}$$

where $T = L/\beta c$ is the revolution period, $\overline{\lambda_i}$ is the average beam line density. The dependence on line density comes from the fact that the local electron production rate depends on the local beam density. If a strong dipole magnetic field is applied and the average electron Larmor radius is much smaller than the beam size, then

$$\delta_{e,z_0} = \frac{1}{T\overline{\lambda_i}} \int_0^T \frac{\lambda_i(t)}{\sqrt{\gamma_e(t)\beta^e_{max}}} dt. \tag{5.19}$$

The area is increased because the electrons are frozen in one direction. Stable production areas within the round KV beam are illustrated in Fig. 5.6.

The real beam is elliptic. It means that $\omega_{e,x} \neq \omega_{e,y}$. To be trapped electron transfer matrices in both planes should satisfy Eq. 5.12. If they do, then the survival ratio is given as follows

$$\delta_{e,z_0} = \frac{1}{T\overline{\lambda_i}} \int_0^T \frac{\lambda_i(t)}{\sqrt{\gamma_{e,y}(t)\beta^e_{y,max}\gamma_{e,x}(t)\beta^e_{x,max}}} dt. \tag{5.20}$$

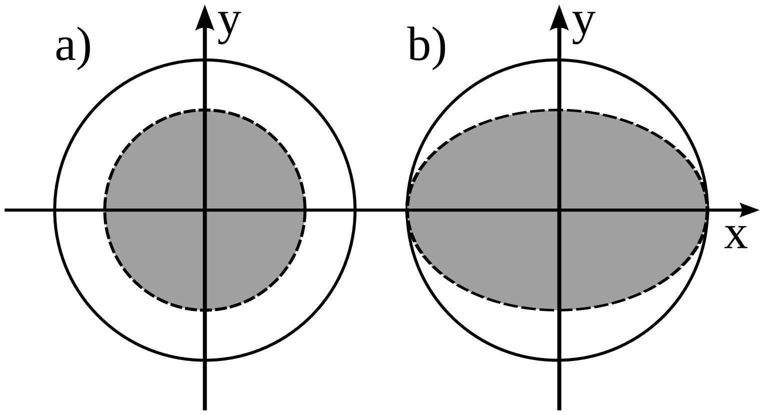

Figure 5.6.: Areas of stable electron accumulation for round KV beam. The solid line encloses the beam area confined between two barrier rf waves. Stability condition 5.12 is satisfied. The dashed line encloses the area of stable accumulation. a) drift section b) dipole section.

Up to now the electron trapping has been considered in the KV beam with a sharp, well-defined border. In case of Gaussian transverse profile, electrons are produced with large frequency spread. Their motion is governed by the nonlinear Hill's equation. Approximately 60% of them are produced outside the rms radius σ_r. Around 29% of all electrons are produced in the region where focusing force decreases with distance (Fig. 5.7). According to the assumptions made for KV beam, these electrons should be lost. The realistic situation can only be studied in the particle tracking simulations. This is done in Section 7.1.5.

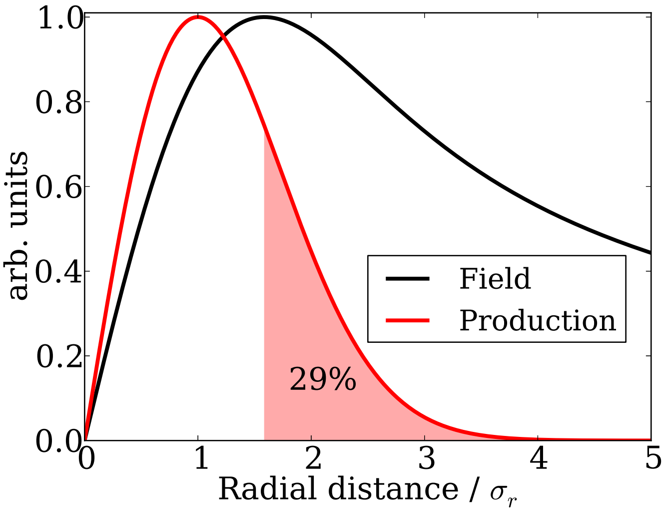

Figure 5.7.: Electric field of the round Gaussian beam in cylindrical geometry together with the production rate per unit of radial distance. 60% of electrons are born outside the rms radius. 29% of all electrons are born in the region of decaying field.

5.2.2 Two-Stream Instability

In Section 5.2.1 we have discussed the electron motion in the transverse field of the fixed beam. In reality the motion of the electrons and the beam particles is coupled. Let x_i and x_e be the transverse displacements of ions and electrons from the beam axis. The system of coupled equations of motion is then given as follows [45, 87]

$$\begin{cases} \left(\frac{\partial}{\partial t} + \omega_0 \frac{\partial}{\partial \theta}\right)^2 x_i + \omega_\beta^2 x_i = \omega_i^2 (x_i - \bar{x}_e) + \omega_{i,s}^2 (x_i - \bar{x}_i) \\ \frac{d^2 x_e}{dt^2} = -\omega_e^2 (x_e - \bar{x}_i) + \omega_{e,s}^2 (x_e - \bar{x}_e) \end{cases}, \tag{5.21}$$

where $\bar{x}_e$ and $\bar{x}_i$ are the centroid displacements of the electron cloud and charged particle beam from the pipe center, x_e and x_i are the single particle displacements, ω_e is defined in Eq. 5.7 and

$$\omega_i = \omega_0 Q_i = \sqrt{\frac{Z n_e e^2}{2\pi\epsilon_0 A m_0 L \sigma_x (\sigma_x + \sigma_y) \gamma_0}} = \omega_0 Q_e \sqrt{\chi_e \frac{Z m_e}{\gamma_0 A m_0}}, \tag{5.22}$$

where we have defined electron trapping tune Q_e and ion trapping tune Q_i. In linear case averaging over the ion and electron displacements removes the space-charge terms. Neglecting the transient effects we assume that the solutions for the electron and beam centroids are

$$\overline{x}_i \propto e^{i(n\theta - \Omega t)} \ , \ \overline{x}_e \propto e^{i(n\theta - \Omega t)}. \tag{5.23}$$

Substituting Eq. 5.23 to Eq. 5.21 one obtains the following algebraic equation:

$$(Q^2 - Q_e^2)\left[(n - Q)^2 - Q_\beta^2 - Q_i^2\right] - Q_e^2 Q_i^2 = 0, \tag{5.24}$$

where $Q = \Omega/\omega_0$ is unknown and $Q_\beta = \omega_\beta/\omega_0$ is the betatron tune. If Q is the complex number, then the instability occurs. In [45] one can find the approximate solutions for this equation. The main result is that even without any electron or beam tune spreads the equation describes a threshold behavior. Not every electron cloud density causes the instability. In the same source it is also shown that these thresholds are underestimated. The exact solution of Eq. 5.24 is shown in Fig. 5.8. It is seen that if the electron frequency matches the frequency of the slow wave (Eq. 3.45), then the instability starts even for electron density approaching zero.

In reality the beam has its own momentum spread dp/p_0 and tune spread ΔQ_β. Electrons interact with nonlinear transverse field of the beam. This leads to a spread in electron frequency ΔQ_e. Another source of the electron frequency spread can come from the varying beam size depending on the local lattice parameters.

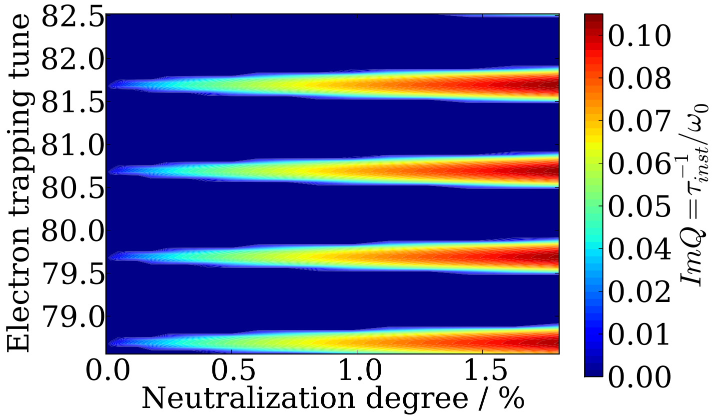

Figure 5.8.: Instability growth rate $Im(Q)$ i.e., solution of Eq. 5.24 as a function of electron trapping tune and neutralization degree for U^{73+}. Beam energy is $E = 1GeV/u$. Betatron tune is $Q_\beta = 21.308$.

The stability condition in case of tune spreads was obtained in [45, 88] and is given as follows:

$$\frac{\sqrt{\Delta Q_\beta^2 - 4\Delta Q_{sc}^2}}{Q_\beta} \cdot \frac{\sqrt{\Delta Q_e^2 - \chi_e^2 Q_e^2}}{Q_e} \gtrsim \frac{Q_i^2}{Q_\beta^2}, \tag{5.25}$$

where ΔQ_{sc} is the space charge tune shift and $\chi_e Q_e$ signifies the shift of the electron frequency due to its own space charge. From this equation it follows that if the neutralization factor approaches the width of the electron frequency distribution, then the loss of damping happens. However, in real situation the electron space charge does not change the spread due to the varying beam size and there should exist some finite threshold.

One peculiarity of the heavy ion synchrotron is that it operates with the particles having a broad variety of mass A and charge Z states. The main constraint for the beam intensity is the space charge limit. For machine operating with heavy ions we assume that tune shift should be one and the same for all the elements and is given by [61]

$$\Delta Q_y = -\frac{2N_i Z^2 g_f}{\pi A \beta^2 \gamma^3 B_f (\epsilon_y + \sqrt{\epsilon_y \epsilon_x})} \propto \frac{N_i Z^2}{A}, \tag{5.26}$$

where B_f is the bunching factor, $\epsilon_{x,y}$ is the transverse emittances, N_i is the number of beam particles, A is the mass number, Z is the charge state, β and γ are the relativistic parameters. From the equation above the scaling for the beam intensity follows:

$$N_i \propto \frac{A}{Z^2}. \tag{5.27}$$

Assuming that different beams have one and the same transverse emittance i.e., beam size, the electron trapping frequency 5.7 is $\omega_e \propto \sqrt{A/Z}$.

At this moment let us assume that the relative spread of the electron trapping frequency, $\Delta Q_e/Q_e \approx const$, is independent of the beam species. Taking into account Eq. 5.22 one gets the stability condition as a function of neutralization factor

$$\frac{\Delta Q_\beta}{Q_\beta} \cdot \frac{\sqrt{\Delta Q_e^2 - \chi_e^2 Q_e^2}}{Q_e} \gtrsim \frac{Q_e^2}{Q_\beta^2} \chi_e \frac{Z m_e}{\gamma_0 A m_0}. \tag{5.28}$$

When the electron trapping frequency is determined by the beam space charge limit Eq. 5.27, one finds that the threshold neutralization degree does not depend on the type of particle. However, limiting ourselves with the round Gaussian beam, we can derive the dependence of the instability threshold on the beam intensity

$$\frac{\Delta Q_\beta}{Q_\beta} \cdot \frac{\sqrt{\Delta Q_e^2 - \chi_e^2 Q_e^2}}{Q_e} \gtrsim \frac{\chi_e}{\omega_0^2 Q_\beta^2} \frac{Z^2 N_i e^2}{2\pi\epsilon_0 \sigma_x(\sigma_x + \sigma_y) L \gamma_0 A m_0}. \tag{5.29}$$

The simulations performed for this thesis were made neglecting the space charge of the electron cloud. For this reason it is useful to find out the threshold neutralization without the electron space charge:

$$\chi_{e,0} \approx \frac{2\pi\epsilon_0 \omega_0^2 \sigma_x(\sigma_y + \sigma_x) L \gamma_0 A m_0}{Z^2 e^2 N_i} Q_\beta \Delta Q_\beta \frac{\Delta Q_e}{Q_e}. \tag{5.30}$$

Substituting this equation to Eq. 5.29 one gets

$$\chi_e = \frac{\chi_{e,0} \frac{\Delta Q_e}{Q_e}}{\sqrt{\chi_e^2 + \frac{\Delta Q_e^2}{Q_e^2}}}. \tag{5.31}$$

One sees that the threshold neutralization degree is always lower than the relative electron frequency spread. The time to reach the threshold is

$$t_i = Z\chi_e/\nu_i. \tag{5.32}$$

Taking into account Eq. 5.27 and Eq. 5.3 one sees that $t_i \propto Z^{-1}$ for constant ρ_g. However, the dynamic vacuum, i.e, ρ_g depends strongly on the beam energy and specie type [89, 90]. Therefore, t_i to reach the threshold can be significantly modified. Nevertheless, one sees that t_i goes to infinity in the limit of small ionization rates.

The thresholds obtained above assume, basically, that the electrons are linear oscillators with the constant frequency spread. In reality, however, electrons change their amplitudes and frequencies during the interaction with the beam. In [74, 75] for long, coasting-beam-like bunches, it was shown that the electron distribution can reconfigure leading to the nonlinear instability in a long term. However, the studies were made for the PSR conditions where the electron cloud production was dominated by the secondary electron emission.

The dynamic picture including the electron cloud production and its interaction with the wall is also not described by the linear model and was not considered in [74, 75]. The simulations performed for J-Parc [91, 71] show that the electron cloud in some cases can induce a very small beam oscillations. The latter itself cause electrons to diffuse and get lost on the wall. The motion of electron in this case is nonlinear as follows from the beam potential. Self-consistent electron density and beam amplitude can be obtained only in simulations. The simulations of the instability together with the electron production are performed in Chapter 7.

5.2.3 Coulomb Scattering

An additional mechanism leading to the electron loss was proposed in [72, 73]. These proceedings make use of the fact that the beam consists of a finite number of particles. These particles collide with the electrons and transmit transverse kinetic energy to them. The electrons are lost when their energy becomes larger than the potential between the beam center and the wall. In some cases this mechanism leads to the saturation of the electron density below the instability threshold. However, this process was studied in a simplified manner. The beam size was assumed to be equal to the pipe size and no electron space charge was included. We study this effect in greater details.

One electron colliding with a charged particle experiences a transverse momentum kick given as follows [86]:

$$\Delta p_{\perp,e} = m_e \Delta v_\perp \approx \frac{Ze^2}{2\pi\epsilon_0 v b} = \frac{2Zr_e c m_e}{\beta_0 b}, \tag{5.33}$$

where b is the *impact parameter*, r_e is the *classical electron radius*. When an electron is a subject of multiple collisions with beam particles, one can find the average energy transfered to it in a unit of time:

$$D_h = \frac{1}{2m_e}\int_{b_{min}}^{b_{max}} 2\pi\Delta p_{\perp,e}^2(b)\beta c\rho_i(b) b\, db = E_0 \frac{4\pi c\rho_i Z^2 r_e^2}{\beta}\ln\Lambda, \tag{5.34}$$

where $ln\Lambda = 10$ is the Coulomb logarithm reflecting the ratio of b_{min} and b_{max}, ρ_i is the beam particle density, E_0 is the electron rest energy. The exact value of $ln\Lambda$ under the accelerator conditions is not studied within the framework of this dissertation. Transfer of energy D_h happens due to many random interactions with beam particles. Electron motion is governed by the second order stochastic differential equation:

$$m_e\ddot{\vec{r}} - \vec{F}(\vec{r}) = \vec{\phi}(\vec{r}, t), \tag{5.35}$$

where $F(\vec{r})$ is the force from the beam seen by the electron, $\vec{\phi}(\vec{r}, t)$ is the noise term due to the Coulomb collisions. The noise term satisfies

$$\overline{\vec{\phi}(\vec{r}, t) \cdot \vec{\phi}(\vec{r}, t + t_0)} = 2m_e D_h(\vec{r})\delta(t_0), \tag{5.36}$$

where the overline $\overline{(...)}$ denotes the averaging, $\delta(t_0)$ is the Dirac delta function, and $D_h(\vec{r})$ is the function of $\vec{r}$, because the collision rate depends on the local density. If the force is linear, then Eq. 5.35 describes a nonergodic two-dimensional Ornstein-Uhlenbeck process [92, 93]. The motion of the electron ensemble in this case is not described by the Fokker-Planck equation. In absence of the external force $\vec{F}(\vec{r})$, the Coulomb collisions lead to the growth of the average electron velocity according to

$$\overline{V}^2(t) = \frac{2D_h t}{m_e}. \tag{5.37}$$

It is equivalent to the linear growth of its average energy

$$E(t) = E_0 + D_h t, \tag{5.38}$$

where E_0 is the electron initial energy. It was shown [94] that Eq. 5.38 holds for the total energy of the particle trapped in a harmonic potential.

First, let us follow the assumptions of negligible electron space charge and uniform filling of the round pipe by the beam in 2D. Let R_p be the transverse half-width of the pipe. In this case a Poisson equation for the beam potential is given as follows:

$$\frac{1}{r}\frac{d}{dr}r\frac{dU(r)}{dr} = \frac{Ze\rho_i}{\epsilon_0}, \quad U(R_p) = 0, \quad \frac{dU}{dr}(0) = 0. \tag{5.39}$$

The depth of the potential well is then

$$U_0 = \frac{Ze\rho_i a^2}{4\epsilon_0} \tag{5.40}$$

and the average energy of the newly produced electrons is

$$E_{born} = \frac{2}{a^2}\int_0^a rU(r)dr = \frac{1}{2}U_0 = \frac{Ze\rho_i a^2}{8\epsilon_0}. \tag{5.41}$$

Based on Eq. 5.38, one can estimate the average electron density using

$$n_e = \nu_i \rho_i \frac{U_0 - E_{born}}{D_h} = \nu_i \rho_i \frac{U_0}{2D_h} = \nu_i \rho_i t_{life}, \tag{5.42}$$

where we have introduced t_{life} meaning the average life time of the electrons. From this equation we see that in case of negligible electron space charge, the electron density scales linearly with the production rate ν_i. Taking into account Eq. 5.1, Eq. 5.34 and Eq. 5.40 one sees that for $\rho_g = const$ the neutralization factor $\chi_e = n_e/(Z\rho_i)$ is the same for beam species with arbitrary Z:

$$\chi_e = \frac{\beta e a^2 \nu_i}{32\pi\epsilon_0 E_0 c Z^2 r_e^2 \ln\Lambda} \approx const. \tag{5.43}$$

This means that sustaining high vacuum during the operation with all the ions will equally prevent them from instability. For a fixed pressure and beam parameters, the neutralization is the function of beam emittance and energy.

However, in cylindrical geometry not all the electrons with the *total energy* $E_t > U_0$ hit the wall. We can separate all the electrons into two groups. The electrons in the first group have $E_t < U_0$ and are never lost. The electrons in the second group have $U_0 \leq E_t < 2U_0$ and are lost depending on their axial momentum. Electrons' integral of motion in this case is

$$\frac{m_e V_\phi^2}{2} + \frac{m_e V_r^2}{2} + \frac{Ze^2 \rho_i r^2}{4\epsilon_0} = E_t, \tag{5.44}$$

where V_ϕ is the azimuthal component of electron velocity and V_r is the radial component of velocity. The axial momentum is

$$M_e = m_e V_\phi r. \tag{5.45}$$

The equation for electron maximum deviation R_e is

$$\frac{M_e^2}{2m_e R_e^2} + \frac{Ze^2 \rho_i R_e^2}{4\epsilon_0} = E_t. \tag{5.46}$$

Solving this equation one gets the maximum achievable momentum for a given energy:

$$M_{e,max} = \sqrt{\frac{2\epsilon_0 m_e}{Ze^2 \rho_i}} E_t = \frac{E_t}{\omega_e} \tag{5.47}$$

and M_e for which the maximum deviation is smaller than R_p:

$$M_e^2 > 2m_e E_t R_p^2 - \frac{m_e Z e^2 \rho_i R_p^4}{2\epsilon_0}. \tag{5.48}$$

This peculiarity of the motion means that in 2D more electrons survive than it is given by Eq. 5.42. Basically, using Eq. 5.42 is equivalent to the assumption of only radial electron motion. However, the fraction of these additionally surviving electrons is of the order of 10%. This difference arises in the realistic simulations (Chap. 7).

What happens if the electron space charge is not negligible? The potential of the beam is distorted in the following manner

$$\frac{1}{r}\frac{d}{dr} r \frac{dU(r)}{dr} = \frac{\rho_i - e n_e(r)}{\epsilon_0}. \tag{5.49}$$

To estimate the effect of the electron space charge one can assume that

$$U(r) = U_0(r)(1 - \chi_e), \tag{5.50}$$

where $U_0(r)$ is the potential of the beam without electrons, $\chi_e = \overline{n_e}/(Z\overline{\rho_i})$ is the neutralization factor, $\overline{n_e}$ and $\overline{\rho_e}$ are the average electron and beam densities. The average life time is then given as

$$t_{life} = t_{life,0}(1 - \chi_e), \tag{5.51}$$

where $t_{life,0}$ is the life time in case of neglected electron space charge. Substituting this equation to Eq. 5.42 one gets the approximate solution for neutralization degree:

$$\chi_e = \frac{\chi_{e,0}}{1 + \chi_{e,0}}, \tag{5.52}$$

where $\chi_{e,0}$ is the neutralization degree without the space charge effect. Fig. 5.9 shows the dependence of the estimated neutralization degree on the beam energy for the SIS-100 parameters. One can see that the complete 100% neutralization is predicted for 10^{-9} mbar. Below this value the Coulomb collisions affect the neutralization. For the design pressure of 10^{-12} mbar the neutralization is everywhere below 1%. It should be mentioned that already at 10^{-10} mbar charge exchange beam losses become very significant [13]. This pressure is avoided by the SIS-100 design.

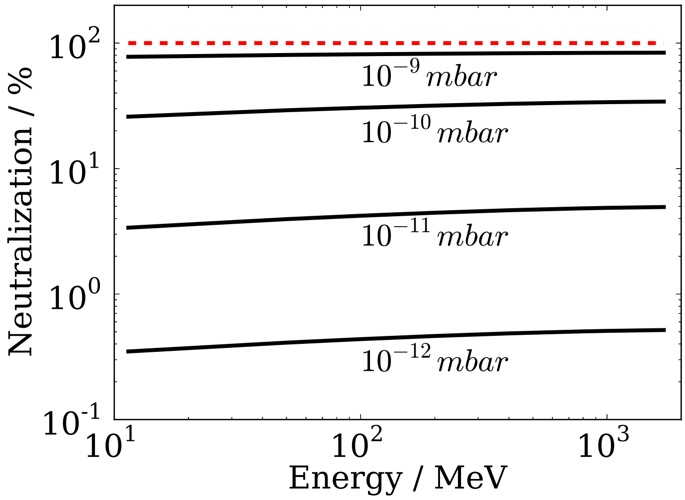

Figure 5.9.: Neutralization degree as a function of energy for different pressures and beam uniformly filling the round pipe(a=5 cm).

So far we have treated the case of a thick beam filling completely the beam pipe ($a = R_p$). In the following we will treat the case of $a < R_p$. Under such conditions the motion of an electron is nonlinear. Furthermore, the heating rate becomes a function of electron position. The beam potential well depth is

$$U_0 = \frac{Ze\rho_i}{2\epsilon_0}\left(\frac{1}{2} + \ln\frac{R_p}{a}\right) = \frac{m_e\omega_e^2 a^2}{e}\left(\frac{1}{2} + \ln\frac{R_p}{a}\right). \tag{5.53}$$

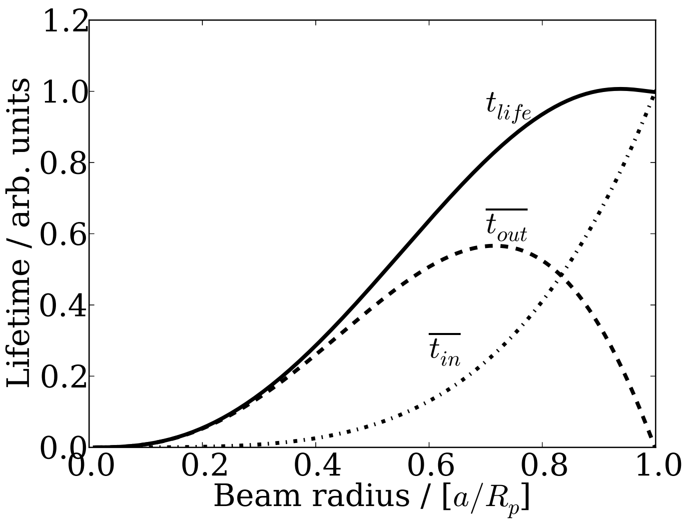

Figure 5.10.: Average electron life time t_{life} versus beam size in cylindrical geometry assuming only radial electron motion. $\overline{t_{in}}$ is the average time spent with amplitudes $x < R_p$. $\overline{t_{out}}$ is the time needed to reach the wall from beam border.

Velocity of the electron starting its motion from $R_0 > a$ when it reaches the beam is given by

$$V_a = \frac{dr}{dt}(a) = \omega_e a \sqrt{2 \ln \frac{R_0}{a}}. \tag{5.54}$$

The time to reach the point a is

$$\tau_{out} = \int_{R_0}^{a} \frac{dr}{\omega_e a \sqrt{2 \ln \frac{R_0}{r}}} = \frac{R_0}{\omega_e a} \sqrt{\frac{\pi}{2}} erf \sqrt{\ln \frac{R_0}{a}}. \tag{5.55}$$

The time to reach the beam center is

$$\tau_{in} = \frac{1}{\omega_e} \arcsin \frac{1}{\sqrt{1 + 2 \ln \frac{R_0}{a}}}. \tag{5.56}$$

In the framework of our model if the electron is outside the beam, then it does not see the Coulomb collisions. One way to take this into account is to assume that the average energy gain is proportional to the time spent inside the beam relative to the total oscillation time. The heating rate as a function of the electron amplitude in this case is

$$D_h(R_0) = D_h \frac{R_0^2}{a^2} \frac{\tau_{in}}{\tau_{in} + \tau_{out}}, \tag{5.57}$$

where D_h is the heating rate calculated for the thick beam. Based on Eq. 5.57 one can write the equation for electron energy change in a unit of time

$$\frac{dE_{t,R_0}}{dt} = D_h(R_0). \tag{5.58}$$

Integrating this equation and averaging over the produced electrons one can find the average life time

$$t_{life} = \frac{2}{a^2} \int_0^a y \int_y^a \frac{m_e \omega_e^2 \psi d\psi}{D_h(\psi)} dy + \int_a^{R_p} \frac{m_e \omega_e^2 a^2 dR_0}{R_0 D_h(R_0)} = \overline{t_{in}} + \overline{t_{out}}, \tag{5.59}$$

where $\overline{t_{in}}$ is the average life time with the amplitudes $a < R_p$, $\overline{t_{out}}$ is the time to reach the wall from the beam border. Fig. 5.10 shows the behavior of the electron life time versus the electron amplitude for different beam sizes. One can see that the life time for the realistic beam size $a < 0.1a$ is at least by an order of magnitude lower than for the beam with $a = R_p$. The applicability of these approximations will be checked in Chapter 7. The effect of electron space charge can be considered using Eq. 5.52.

Based on these calculations one can find a condition under which the instability threshold χ_e is not reached

$$t_{life} \lesssim t_i. \tag{5.60}$$

Thus, one can see that there are two possible vacuum regimes in an accelerator. A good vacuum regime defined by Eq. 5.60 and a bad vacuum regime in the opposite case. One should, however, know the duration of typical cycles of the accelerator. It can happen so that the condition 5.60 is not satisfied, but the beam is extracted before the critical density is reached. The linear theory will be compared with the simulation results in Chapter 7.

5.3 Wake Fields and Synchronous Phase Shift due to Electron Cloud

The effect of the electron cloud can be observed for small electron densities below the instability threshold. The synchronous phase shift due to the electron cloud was measured in CERN [40]. These measurements proved to be a good tool to study the effectiveness of the beam pipe surface conditioning. In this section the analytical expressions developed in [70] for the energy loss in the impulse kick approximation are presented. For that journal article the electron cloud wake fields were simulated using VORPAL (Chapter 7.2). Based on the kick approximation an expression for the longitudinal wake field was derived.

5.3.1 Energy Loss and Synchronous Phase Shift

In Section 4.1 it was shown that longitudinal impedances lead to the energy loss of the beam. This energy loss is observed via synchronous phase shift

$$\sin(\Delta\phi_s) = \frac{\Delta W_p}{ZeV_{rf}}, \tag{5.61}$$

where ΔW_p is the energy loss per particle per turn. The electron cloud also leads to the synchronous phase shift. In the LHC the observed dependence of the RF phase shift on the bunch spacing indicates that the electron clouds can be a source of the energy loss. When a bunch passes through the electron cloud, the latter shrinks rapidly towards the bunch. If the bunch is sufficiently short, most of the electrons receives only a short transverse kick. These electrons pinch in the tail of the bunch reaching there the highest density. The difference in density profile seen by the head of the bunch and its tail generates a longitudinal electric field $E_z(\vec{r})$. This field acts like a longitudinal wake field causing the energy loss:

$$\frac{dW}{ds} = -\int \rho_i(\vec{r})E_z(\vec{r})dr^3 \approx -Ze\int \lambda(z)E_z(z)dz. \tag{5.62}$$

The energy loss per particle per turn is then

$$\Delta W_p = \frac{L}{N_i}\frac{dW}{ds}. \tag{5.63}$$

Eq. 5.62 can be used to obtain the stopping powers from the fields calculated in the simulation.

5.3.2 Electron Equation of Motion

The stopping power can be obtained by the analysis of the electron energy gain in the field of the bunch. For our studies we assume a cylindrically symmetric rigid bunch moving with $\beta \approx 1$. The electron cloud interacts with it by means of the transverse electrostatic field

$$E_r^i(r,z) = \frac{q\lambda(z,t)}{2\pi\epsilon_0 r}\left[1 - e^{-\frac{r^2}{2\sigma_\perp^2}}\right], \tag{5.64}$$

where q is the beam particle charge and the line density is

$$\lambda_i(z) = \frac{N_i}{\sqrt{2\pi}\sigma_z}\exp\left(-\frac{z^2}{2\sigma_z^2}\right). \tag{5.65}$$

For further treatment the beam is assumed to have the KV transverse profile with radius $b = 2\sigma_\perp$. The equation of electron motion is then

$$r'' + \kappa^2(r,z)r = \frac{eE_r^e(r,z)}{m_e c^2}. \tag{5.66}$$

For $r < a$ and uniform beam profile, the focusing gradient is

$$\kappa(z) = \frac{\sqrt{2\lambda_i(z)r_e}}{a}. \tag{5.67}$$

5.3.3 Energy Loss of Short Bunches

First, we neglect the self space charge of electrons. Moreover, the bunch is assumed to be short compared to electron oscillation wavelength in the beam center:

$$\kappa_0 \sigma_z \lesssim 1, \tag{5.68}$$

where $\kappa_0 = \kappa(0)$. The electron cloud is set to be uniformly distributed in the pipe of the radius $a \gg b$. Under such conditions the majority of the electrons receive a transverse impulse kick [95]:

$$\Delta p_{\perp}(b) = \frac{1}{c} \int_{-\infty}^{\infty} F_{\perp}(b,s) ds, \quad F_{\perp} = -eE_{\perp}^{i}(b,s). \tag{5.69}$$

The full energy gain of the electron cloud per unit length is

$$\frac{dW_e}{ds} = \frac{n_e}{2m_e} \int_0^{R_p} 2\pi \Delta p_{\perp}^2(b) b db. \tag{5.70}$$

Taking the integral yields the stopping power:

$$S = \frac{dW_e}{ds} \approx \frac{4\pi}{\epsilon_0} Q_i^2 n_e r_e \ln\left(\frac{R_p}{a}\right). \tag{5.71}$$

Supposing that $\Delta\phi_s \ll 1$ in Eq. 5.61 one obtains the corresponding rf phase shift per unit length

$$\frac{d\Delta\phi_s}{ds} \approx \frac{4\pi Q_i n_e r_e}{\epsilon_0 V_{rf}} \ln\left(\frac{R_p}{a}\right). \tag{5.72}$$

One can easily introduce a stopping power in case of an external dipole magnetic field. The number of cyclotron oscillations per bunch length is approximately

$$N_c \approx \frac{\omega_c \sigma_z}{2\pi c}, \tag{5.73}$$

where $\omega_c = eB/m_e$ is the cyclotron frequency. If $N_c \gg 1$, then the electron horizontal motion is almost frozen leaving one degree of freedom. The stopping power is reduced by

$$\frac{1}{2\pi} \int_0^{2\pi} \sin^2 \theta d\theta = \frac{1}{2}. \tag{5.74}$$

5.3.4 Electron Cloud Space Charge

One can extend the theory to the case of a bunch traveling through the dense electron plasma channel. In this case the self space charge of the electrons is not negligible. The electron equation of motion yields

$$\delta'' + \frac{\omega_{pe}^2}{c^2}\delta = \kappa^2(b,z)b, \tag{5.75}$$

where δ is the oscillator offset and the plasma frequency is

$$\omega_{pe} = \sqrt{\frac{e^2 n_e}{m_e \epsilon_0}}. \tag{5.76}$$

A bunch passing through the plasma excites plasma oscillations. The amplitude of these oscillations is

$$\hat{\delta}(b) = \frac{b}{\kappa_e}\int_{-\infty}^{\infty} \kappa(b,s)^2 \cos(\kappa_e s) ds. \tag{5.77}$$

The energy loss in this case is related to the energy transfered into the plasma wave behind the bunch:

$$\frac{dW_e}{ds} = \frac{1}{2} m_e n_e \omega_p^2 \int_0^{R_p} 2\pi \hat{\delta}^2 b db \tag{5.78}$$

and the stopping power for $R_p \gg a$ results as

$$S = \frac{dW_e}{ds} \approx \frac{Q_i^2 \kappa_e^2}{4\pi\varepsilon_0} \ln\left(\frac{R_p}{a}\right) \exp(-\kappa_e^2 \sigma_z^2). \tag{5.79}$$

One can see that Eq. 5.79 is simply Eq. 5.71 multiplied by the exponential function. It reflects the shielding effect of the dense cloud for $\kappa_e \sigma_z > 1$. Due to this the stopping power goes to zero in the limit of infinite electron density. The comparison of the analytical stopping powers with the simulation results will be presented in Section 7.2.

5.3.5 Electron Cloud Longitudinal Wake Fields for Low Beam Intensities

Based on the kick approximation used in [70] one can evaluate the initial phase of the electron cloud wake field. If the kick approximation holds for the whole bunch, then it also holds for the bunch parts. For this reason the upper integration limit can be replaced by the finite value. Energy loss in terms of the longitudinal electric field is then

$$\frac{dW}{dz}(s) = -Ze \int_{-\infty}^{s} \lambda_i(z) E_{\|}(z) dz. \tag{5.80}$$

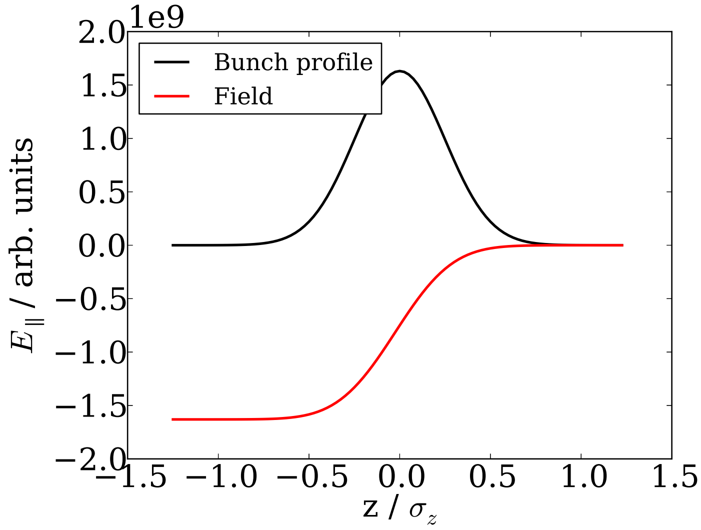

Figure 5.11.: The analytical electron cloud wake field in the kick approximation and corresponding bunch profile. The head of the bunch is to the right.

In the framework of the theory described above the transverse force of the beam can be expressed as

$$F_{\perp}(s,b) = Zeg_{\perp}(b)\lambda_i(s), \tag{5.81}$$

where $g_{\perp}$ is the form factor of the transverse force. In the kick approximation the energy loss of the bunch arriving from $-\infty$ to s is

$$\frac{dW}{dz}(s) = \frac{\pi n_e Z^2 e^2}{m_e c^2} \int_0^{R_p} \left[\int_{-\infty}^{s} g_{\perp}(b)\lambda_i(z)dz \right]^2 bdb. \tag{5.82}$$

Using Eq. 5.80 and Eq. 5.82 one obtains the equation for the longitudinal electric field:

$$\frac{\pi n_e Z^2 e^2}{m_e c^2} \int_0^{R_p} g_{\perp}(b)^2 bdb \cdot \left[\int_{-\infty}^{s} \lambda_i(z)dz \right]^2 = -Ze \int_{-\infty}^{s} \lambda_i(z) E_{\|}(z)dz. \tag{5.83}$$

The field can be obtained directly by taking the derivative with respect to longitudinal coordinate:

$$E_{\|} = -\frac{Zen_e}{m_e c^2} \cdot \int_{-\infty}^{z} \lambda_i(s)ds \cdot \int_0^{R_p} 2\pi g_{\perp}^2(b)bdb. \tag{5.84}$$

The form of the longitudinal wake field is simply given by the line density integral. In case of Gaussian profile it is given by the cumulative distribution function (Fig. 5.11). The value of the wake field reaches a constant level and stays there infinitely long. Such behavior of the bunch wake field means that in this approximation a point charge wake field is a step function. The reason for this is that in the framework of the kick approximation each electron does not change its position. At the same time the fields in between the bunches are of less importance because they do not act on the beam. The realistic wake fields will be compared with Eq. 5.84 in Chapter 7.

6 Simulation Models

In this thesis electron cloud effects are investigated for very different conditions. The time scales of the simulated processes vary from ≈ 13 ns up to 100 ms. For this reason there are some specific features present in the simulations performed for coasting beams that are absent in the simulations of wake fields for short bunches.

The features of the 2.5D simulation codes used to study the electron cloud build-up and two-stream instability in coasting beams are described in Section 6.1. The same code is implemented to study the wake fields of the electron cloud. Section 6.2 describes the basic VORPAL settings used to simulate the electron cloud wake fields.

6.1 Beam Tracking with 2D Transverse Beam-Cloud Interaction

In many codes the interaction of beam with environment is studied separately in the transverse and longitudinal directions [58, 96, 97]. Typically in these codes the beam is sliced. The slices are kicked transversely several times per revolution. These kicks represent the environment response, namely, impedances or electron clouds. Between the kicks the beam is transfered through the lattice. One can say that such codes are 2.5D because the beam moves longitudinally. Electron cloud build-up is usually simulated independently from the instability studies. For this purpose the transverse positing of the beam is fixed. The bunch plays a role of the source of the electric field which accelerates the electrons and causes multipacting. The density obtained in such simulations is then used in another code to study the stability of the beam.

All the simulations in this thesis which do not use VORPAL follow the principles described above. For the wake field simulations the bunches are transversely fixed and the cloud is uniformly distributed. In the Coulomb heating simulations the beams are also stationary but the cloud builds up. The two-stream instability is studied together with the build-up. The verification and convergence studies are placed in Appendix A.

To study the interaction between the beam and the cloud, the electron equations of motion are discretized. The time step is chosen to resolve the maximum electron trapping frequency in the vicinity of the beam center

$$\Delta t = \frac{2\pi}{\omega_{e,max} n_{steps}}, \tag{6.1}$$

where $\omega_{e,max}$ is the trapping frequency for the peak beam line density, n_{steps} is the number of time steps in one electron oscillation period. The beam and the cloud are represented by macroparticles. Each macroparticle has the same charge to mass ratio as the original physical particle but the total macroparticle charge is bigger. This allows us to simulate the particle ensemble consisting of $10^9 - 10^{12}$ real particles using the reduced number of variables.

The following additional assumptions are made. The pipe is assumed to be round and the beam is assumed to have cylindrically symmetric distribution. The beam is sliced into the segments with length $ds = \beta c \Delta t$. The number of slices in the coasting beam is $n_{slice} \approx L/ds$. In the minority of the performed simulations each slice represents a finite number of macroparticles. The set of macroparticles is described by 6 vectors of coordinates: $\vec{x}, \vec{x}', \vec{y}, \vec{y}', \overrightarrow{dp/p_0}$ and $\vec{z}$. The number of elements in each vector is equal to the total number of beam particles. The particles are able to move longitudinally between the slices. Adding a certain momentum spread to this longitudinal motion allows us to simulate the realistic Landau damping.

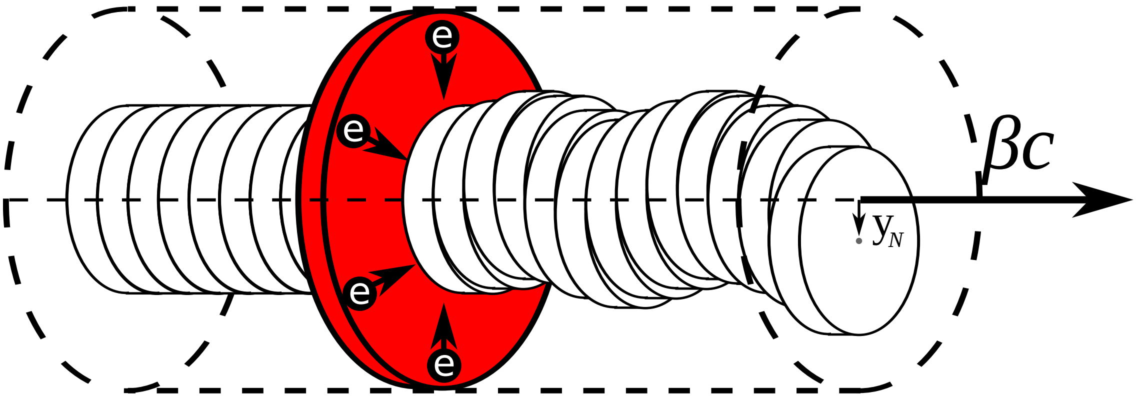

Figure 6.1.: Visualization of rigid slice beam interacting with a 2D electron cloud.

However, the physical processes that are simulated, in most cases, have a large time scale ranging to 10 ms and longer. The effect of the beam numerical noise on the error accumulation in this case is very significant. For this reason in most of the simulations the beam is assumed to be rigid. It implies that each segment is a single macroparticle with an analytically given transverse field and density distribution. Only $\vec{x}, \vec{x}', \vec{y}$ and $\vec{y}'$ representing the transverse phase space are left. The length of each vector is reduced to the number of slices. Though, no longitudinal motion of the slices relative to each other is permitted. Each slice can exhibit only the dipole motion in vertical and horizontal directions. Using such a beam reduces the noise level and the computation time. The main drawback of this model is the absence of Landau damping. In [71] the problem was solved by the introduction of a constant damping term. Each revolution period the coherent amplitude of the beam was multiplied by an analytically calculated damping coefficient. Such a model gives an instability threshold constant for all the possible excited harmonics. For the simulations in this thesis the model is modified. A separate damping coefficient is obtained for each possible excited harmonic. In case of compensated chromaticity the one-turn damping coefficient for j-th harmonic is given as

$$\gamma_{d,j} = e^{-\sqrt{\frac{2}{\pi}}\omega_j \eta \frac{dp}{p_0} T} = e^{-2\sqrt{2\pi}\eta \frac{dp}{p_0} j}. \tag{6.2}$$

Here the use of Eq. 4.27 is made. Each revolution period the Fast Fourier transform (FFT) is applied to the set of beam slice coordinates:

$$\mathscr{F}(\vec{x},\vec{x}',\vec{y},\vec{y}') = (\vec{k_x},\vec{k_x}',\vec{k_y},\vec{k_y}'). \tag{6.3}$$

The obtained set of spectra is multiplied by the vector of damping coefficients and the inverse FFT algorithm is used:

$$\mathscr{F}^{-1}(\vec{k_x}\vec{\gamma_d},\vec{k_x}'\vec{\gamma_d},\vec{k_y}\vec{\gamma_d},\vec{k_y}'\vec{\gamma_d}) = (\vec{x_d},\vec{x_d}',\vec{y_d},\vec{y_d}'). \tag{6.4}$$

This way a new, damped set of coordinates is obtained.

The electron cloud is assumed to be 2D dimensional and concentrated in one longitudinal kick point. The interaction between the beam slices and the electron cloud is purely transverse. A leap-frog scheme was utilized for electron tracking

$$\begin{cases} \vec{r}_{e,j+1} = \vec{r}_{e,j+1} + \vec{V}_{e,j}\Delta t \\ \vec{V}_{e,j+1} = \vec{V}_{e,j+1} + \vec{F}(\vec{r}_{e,j} - \vec{r}_{i,k})\Delta t + \vec{S}_e(\vec{r}_{e,j})\Delta t + \sqrt{D_h(\vec{r}_{e,j} - \vec{r}_{i,k})/m_e\Delta t}\vec{G}_n \end{cases}, \tag{6.5}$$

where j is the timestep number, $\vec{V}_{e,j}$ and $\vec{r}_{e,j}$ are the electron's velocity and coordinate vector from the previous time step, $\vec{r}_{i,k}$ is the vector of beam slice center of mass, $k = j \pmod{n_{slice}}$ is the number of the interacting slice, $\vec{F}(\vec{r}_{e,j} - \vec{r}_{i,k})$ is the analytical beam force depending on the chosen beam profile, $\vec{S}_e(\vec{r}_{e,j})$ is the electron space charge force calculated at the j time step, $\vec{G}_n$ is the noise term given by the random number with normal distribution and unit standard deviation. $D_h(\vec{r}_{e,j} - \vec{r}_{i,k})$ is given by Eq. 5.34 substituting a local beam density. In the Coulomb heating simulation the radial density of the cloud was stored, and the space charge term was obtained solving a radial Poisson equation. In the simulations of the electron cloud wake fields routines from PATRIC [96] were used to interpolate the macroparticles on the rectangular grid. The Poisson equation was also solved using the libraries from this code. Typically the rectangular 256 × 256 grid was used for the density interpolation and electric field computation.

Together with the electron tracking, the slice receives a momentum kick

$$\Delta\vec{x}'_{i,k} = \sum_{n=1}^{N_{el}} \frac{\vec{F}(\vec{r}_{i,k} - \vec{r}_{e,j,n})T}{Am_0\gamma\beta c}, \tag{6.6}$$

where N_{el} is the total number of electron macroparticles, n is the number of the electron, T is the revolution period. Each slice passes through the electron cloud kick point and then is transferred through the lattice by means of one-turn transfer matrix. The form of λ_i perturbed by the barrier bucket in general should be calculated self-consistently using the Vlasov's equation [98]. This is beyond the scope of our studies. For the simulations of the electron trapping in the beam with a gap we have assumed simplified beam parameters. The line density as a function of time is shown schematically in Fig. 6.3. The tails, i.e., transition from the lowest density to the

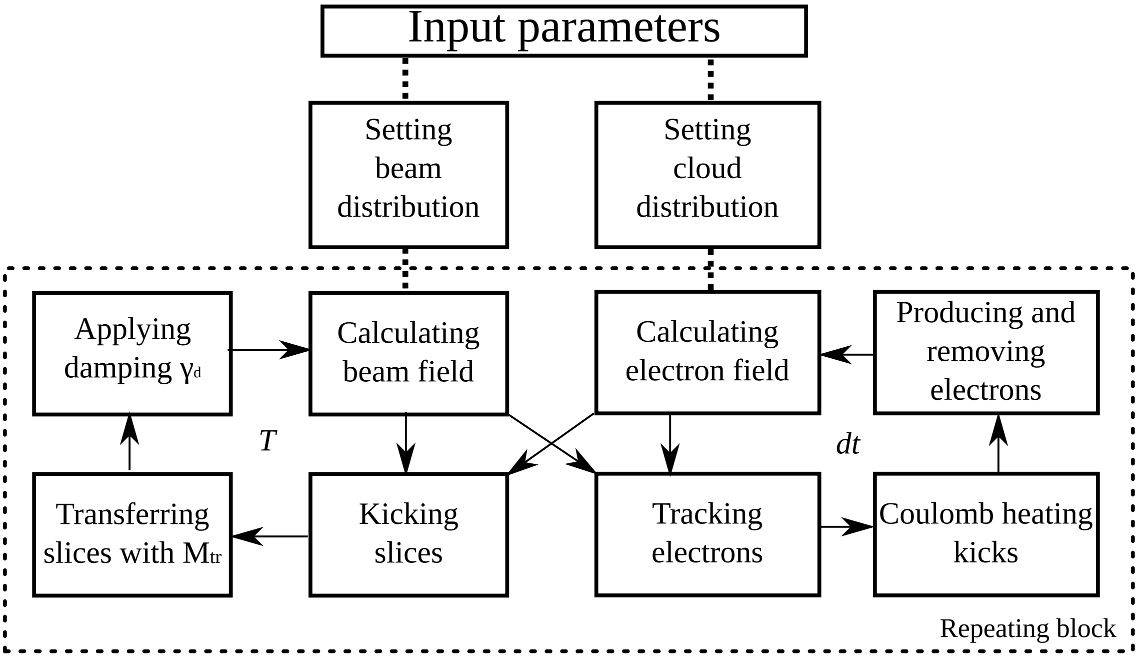

Figure 6.2.: Basic simulation scheme. Each beam slice interacts with the electron cloud only once per period. Electron cloud slice is modified each timestep. The fields are solved either on the grid or analytically.

highest one are represented by the cosines. Everywhere else the line density is constant. To sum up, there are four form parameters: $L_g = L_{tail} + L_l$ - the total length of a gap, L_{tail} - the total length of the tail part described by the cosine functions, L_l - the length of the leakage plateau, $\mathscr{S} = \lambda_{i,min}/\lambda_{i,max}$ is the ratio of the minimum line density to the maximum line density. With this representation one can study completely nonadiabatic cases, e.g., sharp rectangular gap, and adiabatic ones when tails are long compared to the electron oscillation period.

The transverse distribution of the beam in all the wake field simulations was KV. The simulations of the transverse wake fields were performed using the rigid beams made of macroparticles with equal weights. Their longitudinal distribution was Gaussian. The bunch was passing through the cloud slice by slice, and the field imposed on the bunch particles was averaged over

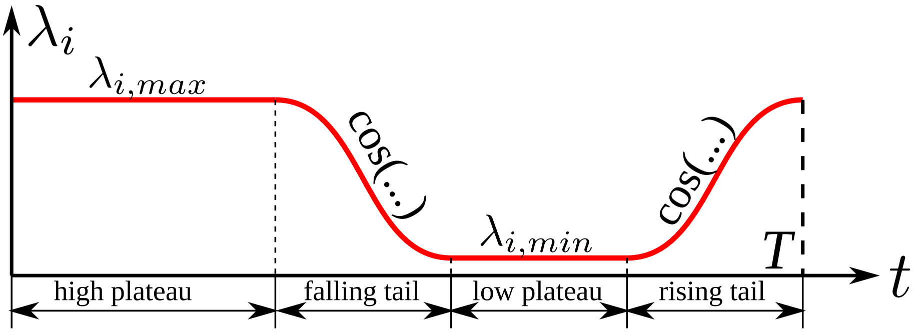

Figure 6.3.: Line density as a function of time used in the simulations of electron trapping in long bunches.

the slice and saved as a wake field. To resolve the field at the tails of the bunch the total number of the bunch macroparticles was 32 million. In case of high electron densities a stationary positive background was added. It was holding the electrons on their places until the bunch arrived. In simulations of the longitudinal wake fields the 2D density of the electron cloud was saved each time step, forming a 3D density array. After the simulation run the r-z Poisson solver was applied to obtain the field.

All the output is saved into the ASCII files. The following electron cloud data can be saved during and after the simulations: electron average density, electron cloud r.m.s. size and oscillation center-of-mass amplitude, electron cloud energy distribution, electron cloud transverse density profile and electric field.

6.2 VORPAL

To simulate the transverse and longitudinal electron cloud wake fields in 3D the commercial package VORPAL 5.0 [99, 100] was utilized. The only possible mesh geometry is rectangular. For all the simulations the round pipe was positioned in the middle of the rectangular domain. The dimensions of the domain in x and y were $2.2 \cdot R_p$. For the LHC conditions the pipe segment of 4 m long was simulated. In case of longer SPS bunches the length was 7 m. In all the simulations the length of the grid cell in longitudinal direction was $\Delta z = 10$ mm. In transverse direction the grid cell length was $\Delta x = \Delta y = 0.55$ mm. The electron cloud was uniformly distributed yielding 20 macroelectrons per grid cell. The time step for all the simulations was calculated as follows:

$$\Delta t = \frac{0.7}{c\sqrt{\frac{1}{\Delta x^2} + \frac{1}{\Delta y^2} + \frac{1}{\Delta z^2}}}. \tag{6.7}$$

This prevents the electromagnetic wave to traverse more than one grid cell per time step.

A beam was represented by the current density $\vec{J} = (0, 0, J_z(x, y, z))$ with longitudinal component given as follows:

$$J_z = J_0 exp\left(-\frac{(z-ct)^2}{2\sigma_z^2}\right) H\left(a^2 - x^2 - (y - \Delta_y - (z-ct)\tan(\theta))^2\right), \tag{6.8}$$

where $J_{0,z}$ is the peak current density, $H(...)$ is the Heaviside function, a is the bunch radius, Δ_y is the bunch offset and θ is the tilt angle. Each time step the current density is reassigned to the grid cells.

The fields are obtained solving the Maxwell equations for the given current density. The VORPAL manual proposes several field updaters suitable for different tasks. These field updaters being applied every time step construct the field solver. Yee-Ampere updater was applied to update the electric field $\vec{E}$ components using the magnetic field $\vec{B}$ and the current density. Yee-Faraday updater was utilized to update the magnetic field using the electric field. A special

Table 6.1.: Computational domain parameters in VORPAL simulations.

Parameter	in SPS	in LHC
Segment length	7 m	4 m
Transverse cell length, $\Delta x = \Delta y$	1.1 mm	0.55 mm
Longitudinal cell length, Δz	10 mm	10 mm
Number of macroelectrons per cell	20	20
Dimensions, $N_x \times N_y \times N_z$	$80 \times 80 \times 700$	$80 \times 80 \times 400$

Yee-Faraday updater was applied for Dey-Mittra cut cells representing the curved surface of the beam pipe. Beam and electron fields were solved separately.

For low electron densities Dirichlet boundary condition was applied. To avoid electron run-away for the dense electron clouds the Neumann boundary condition was used. In simulations this lead to the behavior similar to the case with the stationary positive background in 2D electrostatic simulations.

7 Simulation Results

This chapter is divided into two parts. In Section 7.1 the simulation results of the electron cloud build-up and instability for the FAIR conditions are presented. Additionaly, some limited simulations were performed to study the electron cloud survival in the coasting beam perturbed by a barrier bucket. Section 7.2 shows the comparative results of wake field simulations using different simulation codes. The kick approximation wake fields are compared with the simulated ones as well.

7.1 Coasting Beams in SIS-100

7.1.1 Build-up in Stationary Uniform Beam

In Section 5.2.3 the effect of Coulomb collisions on electron density was explicated. The theory predicts a decrease of electron density with the beam size. According to the rough estimations the neutralization of the coasting beam in the SIS-100 for 10^{-12} mbar is 0.5% (Fig. 5.9). In this section we simulate the build-up of the electron cloud in a stable coasting beam for realistic beam parameters. We start with the case of small production rates i.e., negligible electron space charge. Under these conditions the saturated density is proportional to the ionization rate i.e., pressure. For this reason in this subsection we study the relative change of the electron density depending on the beam size. The simulations with the realistic SIS-100 beams are performed in Subsection 7.1.2.

Fig. 7.1 shows the build-up of the electron cloud limited by the Coulomb collisions in the absence of space charge. Four curves are shown. Two of them are obtained for the realistic 2D motion when electrons are randomly kicked in x and y directions. The other two correspond to the case of the pure radial motion with only radial random kicks. In both cases a uniform beam distribution is assumed. The electron average density is normalized to the density predicted by the analytical theory for thick uniform beam with $a = R_p$. As expected, the density of the electron cloud with the full degrees of freedom is larger than in the case of the strict radial motion. In the latter case it agrees well with the analytical prediction for the thick beam. For $a/R_p = 0.1$ one sees approximately the same absolute value of discrepancy between the two models but a very significant disagreement with the analytical prediction. This indicates that the electron life time is much larger than predicted by Eq. 5.59.

Indeed, the scan over beam radius for fixed production rate ν_i and intensity (Fig. 7.2) reveals an interesting behavior. The colored curves show the simulation results, the black ones represent the analytical results. Life time is simply given by the total number of electrons divided by the

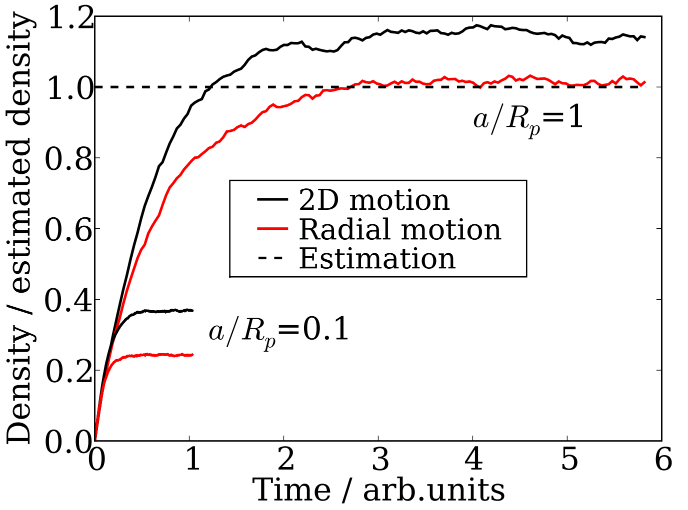

Figure 7.1.: Example of the build-up in KV coasting beams for two beam radiuses: $a/R_p = 1$ and $a/R_p = 0.1$. Compared are the models with pure radial motion and realistic 2D electron motion. Saturation happens because of the Coulomb collisions. Density is normalized to the value predicted for thick uniform beam (Fig. 5.9).

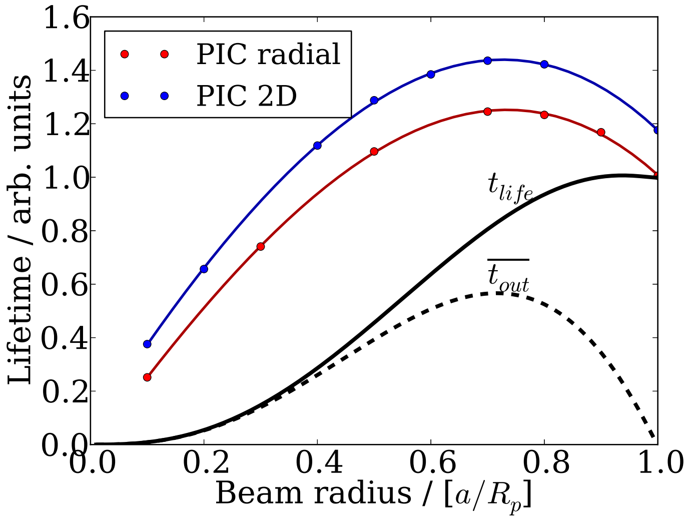

Figure 7.2.: Comparison of the analytical electron life times (the number of electrons divided by the production rate) with the simulated ones. The values are normalized to the analytically predicted life time for the thick beam. The cases of pure (red) radial and unrestricted (blue) motion are depicted. The black curve shows the analytically obtained life time. The dashed black line corresponds to the average time needed for electron to get from beam border to the pipe in the analytical theory.

total production rate. One can see that the agreement between the analytical model and the simulations is reached only for the maximum beam radius. The life time (i.e., density) is a nonmonotonous function of the beam radius. The maximum density is observed at $a = 0.7R_p$. The $\overline{t}_{out}$ curve shows the maximum exactly at this position. For small beam sizes the density goes down in both cases. However, in analytical estimations this happens much faster. The main weak point of the analytical estimations is very likely due to the assumption of the heat transfer proportional to the time spent inside the beam by the freely oscillating electron.

7.1.2 Build-up in Stable Gaussian Beam

So far only the uniform beam distribution has been assumed. Now we proceed with the simulations of the electron cloud build-up in stable Gaussian beam. The cloud space charge is also included. For the simulations the realistic SIS-100 beam parameters are assumed. The beam pipe is assumed to be round with radius $R_p = 5$ cm. Fig. 7.3 shows the evolution of the cloud density for the U^{28+} beam at energy 1 GeV/u. For these simulations the beam transverse r.m.s. radius was set to $\sigma_\perp = 7.5$ mm. The equivalent KV radius is 1.5 cm, so that $a/R_p = 0.3$. For this radius the electron cloud density should be almost the same as for the thick beam (Fig. 7.2). This is indeed so. The red curve corresponds to the pressure $2 \cdot 10^{-11}$ mbar and gives 10% saturated neutralization degree. At the same time Fig. 5.9 indicates that for 10^{-11} mbar the neutralization should be 5%, which is exactly twice smaller. One can see that the dependence becomes nonlinear with the increasing production rate when the neutralization

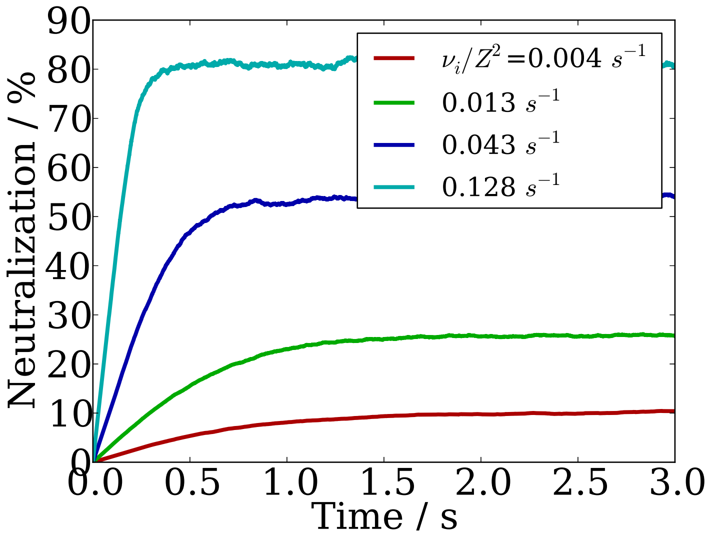

Figure 7.3.: Neutralization degree reached for different production rates (pressures) taking into account electron space charge and heating rate. The profile of the U^{28+} beam is Gaussian with $\sigma_r = 7.5mm$ and $E = 1GeV/u$. Normalized ionization rate $\nu_i/Z^2 = 4 \cdot 10^{-3}\ s^{-1}$ corresponds to approximately $2 \cdot 10^{-11}$ mbar.

degree approaches 100%. There is a transition from the heating dominated regime to the space charge dominated regime.

The extraction energy of the SIS-100 will go up to 2.7 GeV/u for heavy ions. For this reason the scan over beam energies was performed. The resulting dependence of the saturated electron density on the production rate is presented in Fig. 7.4. The difference in neutralization degrees for the simulated energies is not very large. The reason for this is that there are two competing processes. The acceleration of the beam is accompanied by the reduction of the energy transfer from single ions (Eq. 5.33). At the same time the beam is shrunk leading to the increase of the local collision rate. The results of the simulations mean that for the chosen parameter range these processes balance each other. The data obtained in numerical simulations is fitted with the analytical Eq. 5.52. These curves proved to be identical for all possible Z if the beam emittance and energy are preserved. This signifies that the equality of the neutralization factors predicted by the analytical theory for thick beams is valid for the beams with realistic shapes.

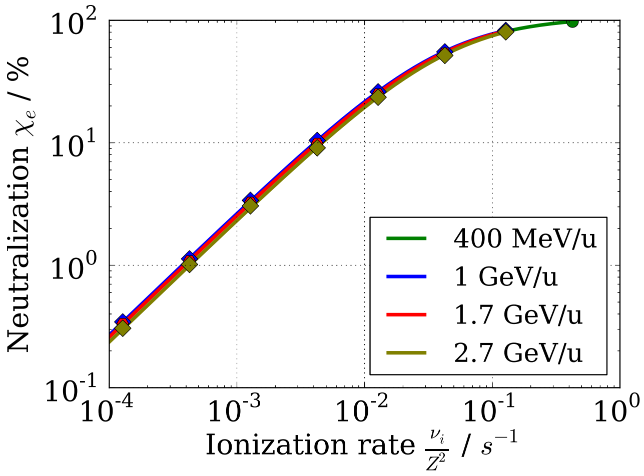

Table 7.1.: Simulation parameters for SIS-100 beams.

Energy / MeV/u	$\sigma_\perp$ / mm
400	10
1000	7.5
1700	6.2
2700	5.2

Figure 7.4.: The neutralization degree reached in stationary beams including heating rate. Pipe radius is R_p =5 cm. Beam size is changing from 10 mm at 400 MeV/u to 5.2 mm at 2700 MeV/u according to Eq. 3.32.

To sum up, it is found out that the cloud density almost does not depend on the beam energy in the studied parameter range. Under the FAIR conditions densities obtained using simple formula 5.42 give a good estimation. For the SIS-100 design pressure the neutralization of the beam is approximately 0.5%. To clarify, whether such densities are dangerous for the SIS-100 operation, the simulations of the two-stream instability were performed. The results are presented in the next subsections.

7.1.3 Electron Frequency Distribution

The electron-ion two-stream instability threshold strongly depends on the frequency spreads of the interacting beam and electron cloud (Eq. 5.28). If electrons are born due to the residual gas ionization in the field of a Gaussian beam, then ≈60% of them are produced outside the r.m.s. beam radius $\sigma_\perp$ (Fig. 5.7). The spectrum of ionization electrons in the field of the beam is shown in Fig. 7.5. To obtain this figure the electrons were produced proportionally to the local beam density. The offset of the cloud center of mass was recorded and the Fourier transform was implemented. The r.m.s. spread of the frequency distribution is 25%. The center of the distribution is shifted to lower frequency $\approx 0.7 \cdot \omega_e$. The relative spread $\Delta Q_e/Q_e$ does not depend on the intensity of the beam. This happens because all the nonlinear field components scale proportionally to the total beam intensity. The same holds for the increased beam radius.

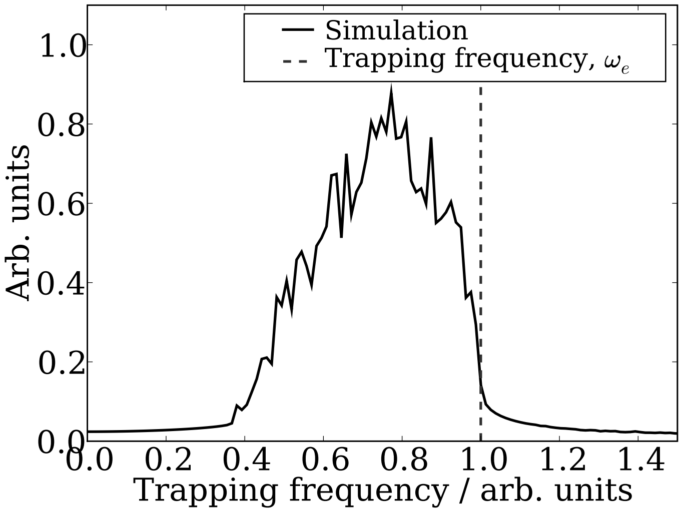

Figure 7.5.: Oscillation spectrum of trapped electrons produced by the residual gas ionization in the round Gaussian coasting beam. The frequency axis is scaled to the trapping frequency in the vicinity of the beam.

After the electron frequency spread has been calculated one can estimate the threshold neutralization degree using Eq. 5.30. The threshold as a function of beam intensity for the maximum and minimum energies from Table 7.1 is shown in Fig. 7.6. One sees that the threshold density decreases with energy and intensity. For the given parameters the threshold density is bigger than the one given by Coulomb heating at 10^{-12} mbar only for the lowest intensities and the highest momentum spread.

7.1.4 Two-Stream Instability

In this section the results of the two-stream instability simulations are presented. The threshold densities are obtained neglecting the Coulomb heating. After that they are compared with the results of Section 7.1.2. The instability thresholds were studied dynamically. It means that the electron cloud density at the beginning of the simulations was set to zero. Hereafter, the electrons were constantly produced. At some point the oscillation amplitude of the beam and the electron cloud size exploded. The electron density accumulated till this moment gives the threshold $\chi_{e,0}$. Because the simulations were performed without the electron space charge,

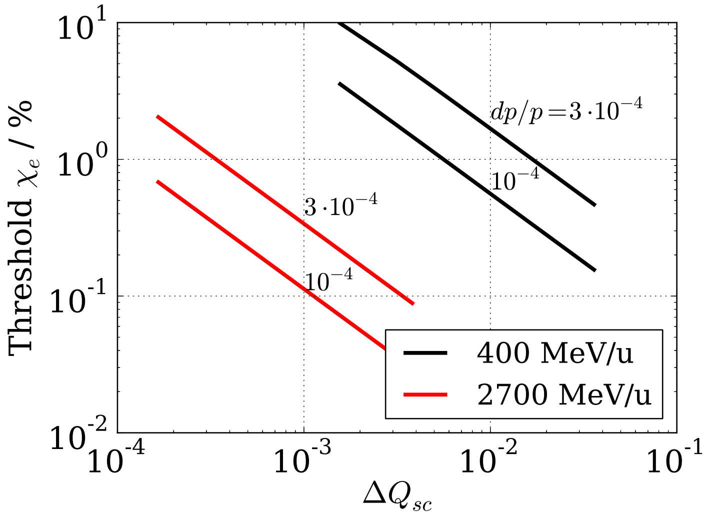

Figure 7.6.: Analytical instability threshold as a function of beam intensity (space charge tune shift) for the realistic electron frequency spread. U^{28+} beam intensity varies from $5 \cdot 10^{10}$ to $1.2 \cdot 10^{12}$.

Eq. 5.31 was applied to correct the instability threshold. The width of the electron frequency distribution obtained in the previous subsection was used.

The reference ion used for many SIS-100 studies is U^{28+} [12, 101, 102]. The design intensity for this ion is $N_i = 5 \cdot 10^{11}$ according to [12]. More recent sources [103, 104, 105] indicate $N_i = 4 \cdot 10^{11}$. For simulations in this thesis three species were selected: U^{73+}, Au^{25+} and Ar^{18+}. Based on the U^{28+} parameters, their intensities were calculated using Eq. 5.26. To speed up the simulations, the artificially high production rates were chosen leading to an instability in 5-8 ms. Simultaneously, the production rate was set to be proportional to the ion charge state Z. This means that the beams of different species are neutralized equally in a unit of time. The use of the three ions and the production rate scaling with Z has the following advantage. It allows to check that the beams with equal space charge tune shifts have similar instability thresholds.

Fig. 7.7 shows the beam amplitude and the corresponding cloud size as a function of time for the three species. The simulation parameters for the figure are listed in Table 7.2. The chosen production rate neutralizes the beams equally in a time unit. One sees that the instability threshold does not depend on the type of the beam particle if the intensity is scaled according to Eq. 5.26. At the same time some ions gain bigger oscillation amplitudes compared to others. We also observe that the cloud size stays constant until the linear instability threshold is reached. One can see that the growing phase of the instability stops relatively fast. For higher momentum spread one can see that the oscillation amplitude even falls down at some point and starts to grow anew. This process shows some similarities with the ISR observations [10], where the modulated signal of the instability was detected. For the Ar^{18+} beam at 400 MeV/u the instability threshold was studied as a function of the production rate. The production rate was varying by two orders. The lowest production rate was approaching the values corresponding to

Table 7.2.: Two-stream instability simulation parameters for Fig. 7.7.

Parameter	Value			
Ion type	U^{73+}, Au^{25+}, Ar^{18+}			
Normalized intensity, $N_i Z^2/A$	$13.4 \cdot 10^{11}$			
Circumference, L / m	1083			
Momentum spread, dp/p	10^{-4} and $3 \cdot 10^{-4}$			
Transition energy, γ_t	24.5			
Vertical tune, Q_y	17.29			
Electron frequency spread, $\Delta Q_e/Q_e$	0.25			
Energy, MeV/u	400	1000	1700	2700
Production rate, ν_i/Z / $[s^{-1}]$	136	34	68	68

10^{-10} mbar. The results of these simulations are presented in Fig. 7.9. The points correspond to the time when the cloud size explodes. One can see that in the simulated range the difference between the thresholds at the maximum and minimum production rates is only 10%. The instability threshold as a function of beam energy for the parameters of Fig. 7.7 is shown in Fig. 7.8. One sees that the thresholds are larger for the larger momentum spread. However, the dependence is nonlinear, contrary to the analytical theory. It is important to point out that for the given simulation parameters the instability threshold is higher than the density limited by the Coulomb heating at 10^{-11} mbar.

For the maximum and minimum energies in Table 7.1 the scan over beam intensities was performed. The momentum spread was set to $dp/p = 10^{-4}$. Fig. 7.10 shows the threshold χ_e as a function of beam intensity. Simulations show that the threshold density is inversely proportional to the beam intensity. For this figure the maximum beam intensity in terms of space charge tune shift was chosen to be 3 times higher than for the reference ion U^{28+}. This corresponds to the $1.2 \cdot 10^{12}$ intensity of Au^{25+} given in [12]. In this extreme case the threshold density is again larger than the level given by the Coulomb heating at 10^{-12} mbar. However, if the dynamic pressure would go up to 10^{-11}, the threshold can be reached.

One should keep in mind that these simulations were performed for the artificially increased production rates. The approximate pressure corresponding to $\nu_i/Z = 136\text{s}^{-1}$ for U^{73+} at 400 MeV/u is $5 \cdot 10^{-9}$ mbar. For U^{28+} it is $\approx 10^{-8}$ mbar. These pressures would prohibit any safe operation due to charge exchange losses and dynamic vacuum reasons [13]. Even without Coulomb heating, in case of design pressure 10^{-12} mbar the time to reach 10% neutralization for U^{73+} is close to 4 seconds and is growing inversely proportional to Z. Another important point is the chromaticity present in the real machine. The SIS-100 will have only the partially compensated chromaticity [12]. This would increase the damping compared to the cases studied in this subsection.

In this subsection we have seen that the model used for the simulations reproduces the scalings of the linear theory. Neutralization degree thresholds decrease with growing beam intensity.

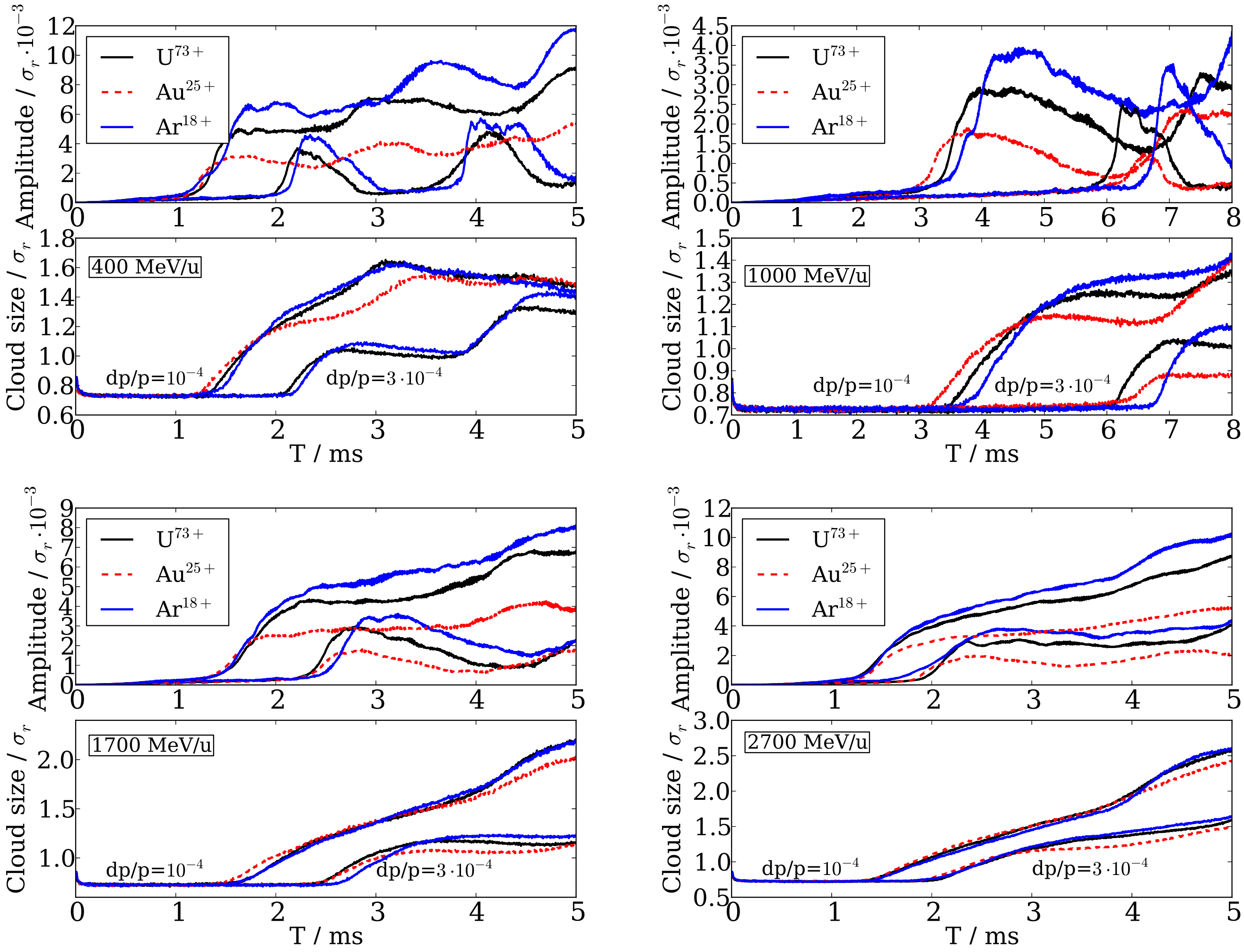

Figure 7.7.: The evolution of the beam oscillation amplitude and transverse cloud size in U^{73+}, Ar^{18+} and Au^{25+} coasting beams. Figure order is from left to right, from up to down. The upper left figure corresponds to 400 MeV/u. Corresponding intensities are $6 \cdot 10^{10}$, $1.658 \cdot 10^{11}$ and $4.234 \cdot 10^{11}$. The average electron cloud density is linearly growing. When the instability threshold is reached, the cloud size starts to grow.

Beams consisting of different species have similar instability thresholds if the beam energies, emittances, and space charge tune shifts are similar. Momentum spread, as expected, raises the threshold neutralization degree. However, one can see that the difference between the linear theory and the simulations is very big. As it is shown in Appendix A in linear cases the agreement between the simulation model and analytical theory is very good. One possible reason for the discrepancy in realistic simulations is that the electrons are not simply an ensemble of oscillators with frequency spread. Their frequency spread comes from the highly nonlinear field.

Taking into account the results of Subsection 7.1.2 one can conclude that for any possible beam intensity one can find a residual gas pressure that will prevent the beam from the electron cloud instability on any time interval. The SIS-100 design pressure of 10^{-12} mbar seems to be

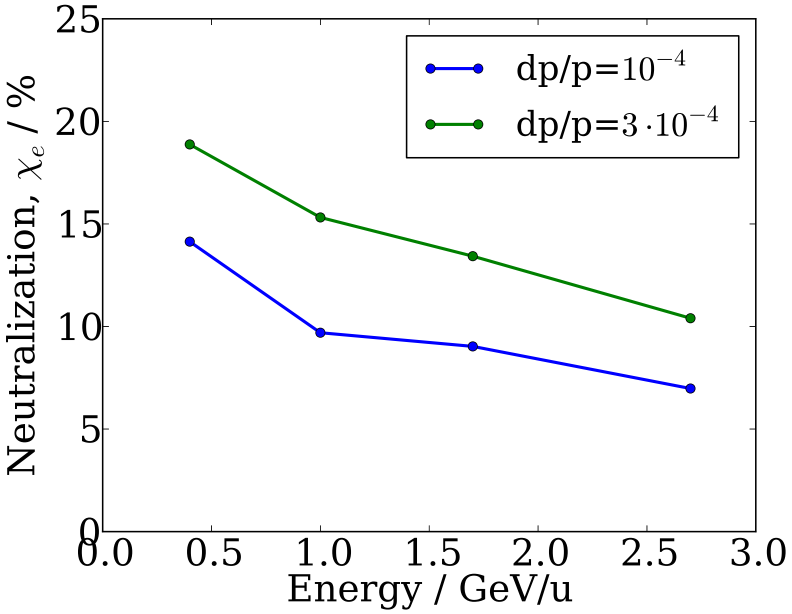

Figure 7.8.: Averaged over three species threshold neutralization degree as a function of beam energy. The points are obtained multiplying the time at which the cloud size starts to increase by the corresponding normalized production rate. All the neutralization factors are higher than the saturation due to Coulomb heating at 10^{-12} mbar.

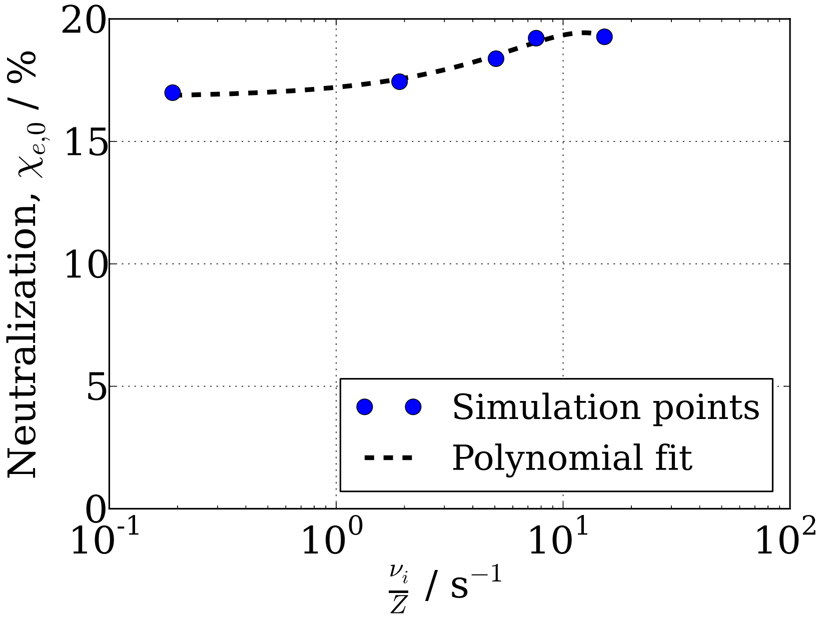

Figure 7.9.: Instability threshold as a function of production rate for Ar^{18+}. Beam energy is 400 MeV/u, momentum spread is 10^{-4}, intensity is $1.2\cdot10^{11}$. Symbols show the simulation results. The relative difference between the thresholds at maximum and minimum production rates is 12%.

sufficient to preserve the beam stability for the compensated chromaticity and $dp/p \approx 10^{-4}$ even for the maximum intensity given in [12].

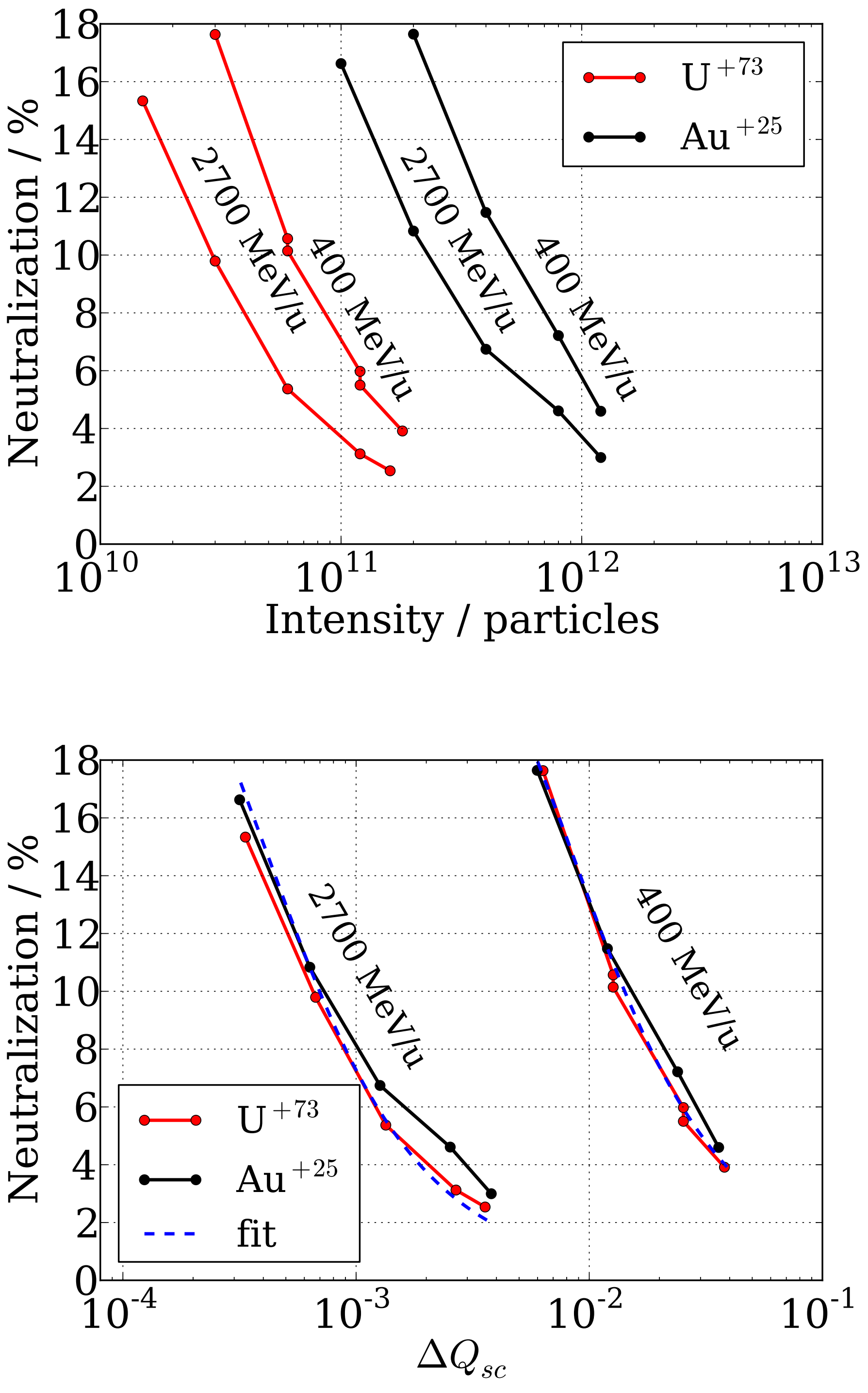

Figure 7.10.: Instability thresholds as a function of beam intensity for $dp/p = 10^{-4}$. The upper graph shows the dependence on the number of particles. The lower graph shows the dependence of the threshold on the corresponding space charge tune shift. The threshold electron density is determined by the time at which the cloud size starts to grow multiplied by the ionization rate.

7.1.5 Barrier Bucket Effect

The linear theory (Sec. 5.2.1) manifests itself very clearly at low beam intensities. Fig. 7.11 shows the build-up of the electron cloud from residual gas ionization in the beam with a rectangular gap. The curve that gives the average linear growth corresponds to the case when the condition Eq. 5.12 is satisfied. Another curve is obtained for the gap length when the stability condition is not satisfied. The ratio between the slopes in perturbed and unperturbed cases gives the survival ratio δ_{e,z_0}. To check the results of Eq. 5.18, the simulations for completely nonadiabatic case were performed, i.e., at some point $\lambda_i = 0$. Transverse beam profile was round and uniform. The length of the gap ranged from 0 to 20% of the accelerator circumference. Two gap profiles were investigated: a completely rectangular with 0% leak and a purely cosine without plateau in the minimum. The results are seen in Fig. 7.12. One can notice that there is a perfect agreement with the analytically predicted survival ratio. Beam boundary acts like a real physical border where electrons are lost.

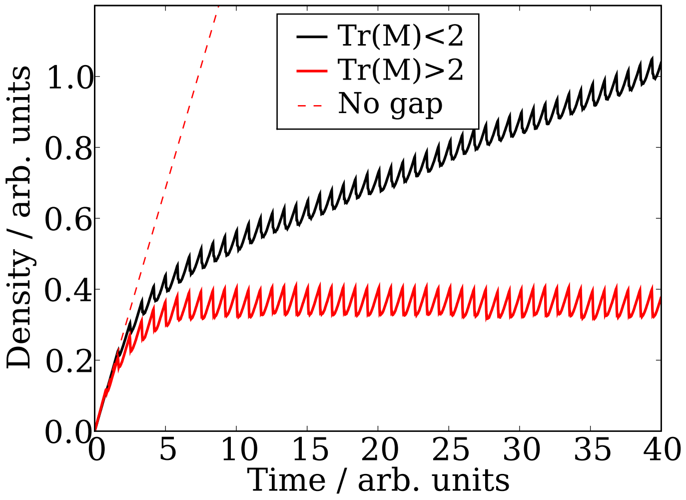

Figure 7.11.: Example of the gap effect on the electron density in PIC simulations of KV beam. The dashed line shows the electron accumulation without a gap. The black curve shows the long term accumulation. The red line shows the absence of accumulation (density stays at negligible level).

However, the picture changes dramatically if the beam form-factor is modified. The simulations were performed for elliptical KV beams and for Gaussian beams. In both cases the beam intensities were the same as for the round KV beam simulations. The beam parameters were chosen so that ω_e in the vicinity of the beam center was equal in KV and Gaussian beam. This signifies that $r_{kv} = \sqrt{2}\sigma_\perp$ meaning lower KV beam emittance. The trapping ability of the beam was lost. All the electrons after 10-100 turns gain significant amplitudes and reach the wall. However, it was observed that in between the stability islands (Fig. 7.12) electrons in Gaussian beam are lost slower. When the linear theory predicts the stability of the cloud, Gaussian beam

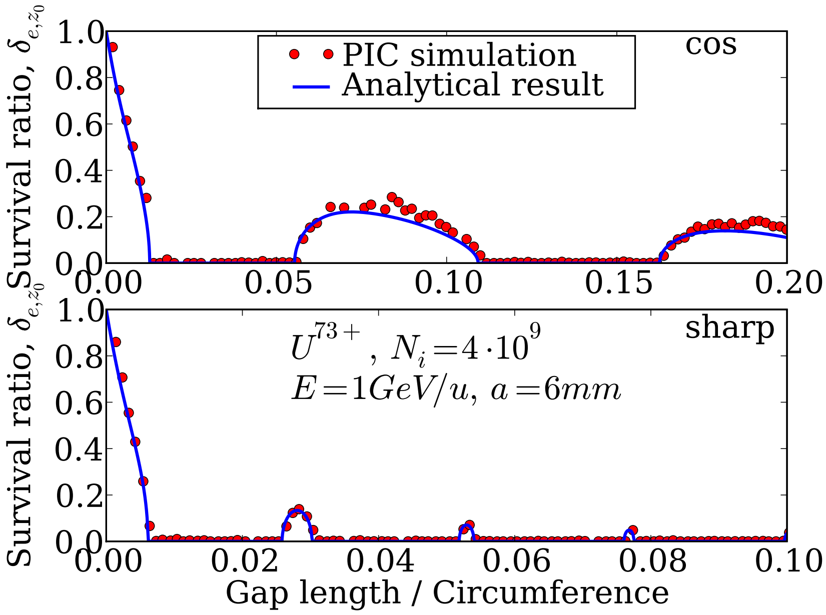

Figure 7.12.: The electron survival ratio as a function of gap length in the SIS-100 for the low density round KV beam. Gaps with two form factors are compared. The simulation parameters are $L_l = 0$, $L_g = 0.1L$ and $\mathscr{S} = 0$. Beam with cosine tails shows wider stability region.

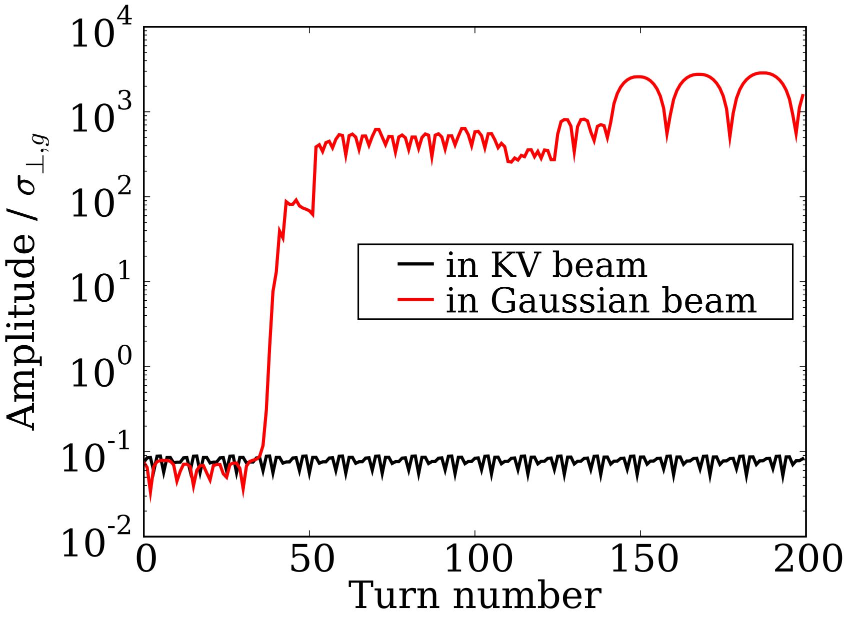

Figure 7.13.: Evolution of the electron amplitude for Fig. 7.12 conditions. Rectangular gap length is $L_g = 0.029L$. The black curve shows the finite amplitude in case of KV beam. The red curve shows the unstable behavior of the electron in Gaussian beam.

shows the trapping only for very small amplitudes $r < 0.1$. However, the total contribution of these electrons to the accumulation is negligible (Fig. 5.7).

So far the nonadiabatic low-intensity case has been addressed. What happens if the design intensities of FAIR are considered? For the reference ion U^{28+} at intensity $5 \cdot 10^{11}$, the total stored charge is ≈50 times larger than it was assumed for Fig. 7.12. The electron trapping frequency in this case is 7 times larger. It means that the distribution of stable islands is also 7 times more dense. Again only round KV beam gives a long term accumulation in stability islands. And this happens up to $\mathscr{S} = 0.01$. Above 1% leakage the cleaning is already not so efficient. At 10% the motion of electrons under the FAIR conditions is almost adiabatic. The islands of stability merge together. Electrons having high nonlinear amplitudes still stay trapped for hundreds of turns. Additional simulations are needed to find out the saturated electron cloud density.

To summarize, in this subsection the motion of an electron in the long sausage-like bunches was studied. It was shown that the linear theory described, for example, in [45] does not work for the realistic Gaussian distribution under the FAIR conditions. The simulations indicate that the trapping may be effective when the beam density perturbation gets more adiabatic if, for example, the leakage in the gap is significant (>1%).

7.2 Electron Cloud Wake Fields for Relativistic Proton Bunches

In this section the results of the wake field simulations are presented. The simulations were performed for the CERN LHC and SPS conditions. The main simulation parameters are listed in Table 7.3. The wall in all the simulations was absorbing the electrons. The electron production during the bunch passage is not taken into account.

Table 7.3.: Wake fields' simulation parameters

Parameter	LHC	SPS
Particle	proton	proton
Intensity	10^{11}	$1.1 \cdot 10^{11}$
KV beam radius / mm	2	4
Bunch r.m.s. length / m σ_z	0.1	0.25
Pipe radius	2 cm	4 cm
Cloud density	$10^{12} - 10^{16}\ m^{-3}$	$10^{12} - 10^{16}\ m^{-3}$

In Subsection 7.2.1 the longitudinal electron cloud wake fields are simulated. The results of the electrostatic and electromagnetic codes are compared with the analytical wake field in the kick approximation. In Subsection 7.2.2 the results of the transverse wake fields for the disturbed relativistic bunches are presented.

7.2.1 Longitudinal Wake Fields

Fig. 7.14 shows the longitudinal wake field calculated using the electrostatic code with 2D Poisson solver and VORPAL. A perfect agreement between these two simulation codes is observed. Another wake field obtained for similar bunch parameters but high electron density is depicted in Fig. 7.15. One can see that the bunch produces long lasting plasma waves. Both codes in this case also agree very well.

By virtue of the very good agreement between the simplified PIC code and VORPAL, simulations of the electron cloud stopping powers were performed in [70]. The stopping power curve as a function of electron density is shown in Fig. 7.16. One can see that the agreement between the simulations and theory for very low densities is good. In simulations, however, the decrease of the stopping power starts later than predicted by the theory. If one substitutes the twice shorter bunch length to Eq. 5.79, then the analytical curve agrees well with the simulation results. The reason for this discrepancy is not understood yet. Even in the region where the agreement is good the numerical points lie below the analytical curve. One can understand this, comparing the longitudinal wake fields obtained analytically and in simulations. These wake fields are shown for $n_e = 10^{12}\mathrm{m}^{-3}$ in Fig. 7.17. One can see a dramatic difference between the wake fields at the tail of the bunch. However, the contribution of this discrepancy to the stopping power is not that significant. To show that there are conditions under which the kick approximation gives a good agreement with the VORPAL simulations, the wake field was simulated for the bunch intensity 10^9 protons (Fig. 7.18). The corresponding stopping powers as well as the wake field form agree much better under these conditions.

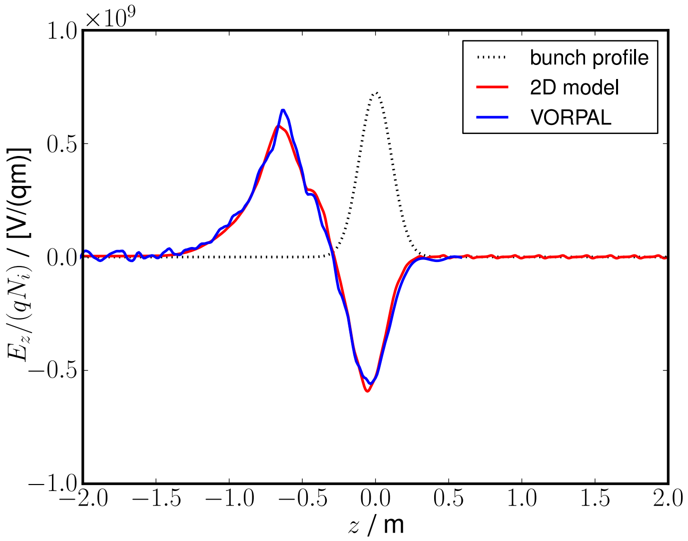

Figure 7.14.: Longitudinal electric field induced by the electron cloud interacting with the short proton bunch (LHC). Electron cloud density is 10^{12} m^{-3}.

7.2.2 Transverse Wake Fields

Additionally, for the low electron cloud densities ($\sigma_z \kappa_e < 1$) the simulations of the transverse wake fields were performed. The beam was moving along the pipe axis but with an offset or tilt. This corresponds to $k = 0$ and $k = 1$ head-tail modes [45]. Fig. 7.19 shows the position of the bunch and the electron cloud pinch observed in the VORPAL simulations. One can clearly see the transverse asymmetry of the cloud that generates the transverse field acting on the bunch. The comparison of the VORPAL and 2D electrostatic PIC code wake fields for $k = 0$ mode is shown in Fig. 7.20. The agreement is very good. The same simulations were performed for the $k = 1$ mode. In this case the agreement is again very good. The noisy behavior of the 2D wakes at the ends of the intervals is due to the diminishing number of beam macroparticles.

The results of this section indicate that for highly relativistic cases like in the LHC and the SPS, the codes with pure 2D interaction between the electron cloud and the beam are sufficient. The formula describing the initial growing phase of the longitudinal electron cloud wake field is derived. It is found out that for the LHC and SPS conditions the discrepancy between Eq. 5.84 and numerical simulations is significant at the bunch tail. However, the stopping powers obtained in the framework of the kick approximation (Eq. 5.71) and their simulated analogue are in a good agreement.

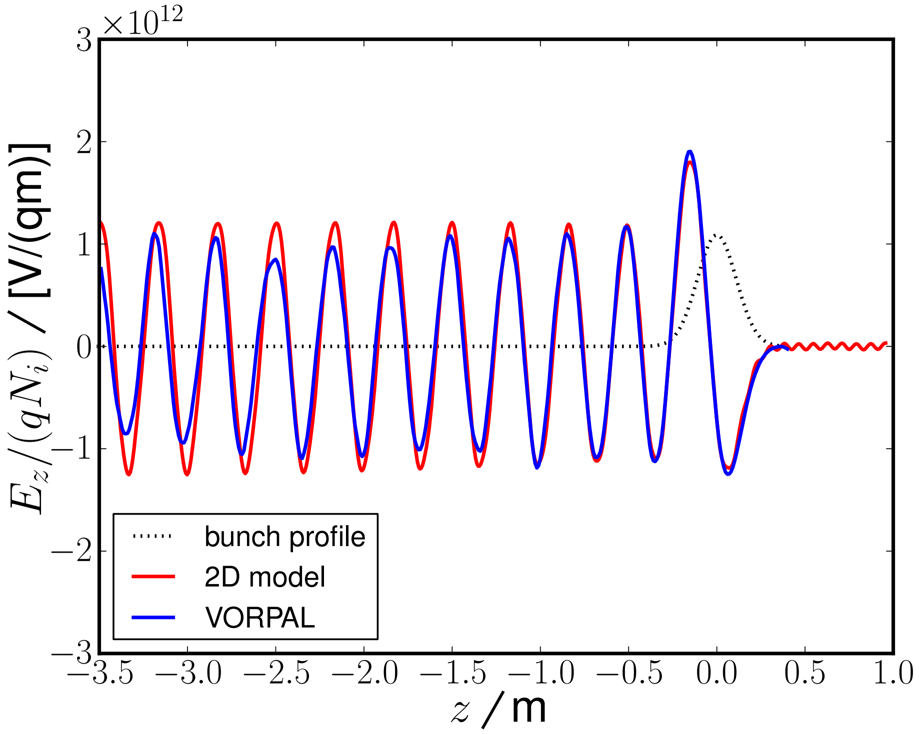

Figure 7.15.: Longitudinal electric field induced by the electron cloud interacting with the short proton bunch (LHC). Electron cloud density is 10^{16} m^{-3}. Long range plasma waves are reproduced by both of the codes.

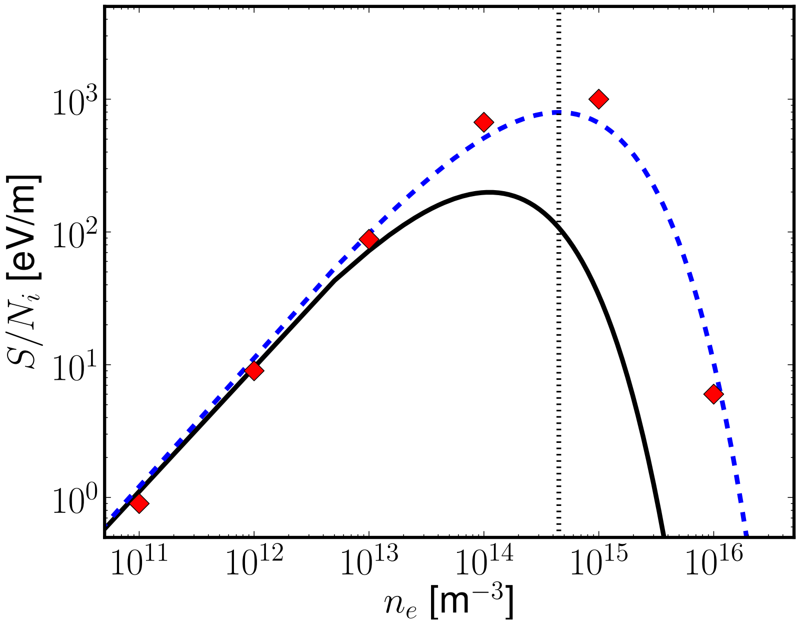

Figure 7.16.: (Courtesy O. Boine-Frankenheim) Stopping power as a function of the electron density. The analytic results obtained from Eq. 5.71 for $\sigma_z = 0.25$ m are represented by the solid curve. The symbols show the results obtained from the simulations. The vertical, dotted line corresponds to $\kappa_e \sigma_z = 1$. The dashed blue curve corresponds to Eq. 5.71 for $\sigma_z \to \sigma_z/2$.

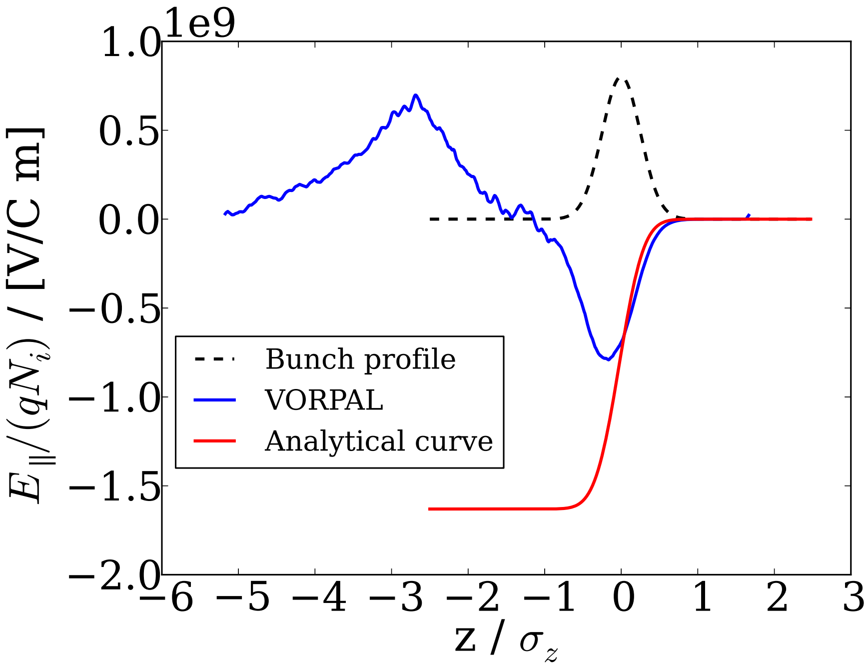

Figure 7.17.: Comparison of the analytical (Eq. 5.84) and simulated wake fields for the SPS parameters. Electron cloud density is $10^{12}\mathrm{m}^{-3}$. The corresponding stopping powers are $S_a = 11.56\ eV/m$ and $S_V = 8.73\ eV/m$.

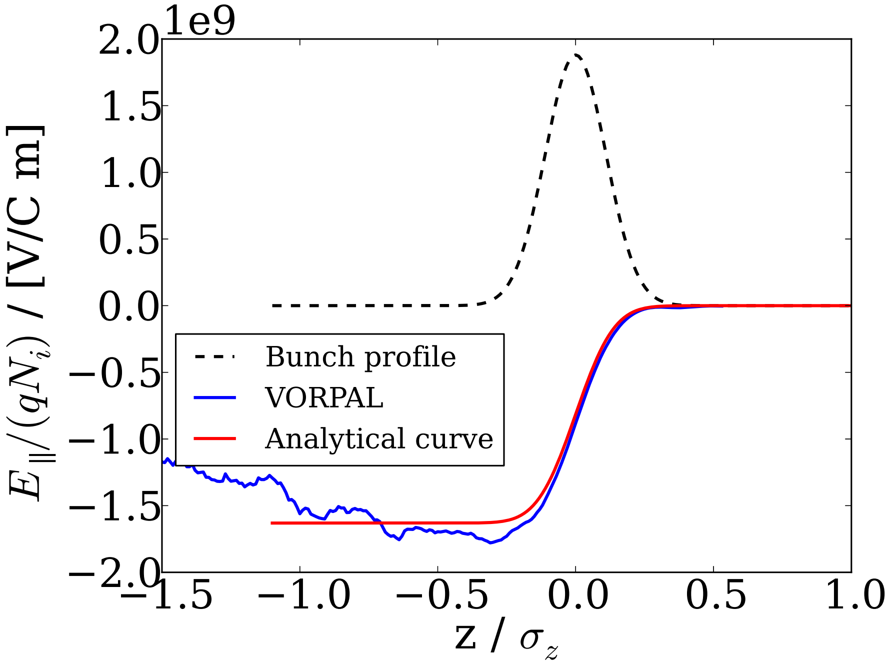

Figure 7.18.: Comparison of the analytical (Eq. 5.84) and simulated wake fields in the LHC geometry. Bunch intensity is 10^9. Electron cloud density is $10^{12}\mathrm{m}^{-3}$. The corresponding stopping powers are $S_a = 0.1156\ eV/m$ and $S_V = 0.1231\ eV/m$.

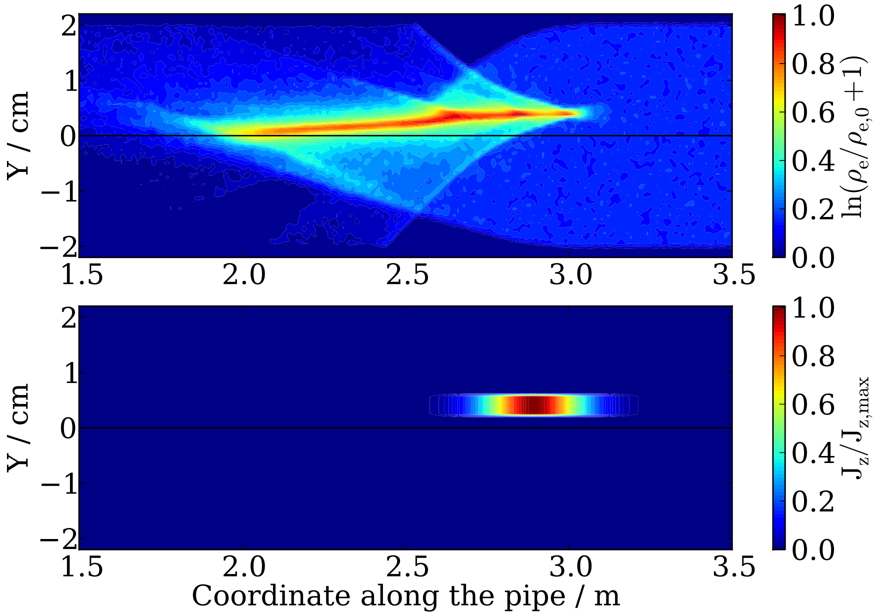

Figure 7.19.: Pinch of the uniform electron cloud around the off-axis bunch (LHC). The upper figure shows the electron cloud density in logarithmic scale. The lower plot shows the position of the bunch relative to the pipe axis.

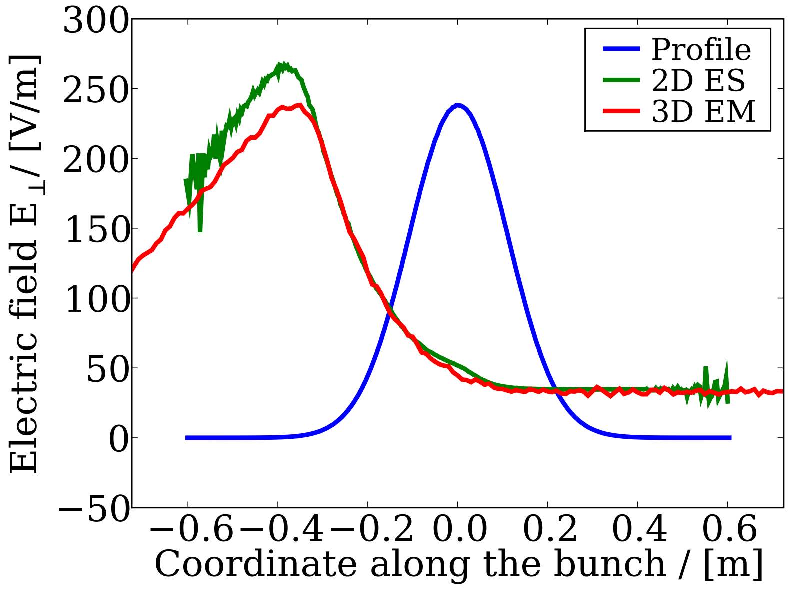

Figure 7.20.: Transverse electric field induced by the electron cloud interacting with the off-centered bunch (LHC). Depicted is the local field strength acting on the bunch averaged over the bunch cross section. The results of VORPAL and particle-in-cell code with 2D Poisson solver are shown. The offset of the bunch is $\Delta y = 4$ mm.

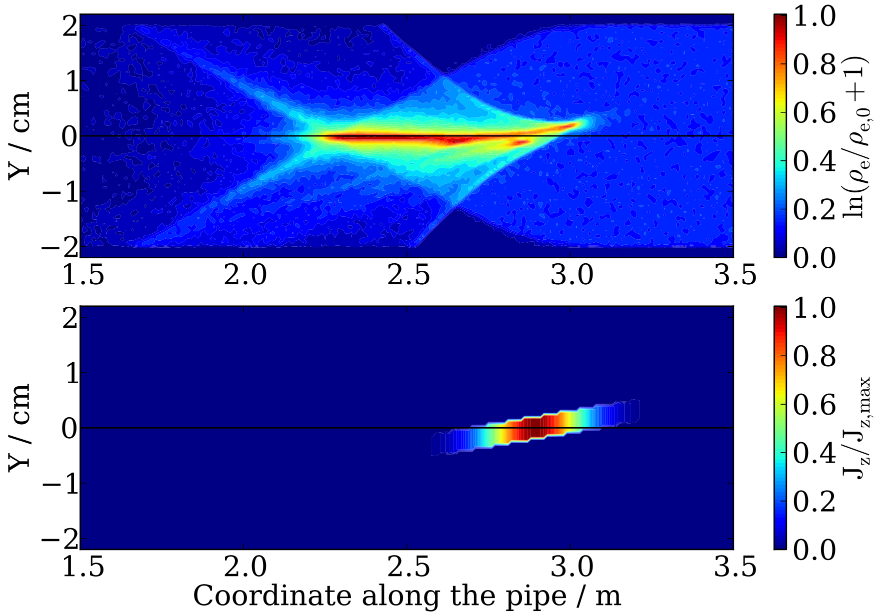

Figure 7.21.: Pinch of the uniform electron cloud around the tilted bunch (LHC). The upper figure shows the electron cloud density in logarithmic scale. The lower plot shows the position of the bunch relative to the pipe axis.

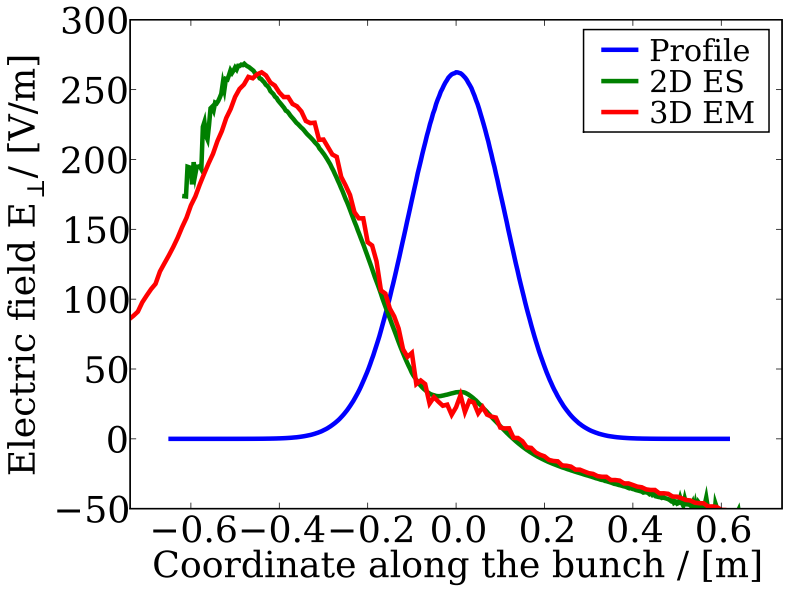

Figure 7.22.: Transverse electric field induced by the electron cloud interacting with the tilted bunch (LHC). Depicted is the local field strength acting on the bunch averaged over the bunch cross section. The results of VORPAL and particle-in-cell code with 2D Poisson solver are shown. The tilt angle of the bunch is $\tan(\theta) = 0.05$.

8 Conclusions and Outlook

The aim of the work was to analyze the electron cloud effects in intense hadron beams under the FAIR and CERN conditions. Different aspects of the electron cloud phenomenon were investigated taking into account specific features of the facilities.

Concerning the FAIR conditions the electron cloud effects were analyzed for the SIS-100 in application to the coasting beams. There the stability of the beam was studied against the electron cloud originating from the residual gas ionization. The analysis of the linear coupled electron-beam equations of motion revealed that the beams with equal space charge tune shifts have identical threshold neutralization factors. We confirmed this in the numerical particle-in-cell simulations for the realistic beam parameters. We also found out that the linear theory underestimates the thresholds compared to the numerical simulations.

In [72] the Coulomb heating of the electron cloud by the beam particles was proposed as a mechanism that can reduce the electron cloud density. Due to these collisions the electron motion is described by the second-order nonlinear stochastic equation. Before this thesis the effect was analyzed only for the unrealistic case of the thick beam uniformly filling the pipe. This corresponds to the limit of a quadratic potential when the average electron energy grows linearly with time [93, 94]. In the framework of this thesis the Coulomb heating effect was analyzed for the realistic beam density distributions. In this case there is no analytical theory describing the average parameters of the electron motion. For this purpose particle-in-cell simulations were performed. The attempt to analyze the heating effect in the beam of a small radius analytically was made. The simulation results indicate the growth of the electron energy under the influence of Coulomb collisions for realistic beam profiles. However, in comparison with the thick beam the time dependence is nonlinear. At some point the electron reaches the wall and gets lost. These losses cause the saturation of the electron density in the case of stationary beam. We found that the saturated neutralization degree is similar for the beams of different ion species if the emittance and energy of the beam is preserved. This agrees well with the simple analytical estimations [72] for thick beams. For the production rates approaching zero (i.e. good vacuum) the cloud density goes proportionally to zero. At high production rates the neutralization is limited by the electron space charge at 100% in agreement with the assumptions of [17].

Combining the results above we found out two separate regimes. In the good vacuum regime the interaction of the electron cloud with the beam is dominated by Coulomb collisions. In this regime beams having identical space charge tune shifts are always stable, i.e., threshold neutralization factor is never reached. In the bad vacuum regime the time to reach the threshold density is smaller than the life time due to Coulomb collisions. The electron-beam interaction in this case is dominated by the two-stream instability.

Under the SIS-100 conditions we found that the design pressure of 10^{-12} mbar corresponds to the good vacuum regime. The problems are very likely to start above 10^{-11} mbar. However, under such conditions other problems for instance beam loss due to charge exchange [13] will also manifest themselves.

Apart from Coulomb heating and the instability studies the problem of electron accumulation in long sausage-like bunches was analyzed in the simulations for simplified gap form factors. Based on the linear theory it was pointed out that the accumulation in a realistic beam with elliptic cross section should be very small. The accumulation is possible only at those places in the beam where the Hill's equation of electron motion gives stable solutions in both planes simultaneously. Before this thesis no simulations were made to compare the simplified linear theory with the nonlinear realistic case. We performed such simulations, and the results revealed that if the beam has a Gaussian transverse profile and the beam density perturbation is far from the adiabaticity, then no long-term accumulation happens even if it is predicted by linear theory. However, if the line density changes adiabatically, then the electrons are trapped in the Gaussian beam. Basically, it means that for realistic beam profiles there is a transition from purely nonadiabatic case (low beam intensities) with no trapping to the adiabatic case (high intensity with significant leak) when the accumulation is determined by the electron interaction with the wall.

Longitudinal electron cloud wake fields in the LHC and the SPS were simulated using the 2D electrostatic particle-in-cell code and in 3D using VORPAL. In the 2D code longitudinal wake fields were obtained after the simulation run using an r-z Poisson solver. Before this thesis such comparison was not performed in the available literature. Both codes showed a very good agreement for the electron cloud densities in the range $10^{11} - 10^{16}\mathrm{m}^{-3}$. This result allowed to simulate the electron cloud stopping powers using the fast 2D code [70]. The order of magnitude of the synchronous phase shift obtained from these stopping powers appears to be in agreement with the LHC observations.

Based on the kick approximation the expression for the longitudinal wake field was derived. The form of the obtained wake field is given by the integral along longitudinal direction. The derived expression gives a very good agreement with the numerical simulations in the limit of low intensities, i.e., 100 times lower than in the LHC. For the realistic LHC conditions it was found out that the disagreement is remarkable at the tail of the bunch. However, as it was mentioned above, such integrated quantity as the stopping power is still in a good agreement with the analytical theory.

Transverse electron cloud wake fields were simulated using the two codes for the $k = 0$ and $k = 1$ head-tail modes of the LHC bunches. For this purpose the LHC bunch was transversely perturbed adding a constant offset or a tilt relative to the pipe axis. For the both bunch configurations the agreement between the transverse wake fields was very good. This indicates that for the LHC conditions the codes with purely transverse bunch-cloud interaction are sufficient.

As a next step the simulations of electron clouds in coasting beams can be extended to a fully self-consistent case including the space charge and longitudinal drift of beam particles. Such simulations would allow to account for the emittance growth. The important feature of the LHC bunches is that they are packed into trains. The behavior of the bunch in the beginning of a train affects the rest bunches of the train. Simulations of these effects are very computationally expensive. It is planned to tackle this problem by simulating the whole bunch train using the Graphical Processing Units. Apart from that, the kick approximation can be extended to produce a better approximation of the wake fields.

A Verification of Numerical Model

To verify that our numerical model correctly describes the interaction between the beam and the electron cloud we have performed several tests. For the first test the broad band impedance was applied to the rigid-slice beam with damping:

$$Z_{Tr}(\omega) = \frac{\omega_r}{\omega} \frac{Z_0}{1 + iQ\left(\frac{\omega_r}{\omega} - \frac{\omega}{\omega_r}\right)}. \tag{A.1}$$

The same impedance was used in the complete PIC code where particles can coast longitudinally. Fig. A.1 shows the maximum amplitude of the beam registered during simulations as a function of resonant frequency and shunt impedance. One can see that the instability threshold agrees well within two codes. The threshold also agrees well with the predictions of the theory (Eq. 4.27). The instability threshold is given as follows:

$$\sqrt{\frac{2}{\pi}} \omega_r \delta_p \eta = \frac{Z^2 e^2 N \beta}{8\pi^2 A m_0 \gamma R Q_\beta} Re(Z_{Tr}). \tag{A.2}$$

For the second test the transverse K-V distribution was taken for the beam. The cloud was placed inside the beam. In this case if the cloud does not exceed the borders of the beam, then the motion is linear and described by Eq. 5.21. The instability growth rate of the numerical beam should agree with the predictions of the linear theory (Eq. 5.24). Fig. A.2 shows the results of simulations and linear model for the FAIR U^{28+} beam at 1 GeV/u.

The cloud size and the instability amplitude for different number of time steps per electron oscillation period are shown in Fig. A.3. Convergence is seen above 25 timesteps per electron oscillation period. In this thesis 60-100 timesteps per electron oscillation period were used.

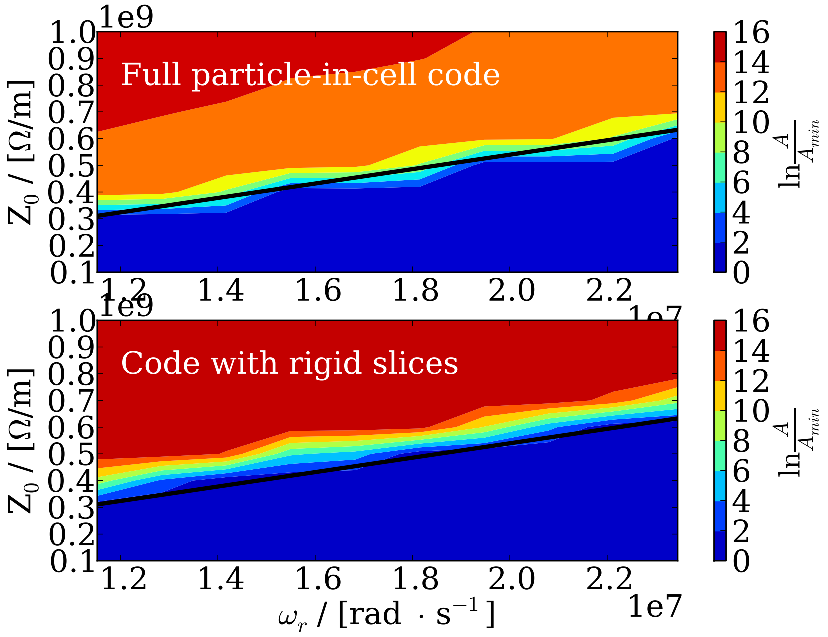

Figure A.1.: The oscillation amplitude of Xe^{48+} beam is shown at 11.4 MeV/u for $dp/p = 5\cdot10^{-4}$. The black line represents the analytical instability threshold given for broad band impedance.

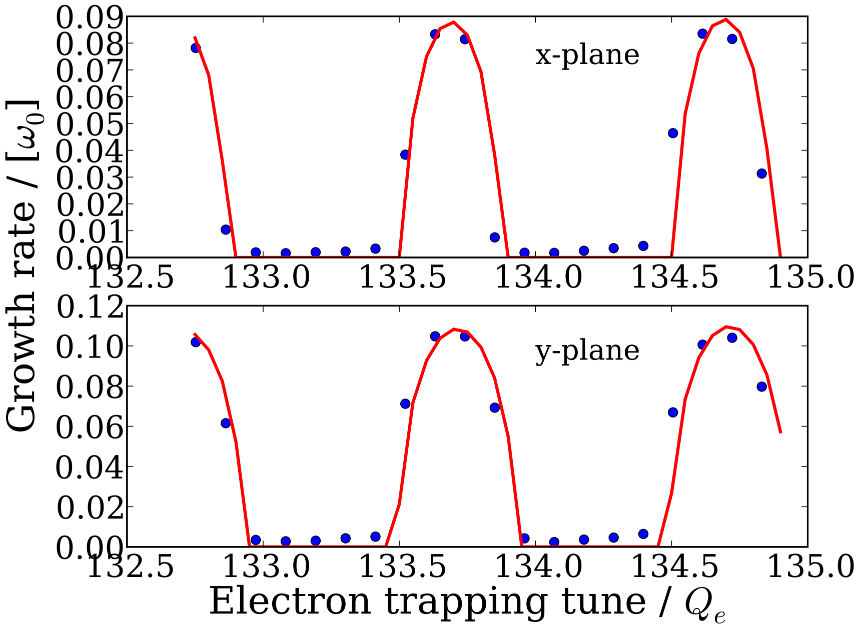

Figure A.2.: Linear instability growth rate for 1% neutralized U^{28+} beam as a function of Q_e. The solid curve is the solution of Eq. 5.24. Symbols represent the simulation results.

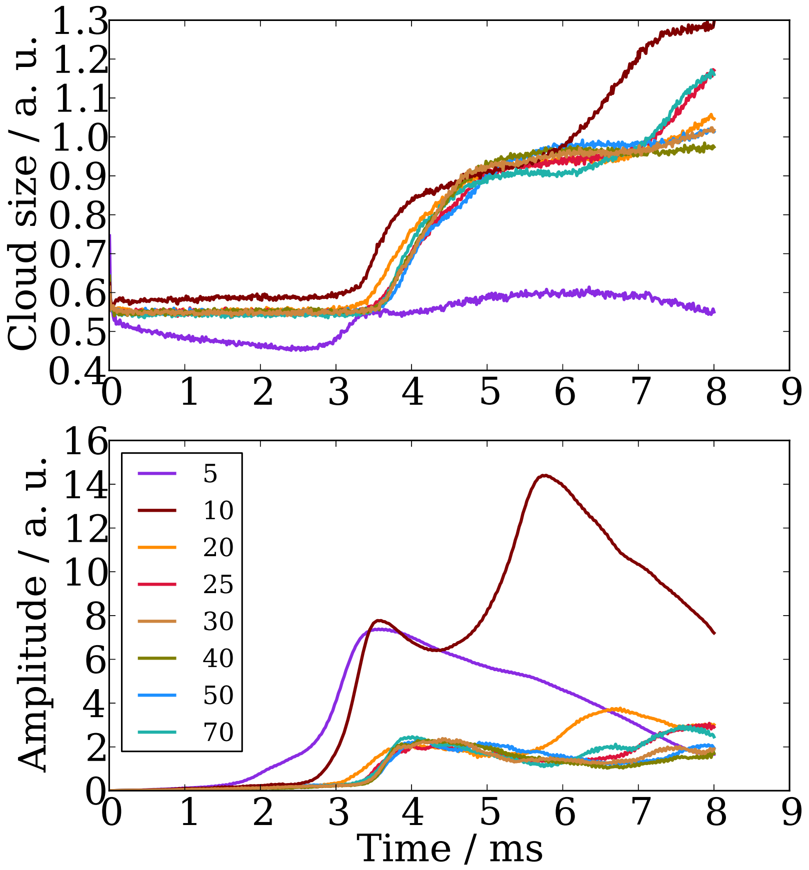

Figure A.3.: The cloud size and the instability amplitude of the U^{73+} beam for different number of time steps per electron oscillation period. The beam energy is 400 MeV/u. Conditions are the same as in Fig. 7.7. Above the 25 timesteps per electron oscillation period the convergence is seen.

B List of Symbols and Abbreviations

a - beam radius
A - mass number
b - impact parameter
$B\rho$ - rigidity
c - speed of light
D - dispersion function
e - electron charge
E_s - average energy of emitted secondary electrons
L - accelerator circumference
L_g - length of the gap in the beam
L_{tail} - length of the tails penetrating the gap
L_l - length of the leakage plateau at minimum density in the gap
$\ln \Lambda$ - Coulomb logarithm
m_e - electron mass
m_0 - atomic unit mass
Q_e - electron bounce tune
Q_i - ion bounce tune
Q_β - betatron tune
Q_x - horizontal betatron tune
Q_y - vertical betatron tune
ξ - chromaticity
q_1 - leading charge
q_2 - trailing charge
R_p - cylindrical pipe radius
R - average accelerator radius
r_e - electron classical radius
t_i - time to reach the threshold electron density
t_h - average electron life time related to the Coulomb heating
T - revolution period
n_e - electron density
V_{rf} - accelerating voltage
$\mathscr{S}$ - ratio of minimum line density in the beam to the lowest line density.
Z - ion charge state
$Z_\perp$ - transverse impedance

$Z_{||}$ - longitudinal impedance
α - one of the Twiss parameters
β - ratio of the velocity to the speed of light
β_x - horizontal beta-function
ϵ_0 - permittivity
ϵ_x - horizontal emittance
ϵ_y - vertical emittance
γ - Lorentz factor
γ_t - transition energy
$\gamma_{d,j}$ - one turn damping coefficient of j-th harmonic
δ_{max} - maximum secondary emission yield
δ_{diff} - number of rediffused electron per incident electron
δ_{refl} - reflection coefficient
δ_p - normalized momentum spread
η - slip factor
λ_i - beam line density
ν_i - electron production rate
ϕ_s - synchronous phase
ρ_i - ion density in the beam
σ_z - bunch rms length
$\sigma_\perp$ - bunch rms radius
σ_x - horizontal beam rms size
σ_y - vertical beam rms size
σ_ω - side band frequency spread
ω_e - electron trapping circular frequency
$\omega_{e,s}$ - electron self space charge frequency
ω_i - electron trapping circular frequency
$\omega_{i,s}$ - ion self space charge frequency
ω_0 - revolution circular frequency
ω_{pe} - plasma frequency
χ_e - neutralization factor

Table B.1.: List of abbreviations

Abbreviation	Full name
ASCII	American Standard Code for Information Interchange
EM	Electromagnetic
ES	Electrostatic
KV distribution	particle distribution with constant transverse density
NEG	Non-Evaporable Getter
PIC code	Particle-in-cell code
SEY	Secondary Emission Yield
CBM	Condensed Baryonic Matter
CERN	European Organisation for Nuclear Research
CMS	Compact Muon Solenoid
FLAIR	Facility for Low-energy Antiproton and Ion Research
HESR	High Energy Storage Ring
LHCb	LHC-beauty
LHCf	LHC-forward
LHC	Large Hadron Collider
MoEDAL	Monopole and Exotics Detector At the LHC
PANDA	Anti-Proton Annihilation at Darmstadt
PSR	Proton Storage Ring
SIS-100	Schwerionensynchrotron-100
SIS-18	Schwerionensynchrotron-18
SNS	Spallation Neutron Source
SPS	Super Proton Synchrotron
TOTEM	Total Cross Section, Elastic Scattering and Diffraction Dissociation

List of Figures

List of Tables

Bibliography

[1] A.A. Budtov, M.F. Vorogushin, V.A. Shyshov, and S.V. Kanaev. ELLUS-6M linear electron accelerator for radiotherapy. In *Proc. RuPAC-2010*, pages 405–407, Protvino, Russia, 2010.

[2] M. Schwicker and A. Peter. Diagnostic instrumentation for medical accelerator facilities. In *Proc. DIPAC 2007*, pages 381–385, Venice, Italy, 2007.

[3] D. Vandeplassche and L. Medeiros Romao. Accelerator driven systems. In *Proc. IPAC 2012*, pages 6–10, New Orleans, Louisiana, USA, 2012.

[4] J.B. Pelka. Synchrotron Radiation in Biology and Medicine. In *Proc. the 7-th National Meeting of Synchrotron Radiation Users*, pages 309–329, Poznan, Poland, 2008.

[5] P. Spiller, Y. El-Hayek, U. Blell, L. Bozyk, J. Stadlmann, and H. Reich-Sprenger. High intensity intermediate charge state heavy ions in synchrotrons. In *Proc. IPAC 2012*, pages 3719–3721, New Orleans, Louisiana, USA, 2012.

[6] R. Cimino, I. R. Collins, M. A. Furman, M. Pivi, F. Ruggiero, G. Rumolo, and F. Zimmermann. Can low-energy electrons affect high-energy physics accelerators? *Physical Review Letters*, v. 93, 014801, 2004. url: dx.doi.org/10.1103/PhysRevLett.93.014801.

[7] F. Zimmermann. Review of single bunch instabilities driven by an electron cloud. *Phys. Rev. ST Accel. Beams*, v. 7, 124801, Dec. 2004. url: dx.doi.org/10.1103/PhysRevSTAB.7.124801.

[8] G. Budker, G. Dimov, and V. Dudnikov. Experiments on producing intensive proton beams by means of the method of charge-exchange injection. *The Soviet Journal of Atomic Energy*, v. 22: pp. 441–448, 1967. (trans. Springer) url: dx.doi.org/10.1007/BF01175205.

[9] J. H. Martin, R. A. Winje, R. H. Hilden, and F. E. Mills. Damping of the coherent vertical instability in the ZGS. In *Proc. Int. Conf. on High Energy Accelerators*, pages 347–350, Frascati, Italy, 1965.

[10] R. Calder, E. Fischer, O. Gröbner, and E. Jones. Vacuum conditions for proton storage rings. In *9-th Int. Conf. on High-energy Accel.*, pages 70–74, SLAC, Stanford, USA, May 1974.

[11] J.A. Crittenden, D.C. Sagan, and K.G. Sonna. Electron cloud modeling for the ILC damping rings. In *Proc. PAC 2011*, pages 1686–1688, New York, USA, 2011.

[12] H. H. Gutbrod, I. Augustin, H. Eickhoff, K.D. Groß, W. F. Henning, D. Krämer, and G. Walter. Accelerator Facilities. FAIR Baseline Technical Report, GSI, Darmstadt, 2006.

[13] P. Puppel, P. Spiller, and U. Ratzinger. Dynamic vacuum stability in SIS100. In *Proc. IPAC 2011*, pages 2724–2726, San Sebastian, Spain, 2011.

[14] L. Bozyk. *Entwicklung und Test eines Kryokollimator-Prototypen zur Kontrolle des dynamischen Vakuums im SIS100*. PhD thesis, Technische Universität Darmstadt, 2011.

[15] G. Rumolo, O. Boine-Frankenheim, E. Mustain, and I. Hofman. Vacuum and electron cloud issues at the GSI present and future facilities. In *Proc. ECLOUD'04*, pages 95–101, Napa, CA, USA, 2004.

[16] G. Budker, G. Dimov, and V. Dudnikov et al. Development of the intense proton beam at the Novosibirsk. In *Proc.X Internat. Conf. Particle Accelerators*, volume 2, page 287, Protvino, USSR, 1977.

[17] Y. Baconnier. Neutralization of Accelerator Beams by Ionization of the Residual Gas. In *CAS - CERN Accelerator School : General Accelerator Physics*, volume 1, pages 267–300, Gif-sur-Yvette, France, Set. 1984.

[18] E. Benedetto, D. Schulte, F. Zimmermann, and G. Rumolo. Simulation study of electron cloud induced instabilities and emittance growth for the CERN Large Hadron Collider proton beam. *Phys. Rev. ST Accel. Beams*, v. 8, 124402, Dec. 2005. url: dx.doi.org/10.1103/PhysRevSTAB.8.124402.

[19] K. Knie P. Forck G. Breitenberger G. Fehrenbacher C. Mühle H. Romakers H. Reich-Sprenger B. Franzke, P. Sievert. Accelerator Facilities. Technical design report fair antiproton target and separator, GSI, Darmstadt, 2008.

[20] H. Stockhorst, R. Maier, D. Prasuhn, R. Stasse, C. Dimopoulou, A. Dolinskii, T. Katayama, Yu. A. Litvinov, M. Steck, and T. Stöhlker. Stochastic cooling developments for HESR at FAIR. In *Proc. IPAC 2012*, pages 388–390, New Orleans, Louisiana, USA.

[21] Andrea Bersani on behalf of the PANDA Collaboration. The PANDA detector at FAIR. *Physica Scripta*, v. 2012, 014006, 2012. url: dx.doi.org/10.1088/0031-8949/2012/T150/014006.

[22] P. Senger for the CBM Collaboration. Ultra-low energy storage ring at FLAIR. *Hyperfine Interactions*, v. 213: pp. 205–215, Dec 2012. url: dx.doi.org/10.1007/s10751-011-0460-z.

[23] E. Widmann, J. Walz, and W. Quint et al. FLAIR: A Facility for Low-energy Antiproton and Ion Research, Letter of Intent for the Future Accelerator, Facility for Beams of Ions and Antiprotons at Darmstadt. Technical report, GSI, Darmstadt, 2004.

[24] P. Senger for the CBM Collaboration. The CBM experiment at FAIR. *Journal of Physics: Conference Series*, v. 50: pp. 357–360, 2006. url: dx.doi.org/10.1088/1742-6596/50/1/048.

[25] H. Geissel and NuSTAR collaboration Super-FRS working group. Technical design report on the Super-FRS. Technical report, GSI, Darmstadt, March 2008.

[26] C. Omet, P. Spiller, J. Stadlmann, and D. H. H. Hoffmann. Charge change-induced beam losses under dynamic vacuum conditions in ring accelerators. *New Journal of Physics*, v. 8: p. 284, 2008. url: dx.doi.org/10.1088/1367-2630/8/11/284.

[27] P. Spiller, L. Bozyk, and P. Puppel. SIS18 - intensity record with intermediate charge state heavy ions. In *Proc. IPAC 2012*, pages 3719–3721, New Orleans, Louisiana, USA, 2012.

[28] J. Stadlmann et al. Ion optical design of SIS100 and SIS300. In *Proc. of EPAC 2008*, pages 358–360, Genoa, Italy, 2008.

[29] N. Pyka, U. Blell, P. Spiller, and J. Stadlmann. Design of the beam extraction systems of the new heavy ion synchrotrons SIS100 and SIS300 at FAIR. In *Proc. EPAC08*, pages 3605–3607, Genoa, Italy, 2008.

[30] G. Arnison, A. Astbury, and B. Aubert et al. Experimental-observation of lepton pairs of invariant mass around 95 GeV/c2 at the CERN SPS collider. *Physics Letters B*, v. 126: pp. 398–410, 1983.

[31] G. Charpak et al. The use of multiwire proportional counters to select and localize charged particles. *Nuclear Instruments and Methods*, v. 62: pp. 262–268, 1968.

[32] O. Brüning, P. Collier, P. Lebrun, S. Myers, R. Ostojik, J. Poole, and P. Proudlock. LHC Design Report Volume I: the LHC Main Ring. CERN-2004-003-V-1, CERN, Geneva, 2004.

[33] G. Aad for the ATLAS collaboration. The ATLAS Experiment at the CERN Large Hadron Collider. *Journal of Instrumentation*, 3 S08003, 2008. url: dx.doi.org/10.1088/1748-0221/3/08/S08003.

[34] Martijn Mulders for the CMS Collaboration. The CMS Experiment: Status and First Results. *arXiv:1006.4010*, 2010.

[35] I. Belikov for the ALICE collaboration. Physics of the ALICE Experiment. *arXiv:hep-ex/0605035*, 2006.

[36] H. Terrier for the LHCb Collaboration. Overview of LHCb. *arXiv:hep-ex/0506047*, 2005.

[37] G. Latino for the TOTEM Collaboration. The TOTEM Experiment at LHC. *arXiv:0805.3968*, 2008.

[38] Y. Itow (for the LHCf Collaboration). The LHCf experiment: verification of interaction models of cosmic rays at 10^{17} eV. *Journal of Physics: Conference Series*, v. 120, 062028, 2008. url: dx.doi.org/10.1088/1742-6596/120/6/062028.

[39] MoEDAL Collaboration. Technical Design Report of the MoEDAL Experiment. CERN-LHCC-2009-006 ; MoEDAL-TDR-001, CERN, Geneva, 2009.

[40] J. F. Esteban Müller, P. Baudrenghien, G. Iadarola, T. Mastoridis, G. Papotti, G. Rumolo, E. Shaposhnikova, and D. Valuch. Synchronous phase shift at LHC. In *Proc. of ECLOUD'12*, La Biodola, Isola d'Elba, 2012.

[41] A. Chao. *Physics of Collective Beam Instabilities in High Energy Accelerators*. John Wiley & Sons, Inc., New York, 1993.

[42] D. A. Edwards and M. J. Syphers. *An introduction to the physics of high energy accelerators*. John Wiley & Sons, Inc., 1993.

[43] M. Reiser. *Design and Theory of Charged Particle Beams. Beam Physics and Accelerator Technology*. John Wiley & Sons, Inc., buch bücher dd ag, Birkach, 1994.

[44] E. Wilson. Transverse beam dynamics. In D. Brandt, editor, *Proc. CAS - Intermediate accelerator physics*, pages 131–158, DESY, Zeuthen, Set. 2003. CERN.

[45] K. Y. Ng. *Physics of Intensity Dependent Beam Instabilities*. World Scientific, Singapour, 2006.

[46] E.D. Courant and H.S. Snyder. Theory of the alternating-gradient synchrotron. *Annals of Physics*, v. 3: pp. 1–48, 1958. url: dx.doi.org/10.1016/0003-4916(58)90012-5.

[47] S. Guiducci. Chromaticity. In *Proc. CAS: 4th General Accelerator Physics Course*, pages 53–68, Jülich, Germany, 1990.

[48] W. Schottky. Über spontane Stromschwankungen in verschiedenen Elektrizitatsaleitern. *Annalen der Physik*, v. 362: pp. 541–567, 1918.

[49] S. Chattopadhyay. Some fundamental aspects of fluctuations and coherence in charged-particle beams in storage rings. Technical Report CERN 84-11, CERN, Geneva, 1984.

[50] S. Appel and O. Boine-Frankenheim. Microbunch dynamics and multistream instability in a Heavy-Ion Synchrotron. *Phys. Rev. ST Accel. Beams*, v. 15, 054201, May 2012. url: dx.doi.org/10.1103/PhysRevSTAB.15.054201.

[51] O. Chorniy. *Measurement and interpretation of the bunched beam transfer function in SIS-18 with space charge*. PhD thesis, Technische Universität Darmstadt, 2008.

[52] A. Hofmann. Landau damping. In *Proc. CAS: Intermediate Course on Accelerator Physics*, pages 271–304, Zeuthen, Germany, 2003.

[53] S. Paret. *Transverse Schottky Spectra and Beam Transfer Functions of Coasting Ion Beams with Space Charge*. PhD thesis, Technische Universität Darmstadt, 2010.

[54] V. Kornilov and O. Boine-Frankenheim. Transverse Instability of Coasting Beam in SIS18. Technical Report Acc-Note-2009-008, GSI, Darmstadt, 2009.

[55] L. Palumbo, V.G. Vaccaro, and M. Zobov. Wake fields and impedance. In *CAS Advanced School on Accelerator Physics*, pages 331–390, Rhodes, Greece, Set. 1994.

[56] T. Weiland and R. Wanzenberg. Wake fields and impedances. In *Frontiers of Particle Beams: Intensity Limitations, Lecture Notes in Physics*, volume 400, pages 39–79. Springer, 1992.

[57] K. Ohmi, F. Zimmermann, and E. Perevedentsev. Wake-field and fast head-tail instability caused by an electron cloud. *Phys. Rev. E*, 65, 016502, Dec. 2001. url: dx.doi.org/doi/10.1103/PhysRevE.65.016502.

[58] G. Rumolo and F. Zimmermann. Electron cloud simulations: beam instabilities and wakefields. *Phys. Rev. ST Accel. Beams*, v. 5, 121002, Dec. 2002. url: dx.doi.org/10.1103/PhysRevSTAB.5.121002.

[59] L.D. Landau. On the vibrations of the electronic plasma. *Journal of Physics USSR*, v. 10: p. 25, 1946.

[60] K. Y. Ng. Decoherence and Landau-damping. Technical Report FN-0763-AD, Fermilab, Batavia, 2005.

[61] K. Schindl. Space charge. In *Proc. CAS: Basic Course on General Accelerator Physics*, page 285, Loutraki, Greece, 1999.

[62] Humberto Maury Cuna and Jesus Guillermo Contreras. Simulations of electron-cloud heat load for the cold arcs of the CERN large hadron collider and its high-luminosity upgrade scenarios. *Phys. Rev. ST Accel. Beams*, v. 15, 051001, May 2012. url: dx.doi.org/10.1103/PhysRevSTAB.15.051001.

[63] S.Y. Zhang et al. Experience in reducing electron cloud and dynamic pressure rise in warm and cold regions in RHIC. In *Proc. EPAC2006*, pages 595–597, Edinburgh, Scotland, 2006.

[64] E. Benedetto, G. Franchetti, K. Ohmi, D. Schulte, and F. Zimmermann. Emittance growth caused by electron cloud below the fast TMCI threshold: numerical noise or true physics? In *Proc. PAC 2005*, pages 1344–1346, Knoxville, Tennessee, USA, 2005.

[65] M. Tobiyama, J. W. Flanagan, H. Fukuma, S. Kurokawa, K. Ohmi, and S. S. Win. Coupled bunch instability caused by an electron cloud. *Phys. Rev. ST Accel. Beams*, v. 9, 012801, Jan. 2006. url: dx.doi.org/10.1103/PhysRevSTAB.9.012801.

[66] S. De Santis, J. M. Byrd, M. Billing, M. Palmer, J. Sikora, and B. Carlson. Characterization of electron clouds in the Cornell Electron Storage Ring Test Accelerator using TE-wave transmission. *Phys. Rev. ST Accel. Beams*, v. 13, 071002, July 2010. url: dx.doi.org/10.1103/PhysRevSTAB.13.071002.

[67] Jie Wei. Spallation Neutron Source ring - status, challenges, issues, and perspectives. In *Proc. PAC 2003*, volume 1, pages 571–575, 2003.

[68] R. J. Macek et al. Electron cloud generation and trapping in a quadrupole magnet at the Los Alamos Proton Storage Ring. *Phys. Rev. ST Accel. Beams*, v. 11, 01010, Jan. 2008. url: dx.doi.org/10.1103/PhysRevSTAB.11.010101.

[69] U. Iriso and S. Peggs. Maps for electron clouds. *Phys. Rev. ST Accel. Beams*, 8, 024403, Feb. 2005. url: dx.doi.org/10.1103/PhysRevSTAB.8.024403.

[70] O. Boine-Frankenheim, E. Gjonaj, F. Petrov, F. Yaman, T. Weiland, and G. Rumolo. Energy loss and longitudinal wakefield of relativistic short proton bunches in electron clouds. *Phys. Rev. ST Accel. Beams*, v. 15, 054402, May 2012. url: dx.doi.org/10.1103/PhysRevSTAB.16.034201.

[71] K. Ohmi, T. Toyama, and M. Tomizawa. Study of ep instability for a coasting proton beam in circular accelerators. In *Proc. PAC 2003*, pages 3083–3085, Portland, OR, USA, 2003.

[72] P. Zenkevich et al. Adiabatic theory of electron oscillations and its application to SIS100/SIS200. In *Proc. ECLOUD'02*, pages 91–96, 2002.

[73] P. R. Zenkevich. Transverse electron-ion instability in ion storage rings with high current. In *AIP Conf. Proc.*, volume 480, pages 74–84, 1998.

[74] H. Qin, E. A. Startsev, and R. C. Davidson. Nonlinear perturbative particle simulation studies of the electron-proton two-stream instability in high intensity proton beams. *Phys. Rev. ST Accel. Beams*, v. 6, 014401, Jan. 2003. url: dx.doi.org/10.1103/PhysRevSTAB.6.014401.

[75] P. J. Channell. Phenomenological two-stream instability model in the nonlinear electron regime. *Phys. Rev. ST Accel. Beams*, v. 5, 114401, Nov. 2012. url: dx.doi.org/10.1103/PhysRevSTAB.5.114401.

[76] L. Wang, H. Hseuh, Y. Y. Lee, D. Raparia, J. Wei, S. Cousineau, and S. Henderson. Electron cloud in the collimator- and injection- region of the Spallation Neutron Source's accumulator ring. In *Proc. PAC 2005*, pages 1865–1867, Knoxville, Tennessee, 2005.

[77] B. Angerth, F. Bertinelli, J. C. Brunet, R. Calder, J. Gomez-Goni, O. Gröbner, A.G. Mathewson, A. Poncet, C. Reymermier, and E. Wallen. The cold vacuum system of the Large Hadron Collider. In *4th EPAC*, pages 2467–2469, London, UK, 1994.

[78] G. Lanza, V. Baglin, G. Bregliozzi, and J.M. Jimenez. LHC beam vacuum during 2011 machine operation. In *Proc. IPAC 2012*, New Orleans, Louisiana, USA, 2012.

[79] R. Davis, P. He, H.C. Hseuh, R. Lee, D. Pate, L. Smart, R. Todd, and D. Weiss. Performance of RHIC vacuum systems. In *Proc. PAC 2012*, pages 2156–2158, Chicago, USA, 2012.

[80] K. Kanazawa, S. Kato, Y. Suetsugu, H. Hisamatsu, M. Shimamoto, and M. Shirai. The vacuum system of KEKB. *Nuclear Instruments and Methods A*, v. 499: pp. 66–74, 2002. url: dx.doi.org/10.1016/S0168-9002(02)01774-6.

[81] I. D. Kaganovich et al. Scaling and formulary of cross-sections for ion-atom impact ionization. *New Journal of Physics*, 8:278, 2006. url: dx.doi.org/10.1088/1367-2630/8/11/278.

[82] S. Federmann, F. Caspers, and E. Mahner. Measurements of electron cloud density in the CERN Super Proton Synchrotron with the microwave transmission method. *Phys. Rev. ST Accel. Beams*, v. 14, 012802, Jan. 2011. url: dx.doi.org/10.1103/PhysRevSTAB.14.012802.

[83] M. A. Furman and M. T. F. Pivi. Probabilistic model for the simulation of secondary electron emission. *Phys. Rev. ST Accel. Beams*, v. 5, 124404, Dec. 2002. url: dx.doi.org/10.1103/PhysRevSTAB.5.124404.

[84] M.C. Bellachioma, H. Kollmus, A. Krämer, J. Kurdal, H. Reich-Sprenger, L. Urban, and M. Wengenroth. Study of the pressure profile inside the NEG coated chambers of the SIS 18. In *Proc. IPAC 2012*, pages 2519–2521, New Orleans, Louisiana, USA, 2012.

[85] F. Le Pimpec, F. King, R.E. Kirby, and M. Pivi. Secondary Electron Yield Measurements of TiN Coating and TiZrV Getter Film. SLAC-TN-03-052, SLAC, Stanford, US, 2004.

[86] L. D. Landau and E. M. Livshits. *A Course of Theoretical Physics: Mechanics*, volume 1. Nauka, Moskow, 1988.

[87] D. Koshkarev and P. Zenkevich. Resonance of coupled transverse oscillations in two circular beams. *Particle Accelerators*, v. 3: pp. 1–9, 1972.

[88] W. Schnell and B. Zotter. A simplified criterion for transverse stability of a coasting beam, and its application to the ISR. CERN Report CERN-ISR-GS-RF-76-26, 1976.

[89] E. Mahner. Review of heavy-ion induced desorption studies for particle accelerators. *Phys. Rev. ST Accel. Beams*, v. 11, 104801, Oct 2008. url: dx.doi.org/10.1103/PhysRevSTAB.11.104801.

[90] G. Rumolo, O. Boine-Frankenheim, and D. Krämer. Estimations of Beam Lifetimes in the SIS18. In *AIP Conf. Proc.*, volume 773, pages 229–232, 2005.

[91] K. Ohmi and T. Toyama. Electron cloud effect in J-PARC proton rings. Presented at ATAC05, 2005.

[92] G. K. Basak and P. Lee. Asymptotic properties of an estimator of the drift coefficients of multidimensional Ornstein-Uhlenbeck processes that are not necessarily stable. *Electronic Journal of Statistics*, 2:1309–1344, 2008. url: dx.doi.org/10.1214/08-EJS290.

[93] N. Lin and S. V. Lototsky. Undamped Harmonic Oscillator Driven by Additive Gaussian White Noise: A Statistical Analysis. *Communications on Stochastic Analysis*, v. 5: pp. 233–250, 2011.

[94] A. H. Strommen Melbo and D. J. Higham. Numerical simulation of a linear stochastic oscillator with additive noise. *Applied Numerical Mathematics*, v. 51: pp. 89–99, 2004. url: dx.doi.org/10.1016/j.apnum.2004.02.003.

[95] G. Rumolo, F. Ruggiero, and F. Zimmermann. Simulation of the electron-cloud build up and its consequences on heat load, beam stability, and diagnostics. *Phys. Rev. ST Accel. Beams*, v. 4, 012801, Feb. 2001. url: dx.doi.org/10.1103/PhysRevSTAB.4.012801.

[96] O. Boine-Frankenheim and V. Kornilov. Implementation and validation of space charge and impedance kicks in the code PATRIC for studies of transverse coherent instabilities in FAIR rings. In *Proc. ICAP 2006*, pages 267–270, Charmonix, France, 2006.

[97] G. Rumolo and F. Zimmermann. *Practical User Guide for ECloud*. CERN. Geneva, 2002. CERN-SL-Note-2002-016.

[98] O. Boine-Frankenheim. RF barrier compression with space charge. *Phys. Rev. ST Accel. Beams*, v. 13, 034202, Mar 2010. url: dx.doi.org/10.1103/PhysRevSTAB.13.034202.

[99] C. Nieter and J.R. Cary. VORPAL: a versatile plasma simulation code. *Journal of Computational Physics*, v. 196: pp. 448–473, 2004. url: dx.doi.org/10.1016/j.jcp.2003.11.004.

[100] Tech-X Corporation. *VORPAL Reference Manual, Release 5.0*, 2011.

[101] L. Bozyk, P. Spiller, and H. Kollmus. Development of a cryocatcher-system for SIS100. In *Proc. IPAC 2012*, pages 3237–3239, New Orleans, Louisiana, USA, 2012.

[102] G. Franchetti, I. Hofmann, S. Sorge, and V. Kapin. High intensity nonlinear dynamics in SIS100. In *Proc. IPAC 2012*, pages 3242–3244, New Orleans, Louisiana, USA, 2012.

[103] O. Boine-Frankenheim. The FAIR accelerators: Highlights and challenges. In *Proc. IPAC 2010*, pages 2430–2434, Kyoto, Japan, 2010.

[104] O. Boine-Frankenheim. Collective effects at FAIR. In *talk at GSI-CERN Ecloud Workshop*, March 2011.

[105] O. Kester. High intensity issues at FAIR. In *Proc. HB2012, MOI1B01*, Beijing, China. url: jacow.ihep.ac.cn/pls/hb2012/MOI1B01.PDF.

Acknowledgements

First of all, I would like to thank my supervisor Prof. Oliver Boine-Frankenheim for supervising and inspiring me during all the years of my PhD work. All the discussions and the overall spirit in the Beam Physics group were always very motivating.

I would like to thank Prof. Dr.-Ing. Thomas Weiland for being my co-referent, for creating a good working spirit in the TEMF institute and for supporting my last months of PhD.

Another thanks goes to Prof. Dr. Dieter Hoffman from the IKP for being my second co-referent.

I want to thank Dr. Vladimir Kornilov for answering a lot of my questions and helping me during the experiments. More than 3 years ago I responded to his announcement in the Internet concerning the PhD position in Darmstadt.

Special thanks go to Dr. Holger Kollmus and his team for manufacturing the electron cloud pick-up and supporting the experiments involving it. Also thanks for sharing with me the knowledge about the vacuum parameters of the SIS-18.

I appreciate a lot fruitful discussions with Dr. Giuliano Franchetti and Dr. Stefan Sorge. Thank you for sharing with me your knowledge about the SIS-100 intensity and optics details.

I would like to thank Sylvain Franke, Dr. Andrzej Stafiniak, Dr. Vera Chetvertkova, Dr. Ivan Strasik and Dr. Sabrina Appel for being very interesting office mates.

Moreover, a lot of thanks goes to a team of my German proofreaders and correctors (all are my collegues): Dr. Stefan Sorge, Paul Görgen, Klaus Klopfer, Sylvain Franke, Joel Alain Tsemo Kamga. Your help was priceless.

Many thanks go to Prof. Dr. Pavel Zenkevich and Dr. Alexei Burov for sharing their knowledge concerning the electron clouds in coasting beams and criticism with me.

In general, I want to thank all the GSI and TEMF colleagues for sharing with me their ideas and experience. I want to thank the BMBF for the financial support of my work (contract 06DA9022I).

Finally, I want to thank my parents for supporting me during these years. Thanks to my beloved wife, Nadezhda.

Curriculum Vitae

Fedor Petrov
Born on 25.07.1985 in Leningrad, USSR

Education

August, 2009 - Present	Technische Universität Darmstadt, Theorie für Elektromagnetischer Felder, Darmstadt, Germany: PhD student
2006-2009	Saint-Petersburg State University, Physics Faculty, Saint-Petersburg, Russia: Master's degree in plasma physics. Subject of thesis: "Study of Partially Constricted Glow Discharge in Ar/N_2 mixtures."
2002-2006	Saint-Petersburg State University, Physics Faculty, Saint-Petersburg, Russia: Bachelor's degree in plasma physics. Subject of thesis: "The Formation of the Spatial Structure of Glow Discharge"
2000-2002	Academic Gymnasium No. 45 at Saint-Petersburg State University

Professional Experience

2009	State Company "Mineral", Programmer (part-time job)
2006-2008	Nuclear Safety Institute of Russian Academy of Sciences, Programmer (part-time job)

Computer Skills

Operating systems	Linux, Windows, Android
Programming languages	C/C++, Java, JavaScript, Scala, Python, Bash, ActionScript
Applications	gnuplot, Origin, SciDAVis, Eclipse, Microsoft Office, Libreoffice

Refereed publications

1. O. Boine-Frankenheim, E. Gjonaj, F. Petrov, F. Yaman, T. Weiland, and G. Rumolo, Energy loss and longitudinal wakefield of relativistic short proton bunches in electron clouds, Phys. Rev. ST Accel. Beams 15, 054402 (2012)
2. Y.Z. Ionikh, N.A. Dyatko, A.V. Meshchanov, A.P. Napartovich and F.B. Petrov, Partial constriction in a glow discharge in argon with nitrogen admixture, 2012 Plasma Sources Sci. Technol. 21 055008
3. Yu. Z. Ionikh, A. V. Meshchanov, F. B. Petrov, N. A. Dyatko and A. P. Napartovich, Partially Constricted Glow Discharge in an Argon-Nitrogen Mixture, Plasma Physics Reports, 2008, Vol. 34, No. 10, pp. 867
4. Dyatko N.A., Ionikh Y.Z., Kochetov I.V., Marinov D.L., Meshchanov A.V., Napartovich A.P., Petrov F.B., Starostin S.A. Experimental and theoretical study of the transition between diffuse and contracted forms of the glow discharge in argon, J. Phys.D: Appl. Phys. 2008. V. 41. P. 055204.